Influence of magnetism on the martensitic transition and related magnetocaloric effect in NiMn-based Heusler alloys

Dissertation

zur Erlangung des akademischen Grades
Doktor der Naturwissenschaften

an der Fakultät für Physik
der Universität Duisburg-Essen

vorgelegt von

Ivan Titov
Moscow, Russian Federation

November 2014

1 Gutachter: Prof. Dr. Michael Farle
2 Gutachter: Dr. Jürgen Lindner
Tag der mündlichen Prüfung: 19 Februar 2015

To my dear parents, who never lived to see this thesis done,
To my beloved wife Elena for all her love and compassion,
To my grandfather Prof. i.R. Dr. V. E. Titov for
being the exemplar of scientific curiosity.

Contents

Abstract

This work is devoted to improving the understanding of the magnetic and magnetocaloric properties of martensitic Ni-Mn-based Heusler alloys with Ga, In and Sn.

Ni-Mn-Sn, Ni-Mn-In and Ni-Mn-(In,Sn) alloys were chosen as prototype alloys for studying the adiabatic temperature change on cyclic field change. Each of these compositions are known for exhibiting large field-induced entropy changes up to $4\ Jkg^{-1}K^{-1}T^{-1}$ and the inverse magnetocaloric effect (MCE) on applying a magnetic field. We show with adiabatic calorimetry studies that the adiabatic temperature change on initial field application is larger than the one observed on the following field removal and application cycles. Thus in Ni-Mn-In, the inverse MCE of constant size is observed in the following cycles. This is related to the reversibility in the field-induced-change in the austenite-to-martensite ratio caused by magnetoelastic effects observed in these alloys.

In contrast, in Ni-Mn-Sn, the inverse MCE observed on first field application is followed by conventional MCE on field removal and on following cycles. Such behavior arises from small field-induced change in the austenite-to-martensite ratio being lower by an order of magnitude than in Ni-Mn-In. In Ni-Mn-(In,Sn) alloys, the inverse MCE with decreasing magnitude is observed on the cyclic field-change. This behavior is related to irreversibilities in the austenite-to-martensite ratio on cyclic field change.

Compositional series of Ni-Mn-Ga and Ni-Mn-Sn alloys with varying Ni and Mn concentrations were studied by means of ferromagnetic resonance and polarized neutron scattering. With these studies, we show that antiferromagnetic Mn-Mn interactions play the key role in martensitic transformations, and the absence of antiferromagnetic interactions renders the structural transformation impossible. We also show the presence of antiferromagnetic interactions in both the magnetically ordered martensite phase and in the magnetically disordered austenite phase in Mn-rich martensitic Ni-Mn-based Heusler alloys.

The (Ni,Co)-Mn-In alloy is a prototype for large magnetostrain and magnetocaloric effect applications exhibiting large temperature range with low magnetization between T_C^M and A_s in the martensite phase. We show that in this alloy, ferromagnetic domains remain down to $180\ K$ below M_s on cooling. On warming, ferromagnetic domains develop below the austenite start A_s temperature at $250\ K$.

Ni-Mn-In is known for its large shift of the structural transition temperature M_s of about $10\ K/T$ along with partial stabilization of the austenite phase far below M_s. We use field-dependent neutron diffraction on a Ni-Mn-In sample to investigate phenomena of the austenite arrest in this alloy.

Kurzzusammenfassung

Zielsetzung dieser Arbeit ist ein besseres Verständig der magnetischen und magnetokalorischen Eigenschaften der martensitischen NiMnZ (Z = Ga, In und Sn) Heuslerlegierungen.

Die Legierungen Ni-Mn-Sn, Ni-Mn-In und Ni-Mn-(In,Sn) wurden als Protopyen für die Untersuchungen der adiabatischen Temperaturänderung bei sich zyklisch ändernden Magnetfeldern ausgewählt. Jede dieser Legierungen ist für ihre große feldinduzierte Entropieänderung von bis zu $4\ Jkg^{-1}K^{-1}T^{-1}$ und ihren inversen magnetokalorischen Effekt (MCE) bekannt. Es zeigt sich, dass die adiabatische Temperaturänderung bei erstmaligem Anlegen des Magnetfeldes größer ist als die beim Ausschalten und bei der zyklischen Änderung des Feldes. Ni-Mn-In besitzt einen konstanten inversen MCE für oszillierende Felder. Dies steht in Beziehung mit der reversiblen feldinduzierten Änderung des Austenit-Martensit Verhältnisses, die auch durch den magnetoelastischen Effekt beobachtet werden kann.

Im Gegensatz dazu zeigt Ni-Mn-Sn nur beim ersten Anlegen eines Feldes einen inversen MCE, beim Ausschalten des Feldes und bei zyklischer Feldänderung zeigt sich ein konventioneller MCE. Dieses Verhalten ergibt sich aus einer geringen feldinduzierten Änderung des Austenit-Martensite Verhältnisses die hier eine Größenordnung kleiner ist als in Ni-Mn-In. Für Ni-Mn-(In, Sn) Legierungen zeigt sich ein inverser MCE mit abfallender Magnetisierung, sowie eine Reversibilität des Austenite-Martensite, Verhältnisses, für die zyklische Feldänderung.

Probenserien der Legierungen Ni-Mn-Ga und Ni-Mn-Sn mit variierender Ni und Mn Konzentration werden mittels ferromagnetischer Resonanz und polarisierter Neutronenstreuung untersucht. Durch diese Untersuchungen kann gezeigt werden, dass die antiferromagnetische Wechselwirkung der Mn Atome eine Schlüsselrolle in der Martensit Umwandlung spielt. Die Abwesenheit der antiferromagnetischen Wechselwirkung macht die strukturelle Umwandlung unmöglich. Außerdem kann gezeigt werden, dass in der magnetisch geordneten Martensit-Phase also auch in der magnetisch ungeordneten Austenit-Phase in Mn-reichen martensitischen Ni-Mn-basierten Heuslerlegierungen antiferromagnetische Wechselwirkung auftreten.

(Ni,Co)-Mn-In Legierungen sind Prototypen für Systeme mit großem magnetoelastischem und magnetokalorischem Effekt und zeigen in einem weiten Temperaturbereich zwischen T_C^M und A_s der Martensit-Phase eine geringe Magnetisierung. Für diese Legierungen bleiben die ferromagnetischen Domänen während des Kühlens bis zu 180 K unterhalb von M_s bestehen. Während des Heizens entstehen die ferromagnetischen Domänen unterhalb der Austenit- Starttemperatur A_s bei 250 K.

Ni-Mn-In ist bekannt für seine große Verschiebung der strukturellen Umwandlungstemperatur M_s von etwa $10\ K/T$ mit einer partiellen Stabilisierung der Austenite-Phase weit unterhalb von M_s. Wir verwenden feldabhängige Neutronendiffraktometrie, um das Phänomen des «Martensite-Arrest» zu untersuchen. ngerman

1 Introduction

> The last thing one knows when writing a book is what to put first.
>
> Blaise Pascal, 1670

This work is devoted to the study of a certain class of smart materials: Heusler alloys. This class of alloys is named after the German metallurgist Friedrich Heusler, who discovered the alloy with composition Cu_2MnAl in 1903 [1, 2]. This alloy made considerable impact on studies of magnetism both for its high Curie temperature ($600\ K$) and for exhibiting ferromagnetism, while containing no ferromagnetic (FM) element (review devoted to this by O. Heusler [3]). Later, Heusler alloys attracted much attention as promising multifunctional materials with various possible applications: conventional shape memory effect, half-metallicity [4], and moreover, various applications related to properties induced by applying a magnetic field; such as magnetic shape memory, giant magnetoresistance and magnetocaloric effect.

The term `Heusler alloy` is referenced to ternary intermetallic compounds with stoichiometry X_2YZ (`full-Heusler`, L_21 cubic crystal structure), XYZ (`half-Heusler`, C_1b cubic structure with one of the fcc lattices unoccupied, see fig. 1.1). Off-stoichiometric compounds are also referred to as Heusler alloys as well. This work is mainly focused on the investigation of Ni-Mn-Z Heusler systems, where Z is IIIA-VA element such as Ga, In, Sb, Sn. Both full-Heusler and off-stoichiometric FM systems are considered. Some of these FM alloys undergo a martensitic transition: a diffusionless temperature-dependent structural transition between a high-temperature cubic austenite phase with high symmetry and a low-temperature orthorhombic martensite phase with lower symmetry. Various physical properties of the system change along with the variation in the austenite-to-martensite ratio $\frac{a}{m}$ during the transition. The transition temperature and its parameters depend on the composition of the alloy and can be varied in a broad temperature range. The martensitic structural transition in FM Heusler alloys can also be triggered by applying either an external magnetic field or hydrostatic pressure. Due to this fact, much research is conducted on Heusler alloys as prototypes for *smart materials*.

Attention was drawn to Ni-Mn-based Heusler alloys with the discovery of large magnetostrain effect in single crystal stoichiometric Ni_2MnGa in 1996 [6, 7]. Observed giant field-induced strains of about 0.2% under the application of the magnetic field in $Ni-Mn-Ga$ can be compared with other materials showing $\geqslant$ 0.1% piezoelectric strain (lead-zirconate-titanate), $\approx$ 0.24% (rare-earth/transition metal alloys) [8] and makes their application as actuators or sensors feasible. Moreover further studies resulted in observed strains up to $\approx 10\%$ in $Ni_{48.8}Mn_{29.7}Ga_{21.5}$ on applying the magnetic field of $1\ T$ at ambient temperature [9].

The discovery of the large magnetocaloric effect (MCE) in $Gd_5Si_2Ge_3$ around room temperature in 1996 [10] revived scientific and technological interest in magnetic refrigeration. Adiabatic heating of the refrigerant on applying a magnetic field can be used in environmentally-friendly "green" and fuel-independent refrigerators as an alternative to vapor-compression technology [11]. Some years later, considerable entropy change was observed in a single crystal Ni-Mn-Ga alloy close to the 2-1-1 stoichiometric composition [12, 13]. The reported entropy change of $\approx$18 $Jkg^{-1}K^{-1}$ is comparable to the effect observed in $Gd_5Si_2Ge_2$. Recently, the so-called *inverse* MCE was observed in the martensitic $Ni_{50}Mn_{37}Sn_{13}$ alloy at room temperature [14] also exhibiting high entropy change.

Extensive studies on structural and magnetic properties of Ni-Mn-Z (Z=Ga, In, Sn, Sb) based Heusler alloys were undertaken by T. Krenke [5] and were succeeded by S. Aksoy [15] introducing FM resonance and neutron scattering techniques to solve the problem of nature of magnetism in Heusler alloys. These studies also covered various magnetic-field driven properties such as magnetic superelasticity, magnetocaloric effect, and austenite arrest.

The martensitic transition is accompanied by a change in the electronic structure which leads to a change in the charge transport properties such as resistivity [16], magnetoresistance [17, 18], Hall effect [19, 20] and thermopower [21]. Since the discovery of large magnetoresistance effects in Heusler alloys, their applicability in various technological microelectronics applications became worth considering. In Ni-Mn-based Heusler alloys doped with In [22] and Sn [23], effects as large as 70% and 50%, respectively, can be obtained by the magnetic-field-induced phase transition at temperatures just below M_S.

In addition to the fact that these *smart* materials are potentially useful for various technical applications, a broad spectrum of observed effects makes them an interesting class of materials for fundamental studies. Most of these properties depend on the presence of martensitic transition, thus focusing the interest on the temperature range of the transition. All Ni-Mn-based Heusler alloys share the same feature under low external magnetic field ($\leq 10\ mT$): an abrupt change in the magnetization during the martensitic transition and a difference between the temperature dependencies of the magnetization on warming and cooling. To explain these features, it was suggested that besides the presence of FM coupling, there is strengthening of Mn-Mn antiferromagnetic (AF) bonding as sample turns martensitic. This hypothesis was supported by recent observations of exchange-bias and non-saturating behavior in the field-dependence of the magnetization in the martensite phase [24, 25], although Mössbauer studies suggested the presence of a sole paramagnetic phase in the martensite phase [26, 27]. Elaborate polar-

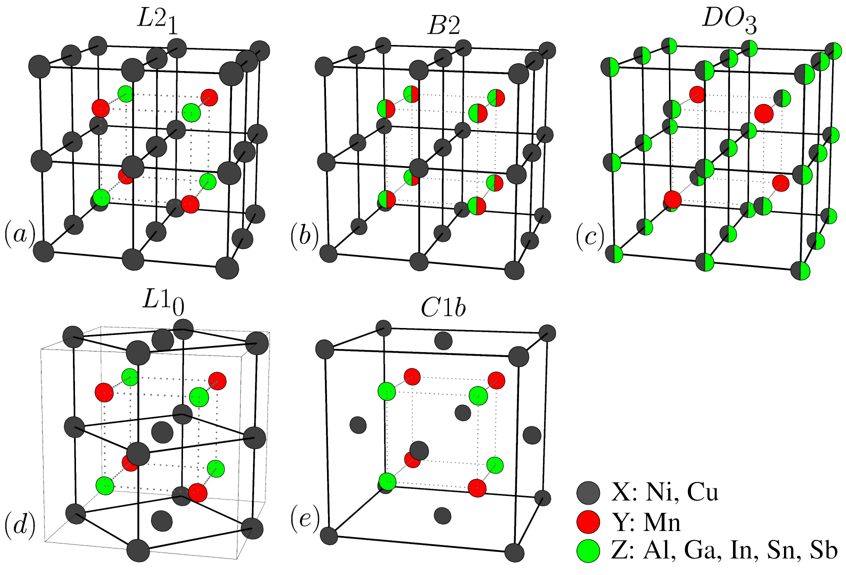

Figure 1.1: Different types of Heusler austenite crystal structures: $L2_1$ of Cu_2MnAl (a); $B2$, $CsCl$-like (b); DO_3, Fe_3Al-like (c); full Heusler martensitic cell: two stacked $L1_0$ cells, $AuCu$-like (d) and half-Heusler alloy lattice $C1_b$, CaF_2-like (e). Adopted from [5].

ized neutron scattering experiments showed AF correlations both in martensite and austenite phases in Ni-Mn-based Heusler alloys [28].

This thesis is devoted to the understanding of the physical properties of the Heusler alloys in the vicinity of the structural transition addressing the understanding of the physical properties on the macroscale and magnetic ordering on the microscale. We provide an overview of fundamental background for Heusler alloys including martensitic transitions and various physical effects exhibited by these alloys in the second chapter. We discuss experimental methods and describe experimental setups used in this work in the third chapter. The fourth chapter is devoted to the discussion of the experimental results, where we discuss the influence of the transitional hysteresis on the magnetocaloric effect in Ni-Mn based Heusler alloys, polarized neutron scattering, and ferromagnetic resonance studies for determining the nature of magnetism in martensite and austenite states. A separate part covers the study of the structure with neutron diffraction under the magnetic field, and a conclusion is provided in the last chapter.

2 Fundamental Background

2.1 General characteristics of the martensitic transition in Heusler alloys

A martensitic transition is a diffusionless structural first-order transition occurring in a wide range of materials; metals, insulators, semiconductors, and organic compounds [29]. The characteristic feature of this transition is that the kinetics and morphology is dominated by lattice distortions and strain energy. The transition is diffusionless but displacive, meaning that atoms in the lattice maintain their local neighbors, and the lattice transformation occurs by the development of distortions and shears. The speed of the transition is at about the speed of sound in the material, exceeding $1000\ ms^{-1}$. The high-temperature parent phase with higher symmetry is referred to as `austenite`, and the low-temperature product phase with lower symmetry is referred to as `martensite`.

The terms austenite and martensite were introduced by the French scientist and engineer Floris Osmond in the beginning of the XXth century [30]. Austenite was named after the English metallurgist William Chandler Roberts-Austen (1843-1902) [31] and originally referred to paramagnetic high-temperature fcc γ-Fe and solid solutions of iron with alloying elements such as Fe-C (plain carbon steels). The term martensite was named after the German metallurgist Adolf Karl Gottfried Martens (1850-1914) and originally referred to the steel crystalline structure obtained by the rapid quenching of Fe-C, noted for its significant hardness.

We show the schematic representation of the temperature dependence of physical properties around the martensitic transition in fig. 2.1(a). Martensitic transitions, being first-order transformations, have the characteristic temperatures martensite-start, martensite-finish (M_s, M_f) and austenite-start, austenite-finish (A_s, A_f). The beginning of the transition can be seen as a rapid change of a physical property with temperature as in fig. 2.1(a). At M_s, the nucleation of martensite domains starts in the austenite lattice during the `forward` transformation, and at M_f, the sample completely turns into martensite. At A_s, the `reverse` transformation starts and finishes at A_f. The difference between start and finish temperatures is taken as the width of the thermal hysteresis, and its significance will be discussed later in this chapter.

From the magnitude of the physical property before and after the transition (fig. 2.1(a)), one can recalculate the temperature dependence of the austenite-to-martensite fraction $\frac{a}{m}$ as shown on fig. 2.1(c).

According to C.W. Wayman and H.K.D.H. Bhadeshia, martensitic transitions can be distinguished from other structural transformations as being *"military"*, i.e., a coordinated movement of the atoms from their positions in the parent phase to their positions in the product phase. This case is opposite to a *"civil"* diffusive transformations, where atoms travel through the phase boundary in an uncoordinated manner. As a result of such coordinated transformation by a slip of the crystallographic planes, deformation occurs, and the sample changes its form on the macro scale. On the microscopic scale, the martensite lattice always bears structural inhomogeneities such as slips, twins and faults. They result in secondary deformation, being intrinsic part of transformation process and providing twin boundaries in product phase and semi-coherent glissile interface between the austenite and martensite phases, also they partially or sometimes completely compensate shape change during the transition. Therefore it is usually not possible to express martensitic transition in exact relations like integral Miller indices [32, p. 1509].

The nucleation of the product phase in the parent lattice results in a change of the elastic and surface energies. We show the temperature dependence of the Gibbs Free energy around the structural transition in fig. 2.1(b). The change in the Gibbs free energy at the transformation can be written as [32, p. 1529]:

$$\Delta G^{A\to M} = \Delta G_C^{A\to M} + \Delta G_{NC}^{A\to M} \tag{2.1a}$$

$$\Delta G^{M\to A} = \Delta G_C^{M\to A} + \Delta G_{NC}^{M\to A}, \tag{2.1b}$$

where $A \to M$ and $M \to A$ denote the direction of the phase transition, ΔG_C is the chemical free energy change per unit volume of the transformation (so $\Delta G_C^{A\to M} = \Delta G_C^{M\to A}$), and ΔG_{NC} is the change in the elastic and surface energies. Therefore, two cases can be discussed yielding large and small G_{NC} changes [33].

In the case when the volume of the parent and product lattices is slightly different, the intrinsic transformation strain is small. Consequently, the structural transformation is close to elastic and is not accompanied by irreversible plastic strain. This results in a small ΔG_{NC}. Therefore, the martensitic transition can show a narrow transitional hysteresis. In the extreme case of the absence of hysteresis, the initial crystallographic state can be completely restored after cycling through the transition. Such a transition is referred to as `thermoelastic`. Elastic accommodation, and thus the restorable property of the states, relies on the small elastic modulus and the high elastic limit of the phases. These properties are important for all observed effects related to martensitic transition, as the restorable nature of the transformation is widely exploited for various applications:

external load: hyperelasticity, rubber-like behavior, training, the conventional shape memory effect, etc. [32, p. 1538-1544]

magnetic field: magnetic shape memory and the magnetocaloric effect [34].

In the case when the parent and product lattices cannot be elastically accommodated, other mechanisms like plastic strain take place, and the motion of interphase boundaries is hampered by structural defects. Therefore, the transition develops mostly by nucleation and growth of individual randomly oriented domains of the product phase inside the parent lattice; instead of a gradual coordinated transformation by slip deformation. In this case, ΔG_{NC} is large. Unlike in the previous case, thermal cycling through the structural transition will result in different austenite structure after each cycle because, each time the high-temperature phase is adopted with different crystalline orientations. And in the extreme case the initial crystallographic state is never be restored as sample get “stuck” in the martensitic phase (obviously it never happens). Such a transition is referred to as `nonthermoelastic`.

It is worth noting that it is difficult to clearly distinguish between thermoelastic and nonthermoelastic martensitic transformations as both are reversible, varying only in the width of the thermal hysteresis. Moreover, this width can change depending on the history of the sample; like thermal mechanical treatment as observed in Cu-Sn, Fe-Pt, and Fe-Co-Ni-Ti alloys, affecting the reversibility.

Prior to considering structural models for lattices, we focus on the magnetic shape memory effect, elastic properties, and the magnetocaloric effect, as they directly depend on the properties of the lattice as discussed above.

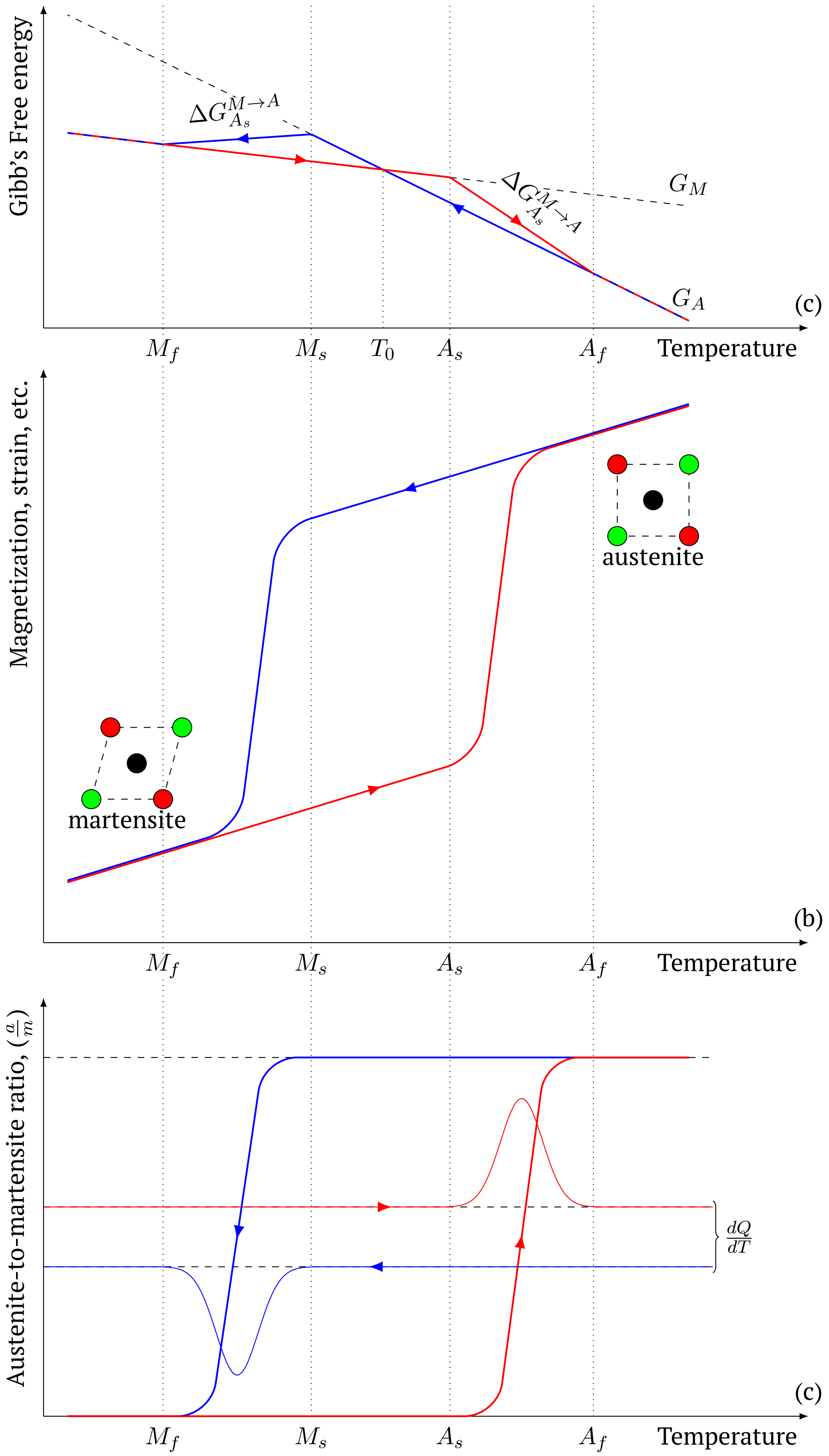

Figure 2.1: Schematic representation of temperature dependence of various physical properties (a), Gibbs Free energy (b), austenite-to-martensite ratio $\frac{a}{m}$ and specific heat $\frac{dQ}{dT}$ (c) around the structural transformation.

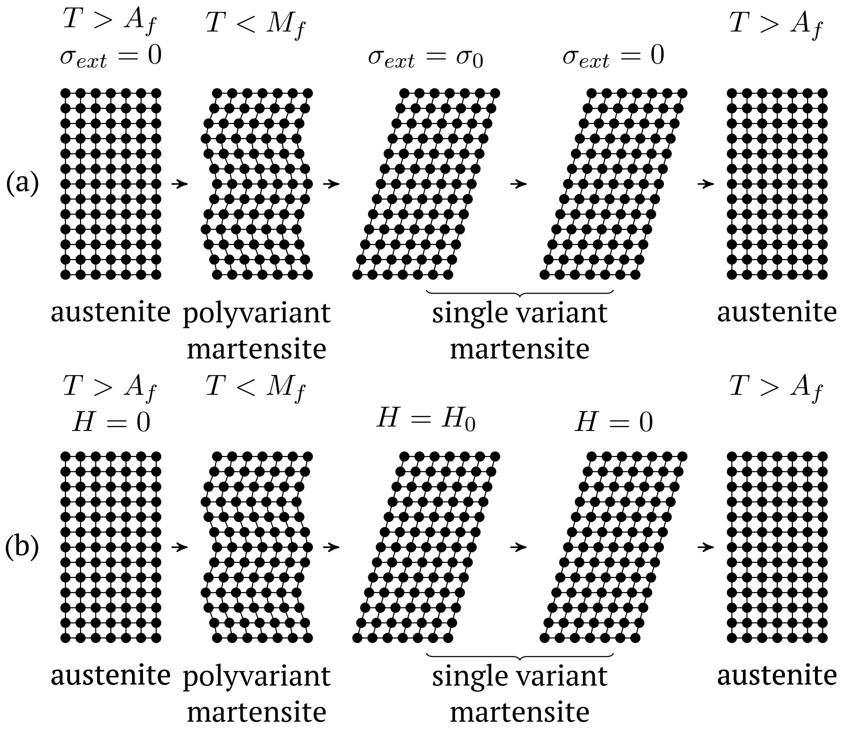

Figure 2.2: Schematic representation of conventional shape memory effect (a) and magnetic shape memory effect (b). Adopted from [34].

2.1.1 Shape memory effects and elastic properties

Among various effects accompanying the thermoelastic martensitic transitions, the `shape memory effect` (SME) is the most extensively studied. The effect can be described as the restoration of sample-shape (originally given in the austenite state) after mechanically deforming the sample in the low-temperature martensitic state and warming it back up to the austenite state. Strains of about 10% can be completely recovered.fig. 2.2(a) shows schematically the process of the shape memory effect.

A thorough explanation of the SME effect is given in [32, 35]. The SME occurs because an applied stress selects an energetically favorable martensite variant causing it to grow by detwinnig. Ultimately, a single variant martensite phase appears with an orientation permitting maximum elongation in the direction of the tensile axis. If a dislocation slip occurs, the SME becomes imperfect. On removing the stress the sample maintains its shape as the deformation is not elastic. Although a single crystal transforms into a polyvariant state during the transition from austenite to martensite on cooling, either polyvariant or single variant martensite transforms back into single crystal austenite on warming. This happens due to the non-diffusive nature of the transition and the austenite and martensite lattice symmetries involved in the transition. Due to its thermoelasticity, the phase transformation brings the sample back to the energetically most favorable “memorized” state as atoms maintain their local neighborhood in the crystal. In the case of a cubic high-temperature lattice, it is even supported by existing many ways to adopt the lattice from poly- or single variant martensite into cubic. In rare cases of non-symmetrical martensite (e.g. monoclinic Cu-Zn-Al alloy), which lacks this variety of ways, the high-temperature phase appears in process of “unshearing” during the reverse transformation.

It is worth noting that in some cases, the shape memory effect occurs in both

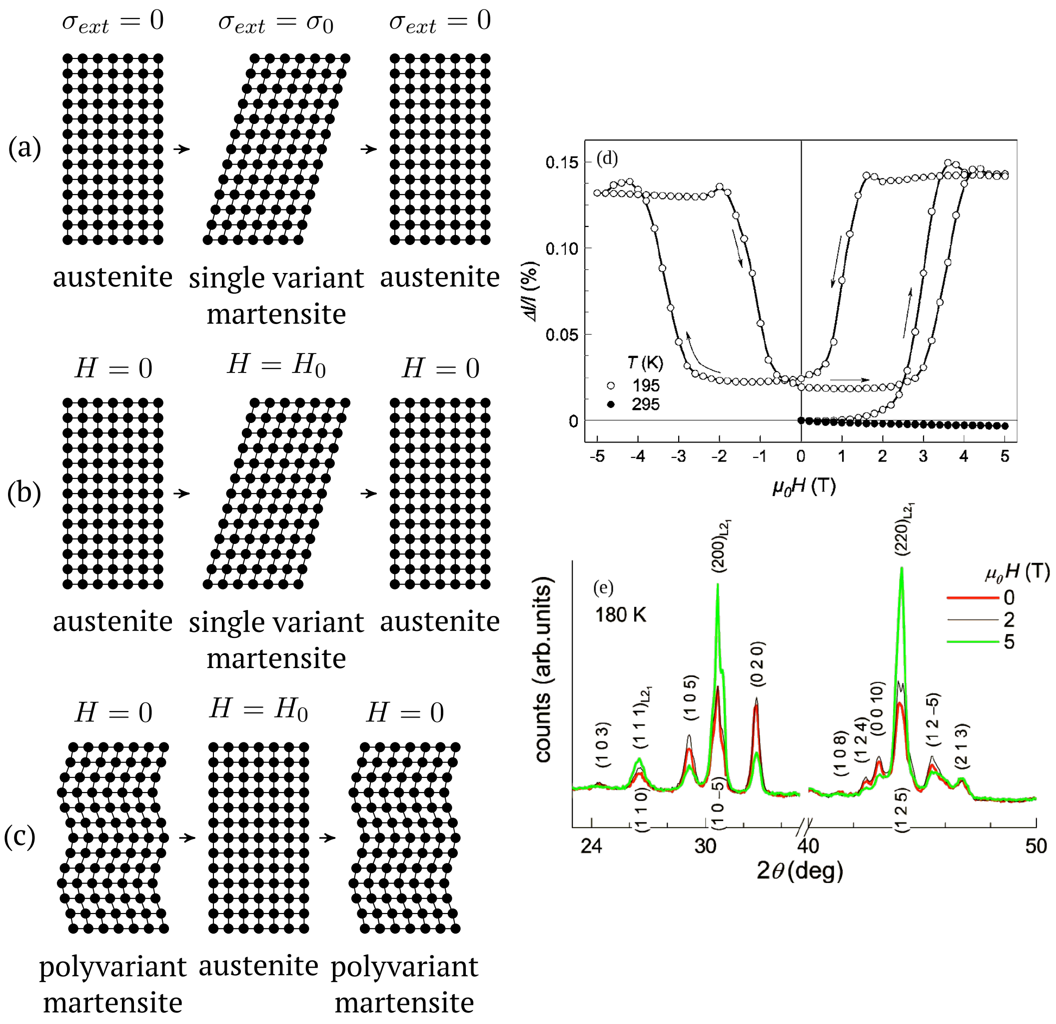

Figure 2.3: Schematic representation of conventional superelastic effect (a) and its magnetic counterparts: forward (b) and reverse (c) magnetic superelastic effects, adopted from [34]. Example for the reverse magnetic superelastic effect in $Ni_{49.7}Mn_{34.3}In_{16.0}$: magnetic-field dependence of strain at $195\ K$ and $295\ K$ (d), neutron diffraction of the field induced transition from martensite to austenite at $180\ K$ (e), taken from [38]

directions of the transition: the material spontaneously deforms during cooling from M_S to M_F and returns to its original shape on warming from A_S to A_F. Such behavior is referred as the `two-way shape memory effect`. It has been shown that this effect occurs due to deformation in either of the phases. Additionally, the sample should be *trained* to be able to exhibit this effect [36, 37].

In materials like Ni-Mn-based Heusler alloys where the magnetic moment is strongly coupled to the lattice, the application of an external magnetic field causes deformation in the martensite state, working in a way similar to mechanical deformation. The case where the shape of the sample deformed by the external field is restored by warming to a temperature at which the parent phase is stable is known as the `magnetic shape memory effect` (MSME). Such behavior is represented in fig. 2.2(b).

Besides the possibility of thermally inducing the martensitic transition, it is possible to stabilize martensite by applying an external stress to the austenitic sample. The resulting martensite will then be single variant as different variants are no more equivalent in energy. This property leads to another important effect of

SME systems called `superelasticity`: a sample in the martensite state, stabilized by external stress, regains it shape as it returns back to the austenite state on removing the stress. This behavior is illustrated in fig. 2.3(a).

This "mechanical" superelasticity has its "magnetic" counterpart: `magnetic superelasticity`. In contrast to MSM, the mechanism of this effect relies not on twin boundary motion, but on stabilizing the phase with higher saturation magnetization isothermally. In fig. 2.3(b), the forward magnetic superelasticity is shown: on applying a magnetic field, the structural transition is induced, and single variant martensite is stabilized. On removing the field, significant shape change occurs as sample turns austenitic.fig. 2.3(c) shows the case of reverse magnetic superelasticity: polyvariant martensite turns into austenite on applying a field and returns back to martensite on removing it. In the latter case, no significant shape change is expected, although due to difference in lattice volumes sample size will change. This effect was studied by T. Krenke et.al in $Ni_{49.7}Mn_{34.3}In_{16.0}$ [38]. Figure 2.3(d) shows the magnetic field induced strain, defined as $\Delta l/l = (l(H) - l)_0/l_0$. At 195 K the initial application of the field induces a strain of about 0.14%, which is not fully recovered, and a strain of 0.12% in further cycles which fully recovers showing superelastic behavior. To show that this behavior is related to inducing austenite by the field, field-dependent neutron diffraction experiments were carried out. In fig. 2.3(e) neutron diffraction of the sample undergoing a field-induced structural transition at 180 K is shown. At zero field, the sample is in a mixed austenite and martensite state. Reflections related to the austenite phase are denoted by $L2_1$. On applying a magnetic field, one can clearly see that the intensity of the reflections from the martensite phase reduces, while the intensity of austenitic reflections grows.

The possibility to stabilize either of the phases by applying a magnetic field also leads to a further effect. Namely, `kinetic arrest`, which is the retarded growth of the low-temperature phase by the supercooled high-temperature phase in first-order transitions. Ito et al. showed kinetic arrest in $Ni_{45}Co_5Mn_{36.7}In_{13.3}$ by means of X-ray spectroscopy, magnetization and electrical resistivity studies [39]. When a high external magnetic field is applied in the austenite state ($T > A_S$) and is cooled, the sample does not transform completely into the martensite state and remains mostly in the austenite state far below M_F (fig. 2.4(a)). When the field is removed at low temperatures, on warming the low-temperature martensite phase slowly grows from supercooled austenite as seen in the diffraction spectra measured at $100\ K$ and $200\ K$. On further warming, the sample fully transforms into austenite at $300\ K$ (fig. 2.4(b)). Magnetization measurements performed on the sample at various fields show that depending on the external field, M_S gradually shifts to lower temperatures at a rate of $\approx\ 10\ K/T$. However at $8\ T$, no transition is observed indicating that the sample remains fully austenitic down to low temperatures (fig. 2.2(c)). A possible explanation of this effect in Ni-Mn based Heusler alloys is that the retarded growth of the martensite phase at temperatures below M_F can be associated with the decrease in the mobility of the habit plane between the parent and the product phase. This hypothesis is supported by resistivity and magnetization measurements. On the other hand, it can be related with the loss of driving force of the transformation, when considered in terms of the Gibbs energy[40, 39].

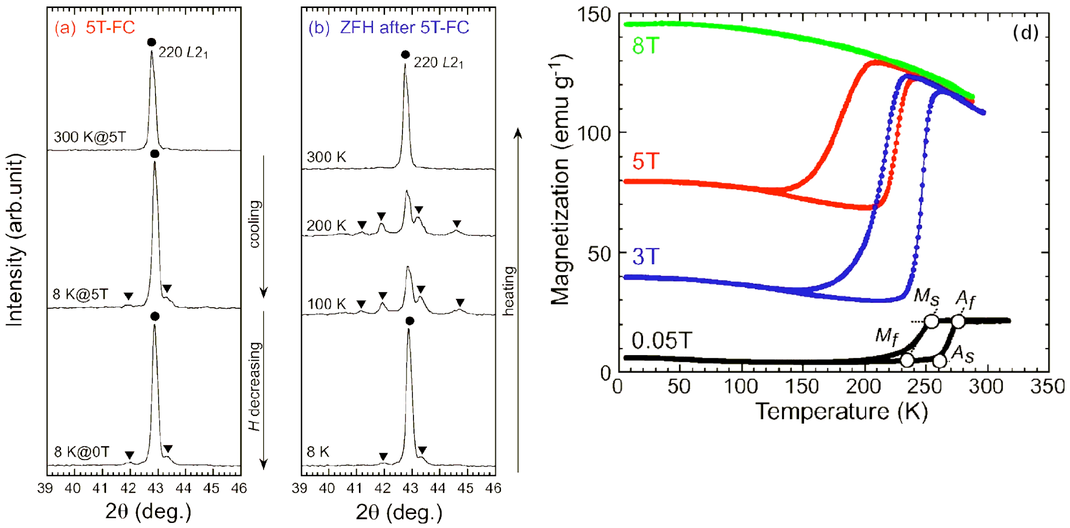

Figure 2.4: Temperature dependent X-ray powder diffraction patterns taken in 5 T field: on cooling (a) and on heating from zero-field-cooled state (b). The filled circle denotes 220 reflection from austenite $L2_1$ phase, arrowhead symbols indicate reflections from martensite phase. Temperature dependence of magnetization measured on heating and cooling at 0.05, 3, 5 and 8 T (c). Taken from [39].

2.2 Magnetocaloric effect in martensitic Heusler alloys

In the previous section we discussed effects occurring due to the interplay between elastic and magnetic anisotropy energies when the system is subjected to external stress, magnetic field, and temperature. This section will be mostly devoted to the discussion on the general theory and application of the magnetocaloric effect in Heusler alloys.

2.2.1 Theory of the magnetocaloric effect

The phenomenon of temperature and entropy-change on the application or removal of an external magnetic field is called the `magnetocaloric effect` (MCE). As both temperature and entropy change on applying a field, the effect is usually described by the isothermal total entropy change ΔS_{iso} and the adiabatic temperature change ΔT_{ad}.

Entropy can be considered as a function of the thermodynamic parameters temperature T, external field H, and pressure p, so that $S = S(T, H, p)$. Thus the total differential of the entropy can be written as

$$dS(T, H, p) = \left(\frac{\partial S}{\partial T}\right)_{H,p} dT + \left(\frac{\partial S}{\partial H}\right)_{T,p} dH + \left(\frac{\partial S}{\partial p}\right)_{T,H} dp. \tag{2.2}$$

In this work, we confine to the isobaric case, i.e. $p \equiv const, dp = 0$, and $\left(\frac{\partial S}{\partial p}\right)_{T,H} = 0$. First, we consider the adiabatic temperature change. Since there is no heat exchange ($\delta Q \equiv 0$) $dS = \frac{\partial Q}{T} = 0$. This assumption leads to the general relation for the temperature-change in a material during adiabatic magnetization under isobaric conditions:

$$dT = -\left(\frac{\partial T}{\partial S}\right)_{H} \left(\frac{\partial S}{\partial H}\right)_{T} dH \tag{2.3}$$

This equation can be further simplified by introducing the heat capacity under constant magnetic field: $C = \frac{dQ}{dT} = T\left(\frac{\partial S}{\partial T}\right)_H$. Although the Maxwell equation $\left(\frac{\partial M(T,H,p)}{\partial T}\right)_{H,p} = \left(\frac{\partial S(T,H,p)}{\partial H}\right)_{T,p}$ does not apply to first order transitions in theory, it is still applicable to these transitions if they occur over a few Kelvin-wide temperature-range [41]. Thus, second term can be rewritten using Maxwell's relation leading to:

$$dT = -\frac{T}{C_H}\left(\frac{\partial M(T, H)}{\partial T}\right)_H dH. \tag{2.4}$$

Finally, integrating this equation gives the value for the adiabatic temperature change for a field change from $H = H_1$ to $H = H_2$:

$$\Delta T_{ad}(T, H) = -\int_{H_1}^{H_2} \frac{T}{C(T, H)}\left(\frac{\partial M(T, H)}{\partial T}\right)_H dH. \tag{2.5}$$

Considering the isothermal change of the entropy in the isobaric case, eq. (2.2) can be simplified as:

$$dS(T, H) = \left(\frac{\partial S}{\partial H}\right)_T dH. \tag{2.6}$$

Again, using Maxwell's equation we rewrite the entropy differential as:

$$dS(T,H) = \left(\frac{\partial M(T,H)}{\partial T}\right)_H dH. \tag{2.7}$$

Finally, integrating this equation gives the value for the isothermal entropy change for a field change from $H = H_1$ to $H = H_2$:

$$\Delta S_{iso}(T,H) = -\int_{H_1}^{H_2} \left(\frac{\partial M(T,H)}{\partial T}\right)_H dH. \tag{2.8}$$

With eq. (2.4), one can estimate the magnetocaloric effect in materials like Fe, Ni, Co and their alloys. In these materials, the magnetization usually decreases with increasing temperature so that $\left(\frac{\partial M(T,H)}{\partial T}\right)_H < 0$, and assuming $C(H,T) \approx const$, the result is a positive temperature change of $\approx 0.1K/T$ on applying a magnetic field and negative on removing the field. Such behavior is referred to as the `conventional MCE`. On the micro-scale, this effect can be explained as the decrease of the magnetic entropy as the external magnetic field gives rise to parallel alignment of magnetic moments in the material. To increase the magnitude of the effect, one can apply the field in the vicinity of 1^{st} and 2^{nd} order transitions, where $C\,(T,H)$ and $\left(\frac{\partial M(T,H)}{\partial T}\right)_H$ change rapidly.

The micro-scale picture is equivalent to the total entropy of the system S_{total} being the sum of contributions from electronic, lattice and magnetic entropies [42, 43]:

$$S_{total} = S_{latt} + S_{magn} + S_e. \tag{2.9}$$

This separation in general is not straightforward, but it is illustrative. In many materials at constant pressure, usually only the magnetic entropy depends on the magnetic field, while the lattice and electronic entropies are field-independent. In Ni-Mn-based Heusler alloys, due to the strong coupling between lattice and magnetic degrees of freedom, the lattice entropy can depend on the magnetic field in vicinity of the structural transition. Also, the heat-capacity exhibits a discontinuity at the first-order transition[44]. Therefore, the theoretical interpretation of the MCE around martensitic is complex.

To discuss the MCE qualitatively, we consider a schematic representation of the temperature dependence of the total entropy $S_{total}(T)$ of the system close to the transition as shown in fig. 2.5. The solid line denotes the zero-field temperature dependence of the total entropy $S_{total}(T)|_{H=0}$, and the dashed line denotes the temperature dependence of the total entropy in an external field $S_{total}(T)|_{H=H_0}$. Figure 2.5(a) shows the case of $S_{total}(T)$ in the vicinity of a second-order (e.g. magnetic) transition. $S_{total}(T)$ for $H = 0$ lies higher than that for $H > 0$ in the whole temperature interval, since the main contribution to the total entropy comes from the magnetic entropy ($S_{total} \approx S_{magn}$), and applying a magnetic field lowers it. Applying a magnetic field adiabatically at T_i^2 leads to a positive temperature change $\Delta T_{ad}^2 = T_f^2 - T_i^2$, while applying a magnetic field isothermally leads to the negative entropy change: $\Delta S_{iso}^2 = S_f^2 - S_i^2$: conventional MCE.

Figure 2.5(b) shows the case of $S_{total}(T)$ in the vicinity of a first-order transition. Below and above the transition, $S_{total}(T)$ for $H = 0$ lies higher than that for $H > 0$. This results in a positive adiabatic temperature change $\Delta T_{ad}^1 = T_f^1 - T_i^1 > 0$, and a negative isothermal entropy change $\Delta S^1 = S_f^1 - S_i^1 < 0$ on applying a field. During the transformation, both magnetic and lattice entropies change, and the applied field stabilizes the state with higher saturation magnetization. This results in a positive total entropy change on applying a magnetic field ($\Delta S_{latt} > \Delta S_{magn}$, $S_{total}(T)|_{H=H_0} > S_{total}(T)|_{H=0}$) and leads to a negative adiabatic temperature change $\Delta T^1_{ad} = T^1_f - T^1_i < 0$ and a positive isothermal entropy change $\Delta S^1 = S^1_f - S^1_i > 0$. This results in the inverse MCE.

From these schematic considerations of the MCE in the vicinity of the thermodynamic transition, it can be understood that both temperature and entropy changes are substantially larger in the vicinity of the transition so that the transition temperature is the most favorable working temperature for MCE applications. Here, the transition is considered to have no hysteresis so that the adiabatic temperature changes on applying and removing the field are equal. However,as martensitic transitions exhibit hysteresis, it is important to consider the influence of hysteresis on the MCE. This is taken into account in section 5.4.1, while we give an overview of possible magnetocaloric applications of Heusler alloys in the next subsection.

2.2.2 Materials for room-temperature magnetic refrigeration

The warming of iron in a magnetic field was discovered by Emil Gabriel Warburg in 1881 [45]. Paul Langevin later showed the reversibility of this effect [46], and later Peter Debye [47] and William Giaque [48] independently proposed the application of this effect for cooling by adiabatic demagnetization. In 1933, temperatures below 1 K were reached using this method [49, 50]. The next milestone in MCE was not reached until 1997 with the discovery of the giant MCE close to room temperature in $Gd_5Si_2Ge_2$ [10] giving rise to the possibility of effective magnetic refrigeration around room temperature [51, 52].

Heusler alloys exhibiting first-order magnetostructural transition show large entropy changes at the transition and are therefore promising materials for MCE applications. The transition temperatures can be varied by varying the material composition (e.g.fig. 2.8) or by further doping of a suitable element. $Ni_{50}Mn_{25+x}Ga_{25-x}$ was the first prototype composition for entropy and adiabatic temperature change investigations.

Further investigations on Heusler magnetocaloric materials covered other Ni-Mn based alloys doped with In, Sn and Sb and further doping of ternary compounds with a fourth transition element. For example, $Ni_{50}Mn_{37}Sn_{13}$ exhibits maximum entropy change of 3.6 $JK^{-1}kg^{-1}T^{-1}$ close to room temperature[14], while $Ni_{47}Fe_3Mn_{37}Sn_{13}$ increases the entropy change up to 5.5 $JK^{-1}kg^{-1}T^{-1}$ [53]. However, in the latter case, M_s drops far below RT. In $Ni_{50}Mn_{34}In_{16}$, the measured entropy change id 1.6 $JK^{-1}kg^{-1}T^{-1}$, while doping with Ga decreases the transition width and shifts the transition to higher temperatures while preserving the value of ΔS.

Among these materials, Ni-Mn-In based alloys appear to be the most promising magnetothermoelasticity in reasonable fields (e.g. 5 T for $Ni_{50}Mn_{34}In_{16}$[38]), thus taking advantage in maximum possible lattice entropy change between both phases ($\Delta S_{lat} = S^{aust}_{lat} - S^{mart}_{lat}$).

As materials showing both inverse and conventional MCE yield large adiabatic temperature changes, both can be used for magnetic refrigeration. A refrigeration cycle with materials exhibiting both types of MCE and thus doubling the cooling power was proposed by [54]. A sketch of such a refrigeration cycle with both effects used is shown in fig. 2.6.

The cycle runs in the sequence ① → ② → ③ → ④. "**I**" and "**C**" denote the inverse and conventional MCE materials that are connected together with a thermally insulating bar. Initially, the system is in equilibrium with a heat bath at ambient temperature at ① with "**I**" in the magnet and "**C**" outside the magnet. Under adiabatic conditions, "**I**" is extracted from the magnet and "**C**" is introduced into it ②,

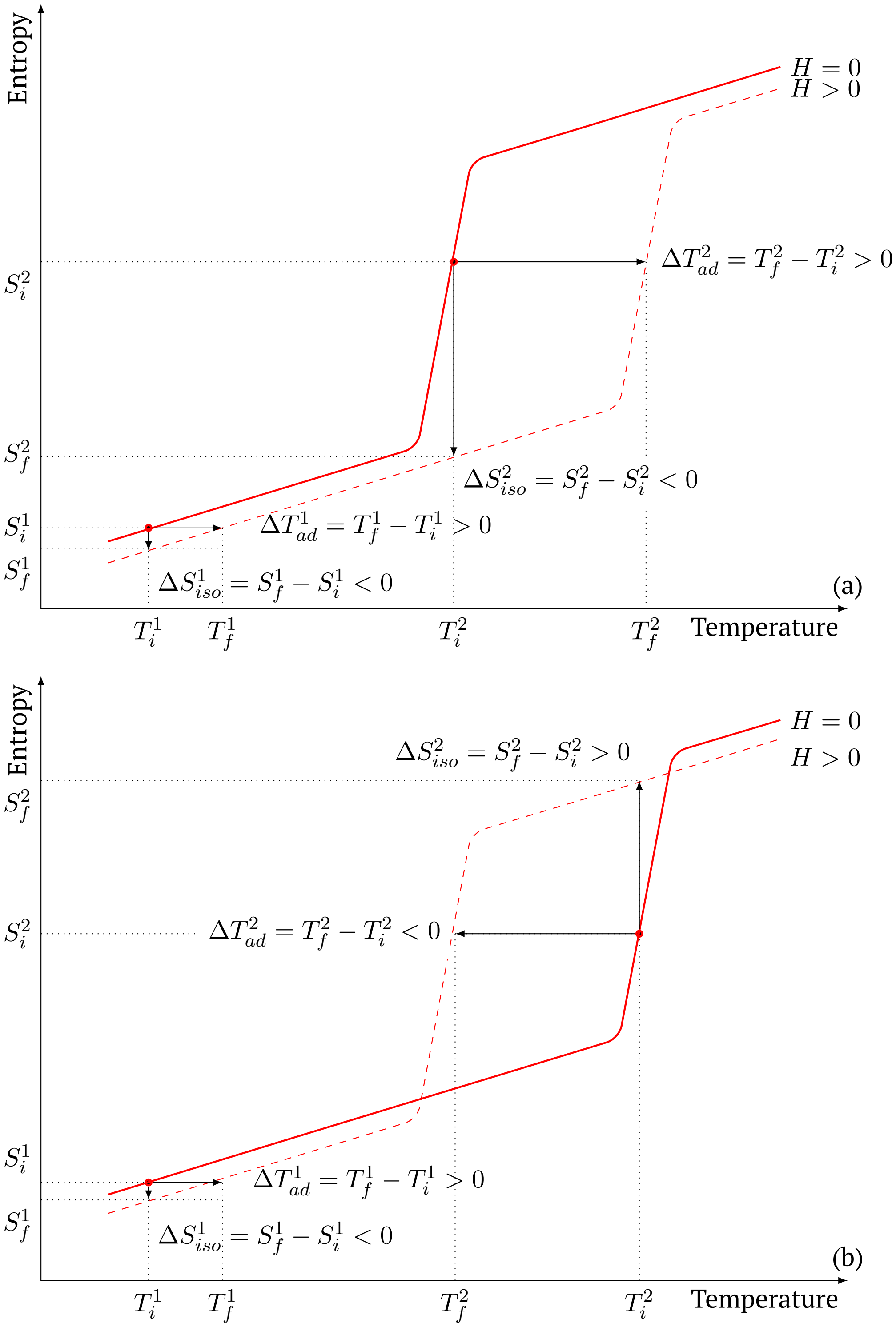

Figure 2.5: Schematic representation of the conventional (a) and the inverse (b) magnetocaloric effects.

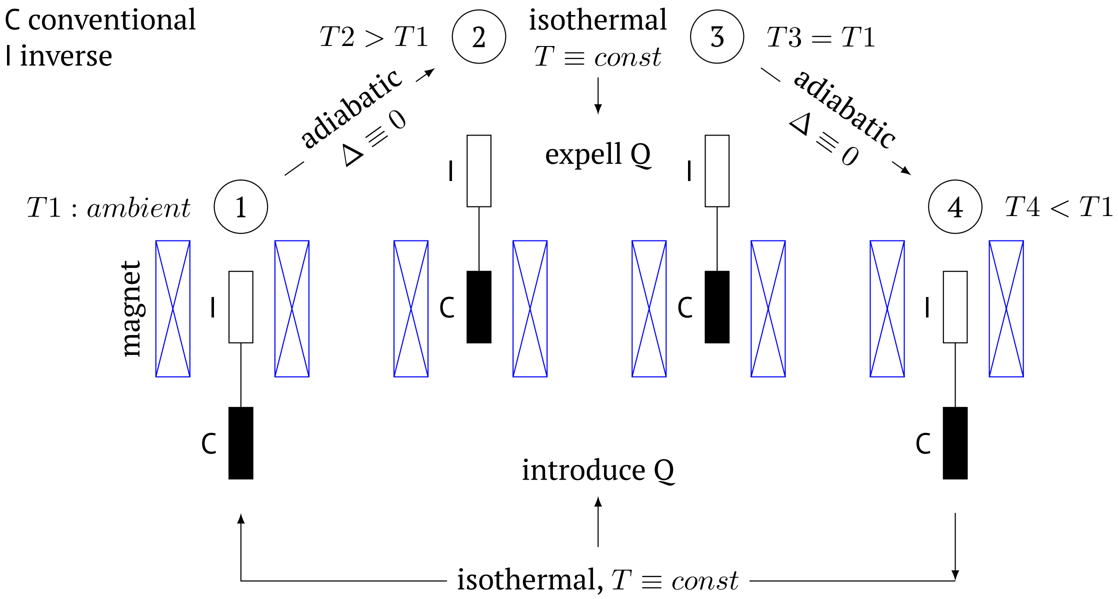

Figure 2.6: A refrigeration cycle using conventional and inverse MCE elements simultaneously, adopted from [54]

in which case both materials warm. The heat Q is then expelled, and both materials return to the bath temperature ③. Then, "**I**" is introduced into the magnet while "**C**" is extracted under adiabatic conditions cooling both materials ④, which can then absorb heat along ④ → ① from the item to be cooled. This cycle shows that using inverse and conventional MCE materials together practically doubles the cooling capacity achieved by a similar cooling scheme that would use only either one of the MCE materials. The feasibility of such a concept relies on finding conventional and inverse active MCE materials with "matching" working properties such as the active temperature-range and the size of the MCE. It is therefore important to understand and tune the properties and the working conditions of both types of MCE materials.

There are restraints for adiabatic temperature changes caused by hysteresis losses (e.g. non-thermoelasticity of the structural transition see section 5.3). Additionally, calculations predict an ultimate limit for the adiabatic temperature change in the vicinity of room temperature as $\Delta T_{ad} \approx 18K/T$, while a more "realistic" estimation would be given in single-digit values [55]. According to the same authors, the efficiency of materials such as Gd ($\Delta T_{ad}^{Gd} \leqslant 3\ K/T$) and FeRh ($\Delta T_{ad}^{FeRh} \approx 6.5\ K/T$) probably will never be surpassed. On the other hand, this estimation takes into account only the magnetic entropy change ΔS_{magn}. This estimation can be suitable for second-order magnetic transitions, whereas in Heusler alloys the MCE is usually exploited for the first-order magnetostructural transition, where both magnetic and lattice entropy changes are considerable and lead to an adiabatic temperature change.

2.3 Structural and magnetic properties of Ni-Mn-based martensitic Heusler alloys

2.3.1 Phase diagram

Properties exhibited by Heusler alloys are strongly dependent on their structure and composition. Here, we introduce the phase diagrams for Ni-Mn-based Heusler alloys.

p-*T* or *p*-*V* phase diagrams are mostly used for gases. In the case of binary alloys and compounds, the compositional dependence of physical properties on temperature is usually represented as 2-D graph: T vs. A_xB_{1-x} phase diagram. Although depictive, such a representation has limitations for ternary alloys; as only a 2-D section of the 3-D phase diagram can be easily plotted on paper. Thus, ternary phase diagrams are usually depicted either as a triangular section at constant temperature with axes corresponding to the ratio of elements ($A_x - B_y - C_z$), or a section including temperature (e.g. T vs. $B_y - C_z$) similar to that in binary phase diagrams. The latter representation is used in the following for the phase diagrams of martensitic Ni-Mn-based Heusler alloys.

For the studies on Ni-Mn-Heusler alloys, the compositional row $Ni_{50}Mn_{50-x}Z_x$ (where Z = Ga, In, Sn, Sb) was usually chosen as a prototype based on several considerations. Off-stoichiometric Mn-rich $Ni_{50}Mn_{50-x}Z_x$ alloys undergo a martensitic structural transition from the cubic austenite phase to the tetragonal martensitic phase. Antiferromagnetic binary alloy $Ni_{50}Mn_{50}$ undergoes a structural transition from the cubic η to tetragonal η' phase at $M_s \approx 1000\ K$ [64, 65]. Additionally, keeping the Ni concentration constant at 50 at. % assures that Ni remains in its own sublattice so that the main changes in the system are brought about by concentration changes of Mn and the Z element. These considerations define the choice of the phase diagram. The section of the ternary phase diagram follows the $Ni_{50}Mn_{50-x}Z_x$ line, where x is in atomic %, and $x \in [25, 50]$. However, it is possible to “generalize” this parameter noting that the concentration of valence electrons in the alloy is proportional to the composition. Thus, one can introduce the valence electrons per atom (i.e. valence electron concentration) e/a as a general phase parameter, as in the Slater-Pauling curve. Introducing e/a also helps in defining the influence of the doping element on certain properties of ternary and even quaternary Heusler alloys as will be shown.

In fig. 2.8, we show the phase diagram of $Ni_2 - Mn - Z$ Heusler alloys with Ga, In, Sn and Sb as Z element. The magnetic and structural transformation temperatures and observed austenite and martensite structures are plotted versus e/a. Empty circles mark the structural transition temperatures M_s of martensitic alloys. The label `cubic` lying above the M_s line denotes the parent cubic phase (austenite) for all Heusler alloys. Labels $L1_0$, **10M**, **14M** and **4O**, lying below M_s denote various product tetragonal phases (martensite). We discuss these lattice structures in more detail in the following section 2.3.2. In each phase diagram, the top right open circle at $\frac{e}{a} = 8.5$ denotes M_s for the $Ni_{50}Mn_{50}$ alloy. With increasing concentration of the doping Z-element (and thus decreasing e/a), the transition temperature decreases until a critical e/a, below which the alloy does not transform martensitically and remains in cubic austenite phase.The structure of the martensite phase also depends on e/a: Alloys with higher e/a transform into the tetragonal $L1_0$ (**2M**) phase, while alloys with lower e/a generally transform into more complex modulated **10M** and **14M** phases. In general, the low temperature phase develops from **2M** $\rightarrow$ **10M** $\rightarrow$ **14M** with decreasing e/a, and eventually remains cubic; although in the case of the $Ni - Mn - Sn$ compositional series, **4O** and **7M** structures are observed in a narrow region below the $L1_0$ region. However, there are reports on the observation of **10M** [62, 63] and **2M** [66] structures in this range. The slope of the temperature dependence of $M_s(T)$ and the critical e/a-value depends on the Z-element, so the slope becomes higher as e/a increases when the doping element Z changes as $Ga \to In \to Sn \to Sb$.

It is clearly seen how sensitive the properties of given alloys are to the composition. A change of 0.1 e/a, corresponding to a change of about 3% in composition, results in a change of the transition temperature of about 80 K for $Ni - Mn - Ga$, and about 200 K for $Ni - Mn - Sb$ alloys.

Filled circles mark the magnetic transitions T_C^A and T_C^M in austenitic and martensitic states, respectively. We discuss the magnetic transition in the martensitic state in more detail in the following subsection in section 2.3.3. Labels `PM` and `FM` lying above and below T_C^A denote the paramagnetic and ferromagnetic states of the austenite phase, respectively. As shown in the graph, T_C^A slowly decreases with increasing e/a, while T_M^C abruptly drops.

2.3.2 Structural properties

On solidifying, most Ni-Mn-based Heusler alloys form a partially ordered cubic B2 phase except for Ni_2MnAl which exhibits order-disorder transitions $L2_1 \leftrightarrow B2 \leftrightarrow A2$ at 990 K and 1220 K, respectively[69, 70]. In the case of $Ni_{50}Mn_{50-x}Z_x$, Ni atoms occupy the corner $(0,0,0)$ positions of the cell, while Mn and Z atoms are randomly distributed at the body center $(\frac{1}{2},\frac{1}{2},\frac{1}{2})$ positions (see fig. 1.1(b)). On further cooling, the order-disorder transformation to the $L2_1$ phase occurs. The maximum transition temperature is slightly below 1100 K for Ni_2MnGa and $Ni_{50}Mn_{27.5}In_{22.5}$ and decreases when deviating from these compositions [71, 72].

In the stoichiometric case (Ni_2MnZ), the Ni atoms occupy the *8c* positions $(\frac{1}{4},\frac{1}{4},\frac{1}{4})$, Mn atoms occupy the *4b* positions $(\frac{1}{2},\frac{1}{2},\frac{1}{2})$, and Z atoms occupy *4a* positions $(0,0,0)$ in the $L2_1$ phase (see fig. 1.1(a)). If the Ni concentration increases, Ni atoms start occupying Mn and Z sublattices, while a change in Mn and Z concentrations leads to disorder at *4a* and *4b* positions, e.g. increasing Mn concentration and keeping Ni concentration at 50 at.% results in Ni remaining at *8c* positions, while Mn occupies its own sublattice and random positions in the Z sublattice.

Stoichiometric Ni_2MnGa and some off-stoichiometric Ni-Mn-based alloys undergo martensitic transformation on cooling from $L2_1$ phase to martensitic phase. This resulting phase has lower symmetry than the parent phase and forms one of several types depending on the sample composition as shown in fig. 2.8. In fig. 2.9 we show the projection of various types of martensitic cells on the *(001)* plane. Figure 2.9(g) indicates the main crystallographic directions in this plane. As can be seen from the graph, `a` and `c` lattice parameters lie in-plane, while `b` lies perpendicular to the plane and defines the z axis depth or “thickness” of the picture.

Thus, the *parent* `bcc` $L2_1$ (austenitic) cell projects as the `bct` cell with $a_{bct} = c_{bct} = a_{bcc}$, $b \neq a_{bcc}$ fig. 2.9(a). We additionally show the dashed outline of the parent phase on each panel in fig. 2.9(b)-(f).

Figure 2.9(b) shows a unit cell of the simplest *product* martensitic structure. It consists of two $L1_0$ cells stacked in the *[001]* direction. Therefore, this structure is sometimes referred to as **2M**(see fig. 1.1(d)). Its lattice parameters are $a_{2M} = c_{2M} = \frac{\sqrt{2}\cdot a_{bcc}}{2}$, $(b_{2M}/a < 1)$. As an example, the martensitic phase of $NiMn$ is of this particular lattice type.

Further types of martensitic Heusler alloy lattices are modulated and also sometimes skewed **2M** cells.

According to the notation introduced by Ōtsuka [73], these lattices are referred to as **nM** or **nO**, where n is the number of layers stacked, while the letter **M** stands for the monoclinic, unit cell and **O** stands for the modulated orthorhombic unit cell.

Thus, **10M** and **14M** stands for the monoclinic structure consisting of 10 or 14 layers, respectively (fig. 2.9(c) and (e)).Sometimes, **10M** and **14M** structures are also referred to as **5M** and **7M** structures, indicating a modulated structure with periodicity of 5 or 7 $L1_0$ unit cells, respectively. Additionally, the **10M** structure can be represented as stacked or sine wave modulated layers as shown in fig. 2.9(c) and (d), respectively. The other possible martensite structure is the 4-fold orthorhombic denoted as **4O** (fig. 2.9(e).

It is also worth mentioning that yet another approach to the martensite structural model was introduced recently. In this model, a modulated martensite structure is represented as nanotwinned variants of the tetragonal martensite phase [74].

2.3.3 Magnetic properties

Full-Heusler alloys that do not transform martensitically (such as stoichiometric $Ni_{50}Mn_{25}Z_{25}$, where $Z = In, Sn, Sb$) behave as a typical ferromagnet; e.g., measured ZFC, FC, FW curves are identical. The magnetization $M(T)$ is constant up to the second order ferromagnet-paramagnet transition (referred to as Curie temperature of the austenite state T_C^A). The magnetization curves $M(H)$ show saturation above $\approx 1\,T$ below Curie temperature, while above the Curie temperature $M(H)$ is linear at lower fields and saturates at higher fields due to the presence of the short FM correlations[24, 25, 61].

Off-stoichiometric Mn-rich $Ni_{50}Mn_{50-x}Z_x$ alloys and stoichiometric $Ni_{50}Mn_{25}Ga_{25}$ undergo martensitic structural transition from austenitic FM correlated state to the low temperature martensite state with complex magnetic structure. Mn-Mn distances change during the structural transition resulting in the change of magnetic interactions in the crystal lattice. These changes give rise to phenomena absent in austenitic Ni-Mn-based Heuslers; e.g., the splitting between ZFC and FC magnetization curves show an abrupt drop at the structural transition temperature and a smeared out magnetic transition in the martensitic state. Additionally, exchange bias effects and large magnetoresistance are also observed in the martensitic state.

Altogether, these phenomena can be explained by the hypothesis that in martensitic Heuslers, Mn-Mn atoms in the lattice can coupled antiferromagnetically in addition to the ferromagnetic coupling. However, contrary to the case of FM coupling, AFM coupling is short-range. Empirically, this idea is supported by the fact that in tetragonal η''-phase of $NiMn$, neighboring Mn atoms also couple antiferromagnetically [60, 75]; also as in the case of stoichiometric Ni_2MnAl featuring smaller cell parameters (in Ni_2MnAl $a = 5.82$ $\mathring{A}$ vs. $a \geqslant 6.0$ $\mathring{A}$ in other Ni-Mn-Z alloys, Ni_2MnGa $a = 5.822$ $\mathring{A}$). Mn atoms form an AF cone spiral magnetic structure [76]. However, recent Mössbauer experiments on Fe-doped $Ni_{50}Mn_{36.5}{}^{57}Fe_{0.5}Sn_{13}$ and $Ni_{50}Mn_{34.3}{}^{57}Fe_{0.5}In_{15.2}$ samples showed no difference between spectra measured below M_s and above T_C^A[26, 27]. In other words, according to these studies, the low-magnetization region in the martensitic state is also paramagnetic, as in the high temperature region above T_C^A.

In contrast to these results, neutron diffraction experiments on $Ni_{50}Mn_{36}Sn_{14}$, $Ni_{50}Mn_{37}Sb_{13}$ and $Ni_{46}Mn_{41}In_{13}$ suggest the presence of the short range AF Mn-Mn coupling, which increase with the growth of the martensite phase [68, 66, 67].

More recently, experiments on neutron polarization analysis were performed on $Ni_{50}Mn_{37}Sn_{13}$ and $Ni_{50}Mn_{40}Sb_{10}$ powder samples. These have demonstrated the presence of AF correlations in the martensite phase in the temperature region between $T_s^M < T < A_s$ along with mixed AF/FM correlations above T_C^A; e.g, in the

$Ni_{50}Mn_{40}Sb_{10}$ sample the magnetic cross sections σ^{mag} in the martensite state above $1.5\mathring{A}^{-1}$ are identical to the magnetic cross sections in the austenite state [28].

Additionally, ferromagnetic resonance experiments performed on $Ni_{1-x-y}Mn_xGa_y$ [77], $Ni_{49.1}Mn_{35.4}In_{15.5}$ and $Ni_{49.9}Mn_{37.0}Sn_{13.1}$ [78] powder samples showed both FM and AF resonance lines below M_s suggesting the presence of mixed AF/FM interactions in the martensite states in these alloys. These experimental results are also supported by density functional theory (DFT) calculations. The results suggest the presence of mixed AF/FM coupling either in the martensite or in the austenite states [79, 80].

These facts are the evidence for the presence of mixed AF/FM correlations in martensite. We consider now some characteristic $M(T)$ dependencies observed in various Ni-Mn-based martensitic Heusler alloys and discuss them in view of magnetic ordering in these materials following [56].

Figure 2.10 shows $M(T)$ for $Ni-Mn-Z$ Heusler alloys (Z = Ga, In, Sb, Sn), undergoing structural transition in temperature range between $200\ K < M_s < 300\ K$ in $5\ mT$ field. $M(T)$ measured under ZFC, FC, FW protocols (the exact protocol descriptions are given in section 3.2) in a low magnetic field of $5\ mT$ are shown in fig. 2.10(a)-(d).

All samples show the same abrupt drop of the magnetization just below the martensite start M_s temperature, attributed to the structural transformation, and discrepancy splitting between ZFC and FW branches of the $M(T)$. Except for $Ni-Mn-Ga$, all samples share the same features in the magnetization dependencies: the drop in $M(T)$ below M_s is followed by slow rise of the magnetization towards lower temperatures. This feature is non-hysteretic and attributed to the magnetic ordering temperature in the martensitic state T_C^M. The splitting between ZFC and FW branches can be connected on the one hand to the presence of AF correlations, pinning FM matrix to different spin configurations depending on the presence of the cooling field. On the other hand, it is related to the magnetocrystalline anisotropy of the FM state below T_C^M, which leads to exchange-bias effects. Thus, the rapid increase in the magnetization in the ZFC branch in the lower temperature region is referred to as the blocking temperature T_B (see fig. 2.10(d)), below which enhanced magnetic anisotropy exists. Actually, the ZFC branch should start from zero magnetization, but the non-zero remanent field of the magnetometers is the reason for $M > 0$.

While the magnetic order-disorder transition in FM austenite state leads to the abrupt drop of the magnetization on heating above T_C^A, the transition around T_C^M is smeared out suggesting the presence of non-FM entities preventing FM alignment of spins. As shown earlier, these entities are short range AF interactions between Mn-Mn nearest neighbors in the Heusler lattice.

In contrast to this, in the $Ni-Mn-Ga$ sample (fig. 2.10(c)) $M(T)$ is nearly constant below the martensitic transformation, so T_B does not exist, and it is difficult to attribute T_C^M in this case. According to [81, 82], in this case $T_C^M > T_C^A$. The reason for this is that $Ni-Mn-Ga$ features high twin-boundary mobility and large magnetocrystalline anisotropy in the martensitic state. This leads to a partial orientation of the martensite variants along the easy axis even in low fields.

In fig. 2.10(e), $M(T)$ measured with the FC protocol in a high magnetic field of $5\ T$ is shown. As seen from the graph, the characteristic drop in $M(T)$ on cooling below M_s does not vanish and remains distinct in fields above the saturation field for all samples except for $Ni-Mn-Ga$, for which the saturation magnetization of martensite is higher than of the austenite. This means that non-FM entities do not weaken, and FM ordering is still disturbed in high fields leading to lower saturation magnetization in the martensite phase. Additionally, the temperature where the drop is observed, shifts with the application of magnetic fields. Therefore, the magnetic field stabilizes the phase with higher magnetization, so that the phase can be induced with the application of an arbitrary field. This is known as `magnetic superelasticity`.

On the other hand, $M(T)$ in $Ni_{50}Mn_{27}Ga_{23}$ slightly rises on cooling below M_s in $5\ T$ so that the saturation magnetization of the martensite phase is higher than in the austenite phase. This feature is explained by the coexistence of the high twin-boundary mobility and the large magnetocrystalline anisotropy in Ni-Mn-Ga Heuslers: martensite variants align with the external field, and this effect overweighs any influence from non-FM entities. Similar behavior of $M(T)$ in high fields is exhibited by martensitic Ni-Fe-Ga Heusler alloys, where high twin-boundary motion and large magnetocrystalline anisotropy are also observed [83].

As a conclusion we emphasize that one should perform low and high-field temperature dependent magnetization measurements to determine the characteristic temperatures of the magnetic and the structural transitions in the martensitic Heusler alloys. One measurement should be done in a magnetic field above the saturation field ($H \geqslant 1.0\ T$, also referred to as `high-field`) on heating and cooling (referred as FW and FC measurements, respectively). In-field structural transitions are seen as the temperature hysteresis in the magnetization curves and the transition temperatures can be derived from these data. However, it is difficult to determine the T_C from this data, since magnetic order-disorder transition is smeared out in high field.

The other measurement is one that is performed in a magnetic field far below the saturation field (e.g. $H \approx 5\ mT$, also referred to as `low-field`) so that the initial susceptibility is measured. This measurement is performed on heating from the zero field cooled state, then on cooling and heating in field (ZFC, FC and FW measurements, respectively). These data give information on magnetic order-disorder temperatures in the martensite and austenite phases (T_C^M and T_C^A, respectively) and on structural transition temperatures. Additionally, the field-induced shift of the transition temperatures can be derived by comparing high-field and low-field magnetization data. By comparing ZFC and FW branches at low temperatures, one can estimate the value of the magnetic anisotropy in the sample.

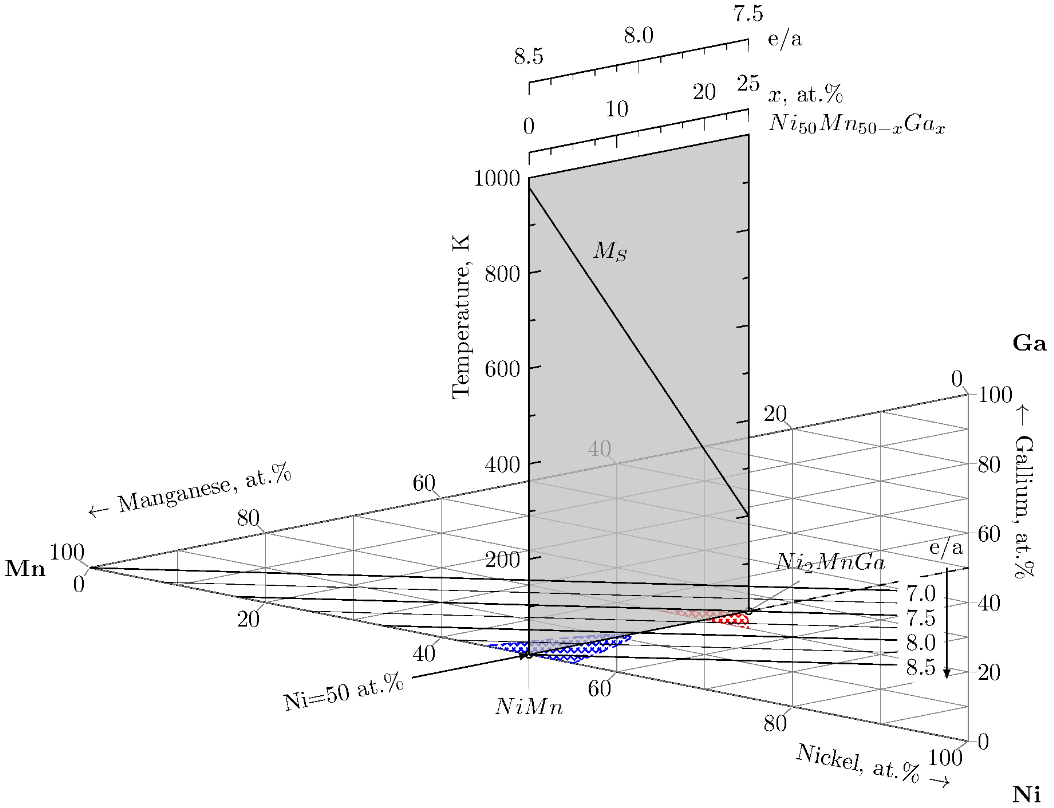

Figure 2.7: Sketch of the ternary phase diagram of $Ni - Mn - Ga$ alloy, showing how the e/a phase diagram is formed on top of it.

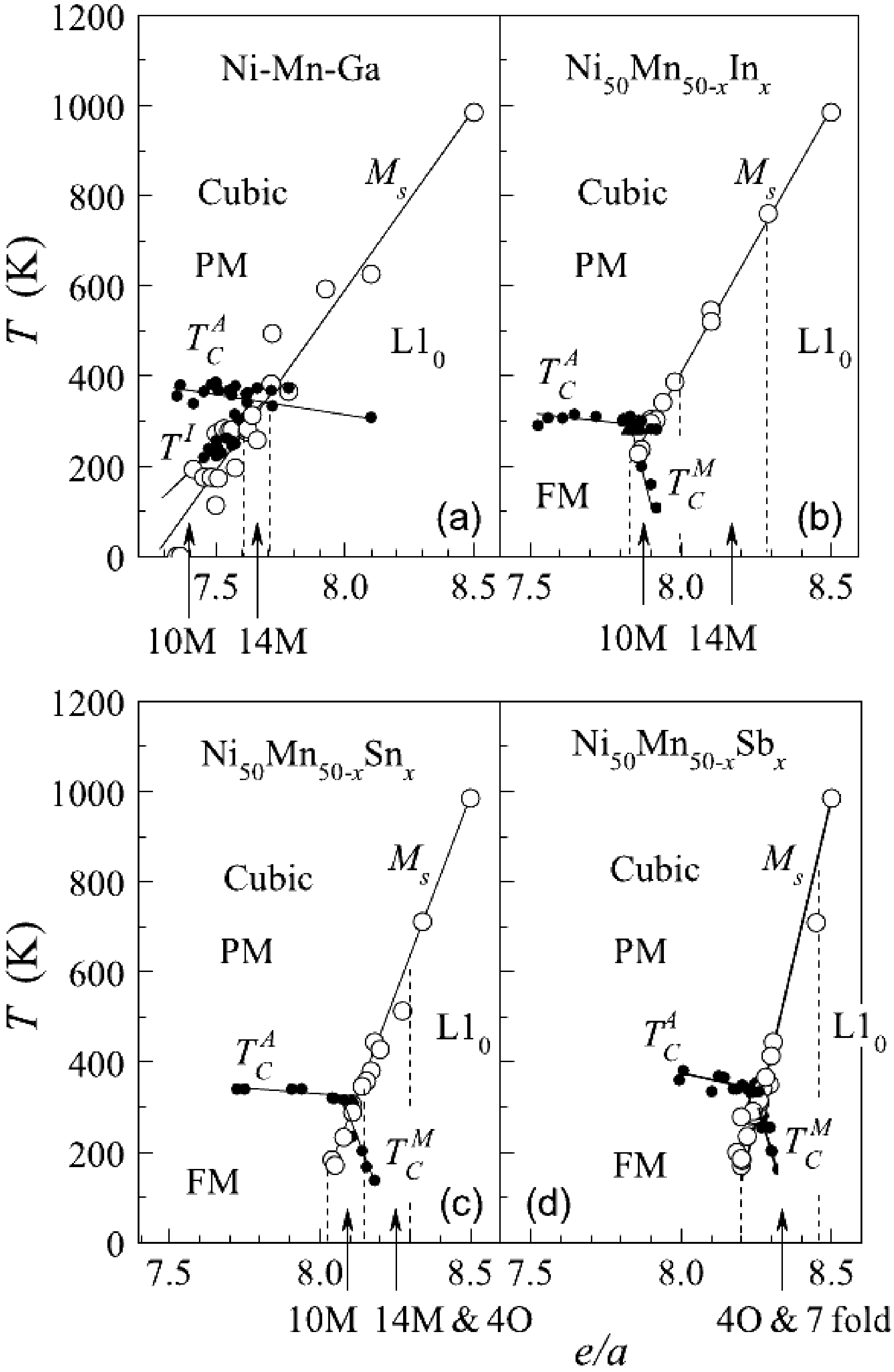

Figure 2.8: Phase diagram of Ni-Mn-Z Heusler alloys with Z as Ga (a), In (b), Sn (c) and Sb (d). The filled and open circels correspond to the magnetic and martensitic transformation temperatures respectively. The regions corresponding to the different structures are separated by dashed lines, taken from [56]. Plotted data is based on following papers: Ni-Mn-Ga [57]; $Ni_{50}Mn_{25-x}Sn_x$ [24, 58, 59]; $Ni_{50}Mn_{25-x}In_x$ [25, 58, 60]; $Ni_{50}Mn_{25-x}Sb_x$ [61, 62, 63].

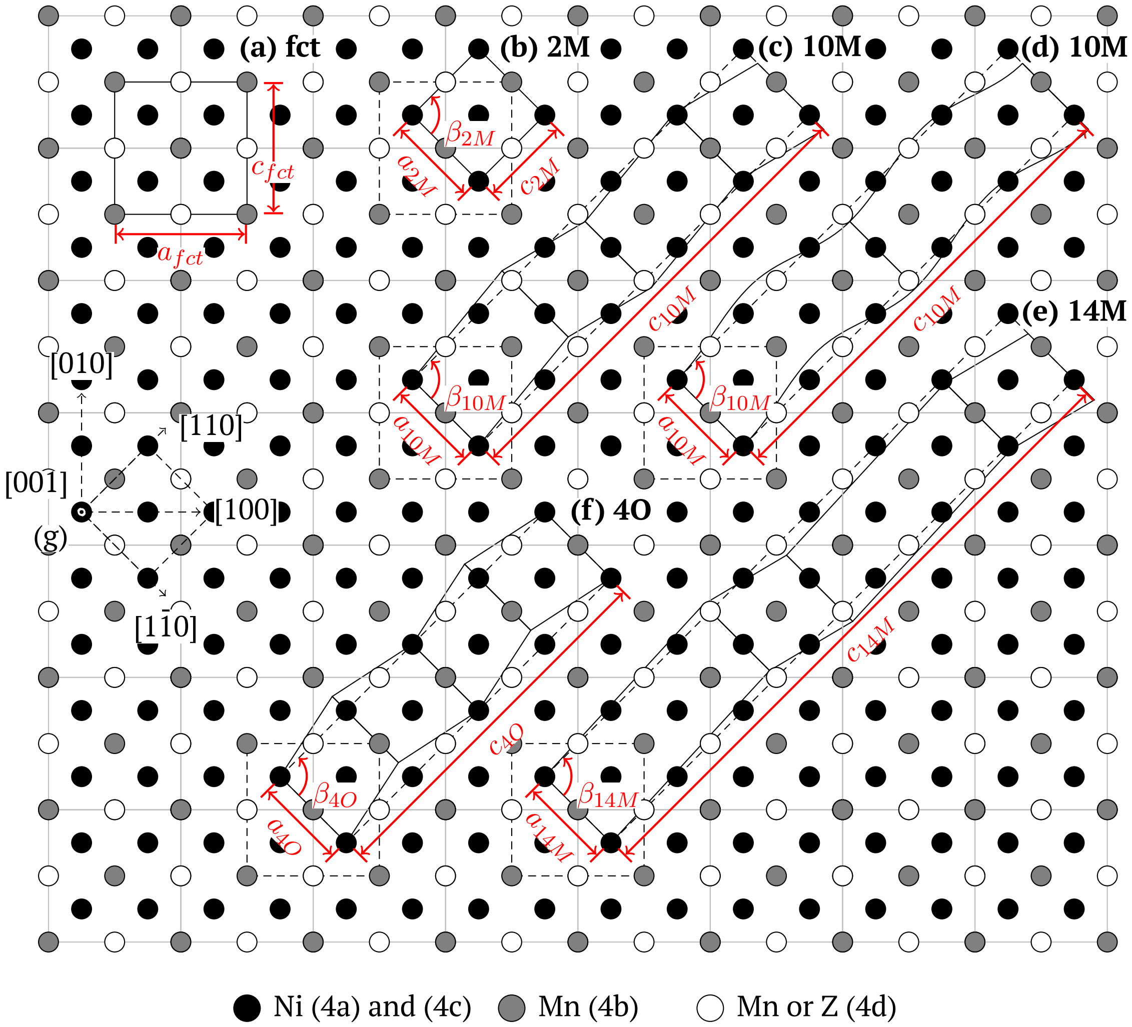

Figure 2.9: Projections of the face-centered tetragonal (a), **2M** (b), **10M** stacked (c) and modulated (d), **14M** (e), and **4O** ($Pmma$) (f) structures observed in Ni-Mn based Heusler alloys on `b (001)` axis. (g) indicates the main crystallographic directions in this plane. Dashed arrows relate certain directions in crystal lattice, based on original cubic cell. Dashed lines represent parent orthorhombic cell for each martensitic cell, depicted by solid lines. a, c and β relate lattice parameters of each martensitic cell. In each case b axis is $[001]_{cubic}$. Adopted from [67, 68, 27].

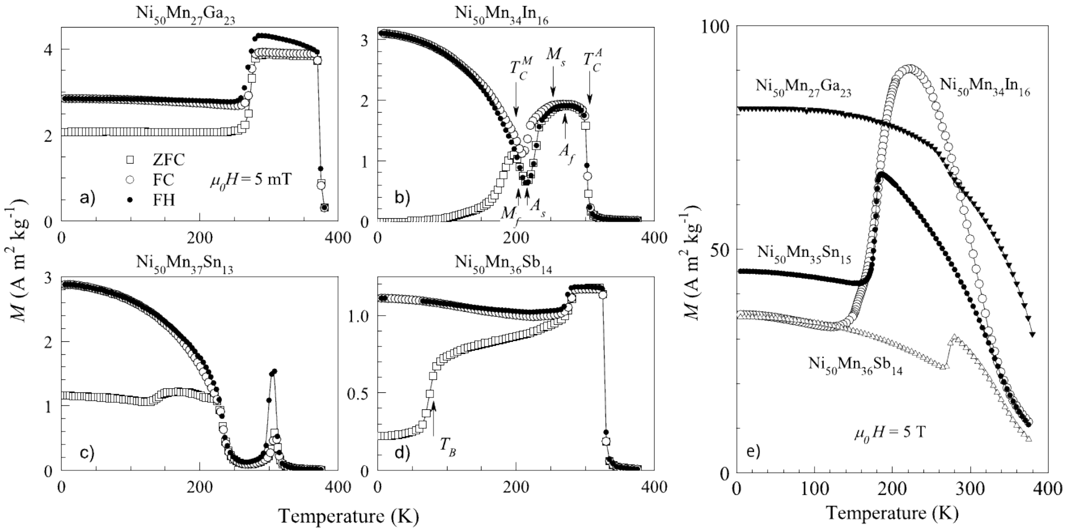

Figure 2.10: The temperature dependence of the magnetization $M(T)$ for $Ni-Mn-Z$ martensitic Heusler alloys (Z: Ga, In, Sb, Sn) measured in 5 mT under ZFC, FC, FW protocols ((a) - (d)) and in $5\ T$ under FC protocol (e). The compositions of the alloys are chosen so that they undergo a martensitic transformation in the range of about $200\ K < M_s < 300\ K$ in 5 mT field (after [24, 25, 61, 34, 56]).

2.4 The choice of the samples

Selection of the samples for the investigation of magnetic interactions in Heusler alloys

As we showed above, the magnetic and structural properties of Ni-Mn-based Heusler alloys depend on doping element Z and specific electron concentration e/a. Additionaly, we showed that antiferromagnetic coupling of Mn atoms in the lattice plays key-role in magnetism of Heusler alloys and stabilizes martensitic structure at low temperatures. We are using concentrational lines of $Ni - Mn - Ga$ and $Ni - Mn - Sn$ based samples for the investigation of the magnetic order in Ni-Mn-based Heusler alloys. In these series we choose samples with stoichiometric $Ni_{50}Mn_{25}Z_{25}$ composition, where Z denotes Ga or Sn, Mn-rich ($> 25\ at.\%$ of Mn) and Mn-poor ($< 25\ at.\%$ of Mn) compositions, where Mn occupies part of Z element sublattice, and Z element occupies part of Mn sublattice, respectively. We also prepared Ni-rich, Mn-poor $Ni_{55}Mn_{20}Z_{25}$ sample, where Ni occupies part of Mn sublattice.

Additionally to these ternary alloys, we used quaternary $Ni_{45}Co_5Mn_{35}In_{15}$ alloy. This alloy exhibits low magnetization in a wide temperature range in the martensitic state. Also it undergoes structural transition from FM/AF martensite to ferromagnetic austenite.

Selection of the samples for the investigation of field-cycling dependence of the adiabatic temperature change

Ni-Mn-based Heusler alloys doped with In and Sn show large field-induced adiabatic temperature change ΔT_{ad} of several degrees K around the structural transition. However, on the further applications of the magnetic field ΔT_{ad} decreases. In this work we choose $Ni{-}Mn{-}Sn$ and $Ni{-}Mn{-}In$ samples, exhibiting martensitic transition close to the room temperature, to analyze their field-cycling properties in connection to their transitional hysteresises. Additionaly, we used $Ni-Mn-In$ sample doped with Sn to see if there is a transtion between the field-cycling effects exhibited by the ternary alloys.

Selection of the samples for the field-dependent neutron diffraction

As I showed in previous chapter martensitic transition temperature M_s of a Ni-Mn-based Heusler alloy with a given composition depends on both stress and magnetic field applied to the sample. External magnetic field can shift M_s temperature by several degrees K by T and also partially stabilize high temperature austenite phase below structural transition temperatures. Additionally, application of an external field may lead to the nucleation of the martensite in the preferred orientation, thus leading to internal stresses unfavorable for the full stabilization of the martensite phase. The latter affects both magnetocaloric and magnetic shape-memory effects exhibited by Ni-Mn-based Heuslers. To investigate the effect of the external magnetic field we chose field dependet neutron diffraction technique as possible internal stress will lead to texturing and thus additional peaks on the diffraction spectra. We chose $Ni - Mn - In$ alloy for this study as in this material the austenite arrest effect is particularly stronger than in the other $Ni - Mn$-based Heusler alloys, and the field shift of M_s in $Ni - Mn - In$ is sufficiently large, about $10\ K/T$.

Target composition	concentration, at%			e/a	
	Ni	Mn	Z		
$Ni_{55}Mn_{20}Sn_{25}$	54.65	19.29	26.06	7.86	ferromagnetic resonance and neutron polarization measurements
$Ni_{50}Mn_{25}Sn_{25}$	49.71	23.98	26.31	7.70	
$Ni_{50}Mn_{35}Sn_{15}$	49.38	34.80	15.82	8.01	
$Ni_{50}Mn_{40}Sn_{10}$	49.37	40.31	9.92	8.16	
$Ni_{55}Mn_{20}Ga_{25}$	56.41	20.11	23.48	7.75	
$Ni_{50}Mn_{30}Ga_{20}$	49.97	30.35	19.68	7.71	
$Ni_{50}Mn_{25}Ga_{25}$	49.95	24.67	25.38	7.48	
$Ni_{45}Mn_{30}Ga_{25}$	45.32	30.33	24.35	7.38	
$Ni_{50}Mn_{20}Ga_{30}$	49.06	20.28	30.66	7.25	
$^{G}Ni_{45}Co_{5}Mn_{35}In_{15}$	45, 5	35	15	7.85	flipping ratio measurements
$Ni_{50}Mn_{33}In_{17}$	50.42	32.96	16.63	7.85	neutron diffraction
$^{A}Ni_{50}Mn_{35}In_{15}$	50.0	35.34	14.66	7.91	magnetocaloric effect measurements
$Ni_{52}Mn_{33}In_{15}$	51.36	32.87	15.77	7.91	
$^{A}Ni_{50}Mn_{35}Sn_{15}$	48.56	34.94	16.50	7.96	
$^{A}Ni_{50}Mn_{34}In_{15}Sn_{1}$	51.7	32.1	15.0 , 1.2	7.92	

Table 2.1: List of the samples used for the measurements in this thesis. Indices G, A denote samples prepared by group of Prof. Gutfleisch, and S. Aksoy, respectively.

3 Experimental methods

> Professor Bloch has told you how one can detect the precession of the magnetic nuclei in a drop of water. Commonplace as such experiments have become in our laboratories, I have not yet lost a feeling of wonder, and of delight, that this delicate motion should reside in all the ordinary things around us, revealing itself only to him who looks for it. I remember, in the winter of our first experiments, just seven years ago, looking on snow with new eyes. There the snow lay around my doorstep: great heaps of protons quietly precessing in the earth's magnetic field. To see the world for a moment as something rich and strange is the private reward of many a discovery. But I am afraid it has little bearing on the sober question we must, as physicists, ask ourselves: What can we learn from all this about the structure of matter?
>
> E.M.Purcell
>
> Nobel lecture (December 11, 1952)

3.1 Sample preparation

The studied samples were prepared by arc melting under argon atmosphere of elements of 99.999% purity. The total mass of the ingots prepared were about 3 g. The sample was remelted 7 times to ensure homogeneity. As-cast button-shaped ingots were ground on one side with 1500 grit polishing paper and then finished with Al_2O_3 powder. Afterwards, each sample was annealed for 48 h in a sealed quartz tube under argon atmosphere at 1073 K and then quenched in cold water. The compositions of the samples prepared were determined by energy dispersive X-ray analysis (EDX) in a scanning electron microscope (SEM). X-ray diffraction measurements were performed on the annealed and as-cast samples, followed by temperature-dependent magnetization measurements. The list of the samples, used in this work, is presented in table 2.1

3.2 Temperature-dependent magnetization measurements

We performed temperature-dependent magnetization measurements $M(T)$ on heating and cooling using a superconducting quantum interference device (SQUID) magnetometer to determine the Curie temperatures of the austenite, T_C^A, and the martensite, T_C^M, phases. In most cases the start temperatures of the structural transition to martensite, M_s, and austenite, A_s, could also be determined along with the width of the transitional hysteresis. $M(T)$ was measured under two constant magnetic fields, 5 mT and 5 T. Low-field data provides the information on behavior of the initial susceptibility of the material, while the high-field data gives information on the temperature dependence of the saturation magnetization. In the case of ferromagnetic Heusler alloys, the field-dependence of $M_s(H)$ can also be extracted from these measurements.

We performed temperature-dependent magnetization measurements using the following scheme:

1. The sample is warmed above the Curie temperature of the austenite phase T_C^A and zero-field-cooled (ZFC) to 5 K. It is worth noting, that remanent field of the SQUID magnetometer is about $\approx 0.5\ mT$, which can affect the initial behavior of the magnetization.
2. A magnetic field $H = H_0$ is applied, and $M(T)$ is measured on warming to 390 K (the highest temperature possible in SQUID).
3. $M(T)$ is measured on cooling from the highest temperature to 5 K under H_0. This measurement is called *field-cooled* (FC).
4. $M(T)$ is measured on rewarming to the highest temperature under H_0. This measurement is called *field-warming* (FW).

The FC and FW branches reveal the transitional hysteresis, and any difference between ZFC and FW branches can be the sign of the frustration of the magnetic moments in the system.

3.3 Powder X-ray diffraction

X-ray powder diffraction (XRD) method was used to determine crystallographic structure of the samples. Room temperature measurements were performed using PANAnalytical X'Pert X-ray diffractometer, and temperature-dependent measurements were made using a Phillips X-ray diffractometer. Both spectrometers incorporate a Cu anode ($K_{\alpha_1} = 1.5405\ \mathring{A}$, $K_{\alpha_2} = 1.5444\ \mathring{A}$). The X-ray spectra were refined using FullProf program suite [84].

3.4 Adiabatic calorimetry

We used a home-built adiabatic calorimeter for adiabatic temperature-change (ΔT_{ad}) measurements to study the MCE in ferromagnetic Ni-Mn-based Heusler alloys. In fig. 3.1 the principal layout of the cryostat with the adiabatic calorimeter insert is shown. The calorimeter is built as an insert into a continuous-flow liquid helium cryostat. A superconducting magnet is mounted inside the helium reservoir of the cryostat, allowing to change the magnetic field from $0\ T$ to $5\ T$ in the sample space. The temperature inside the cryostat is controlled by a heater/thermometer combination at the bottom of the sample space giving a continuous helium flow at constant temperature. The temperature can be stabilized in the temperature range between $5\ K$ and $350\ K$.

The adiabatic calorimeter consists of the following parts. The sample hangs on silk threads glued to a copper frame. Two steel cylinders shield the frame from thermal radiation. The space between the cylinders and the sample space can be independently filled with He exchange gas or evacuated using a turbo-molecular pump. The temperature in the sample space of the calorimeter can be set to a temperature $\pm 15\ K$ from the temperature of the cryostat. The temperature of the copper frame is controlled using a Lake Shore 430 temperature controller with PID regulation and in conjunction with a resistive heater and a GaAs diode thermometer. The temperature of the sample is measured with a chromel-constantan thermocouple

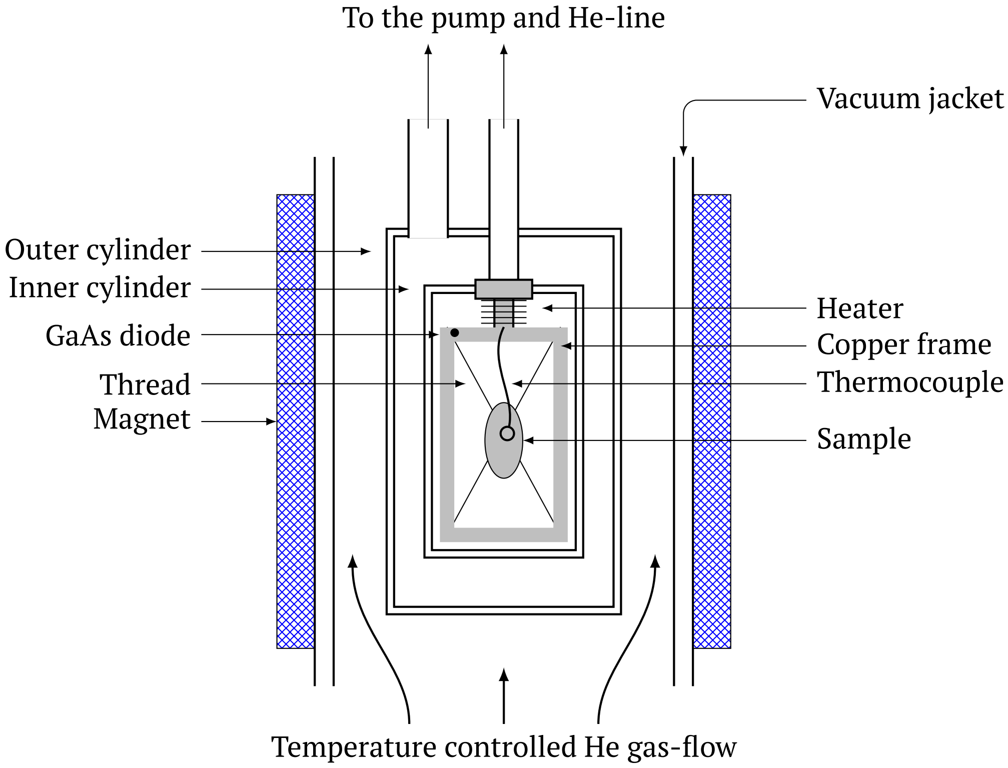

Figure 3.1: Principle layout of the adiabatic calorimeter setup, adopted from [15].

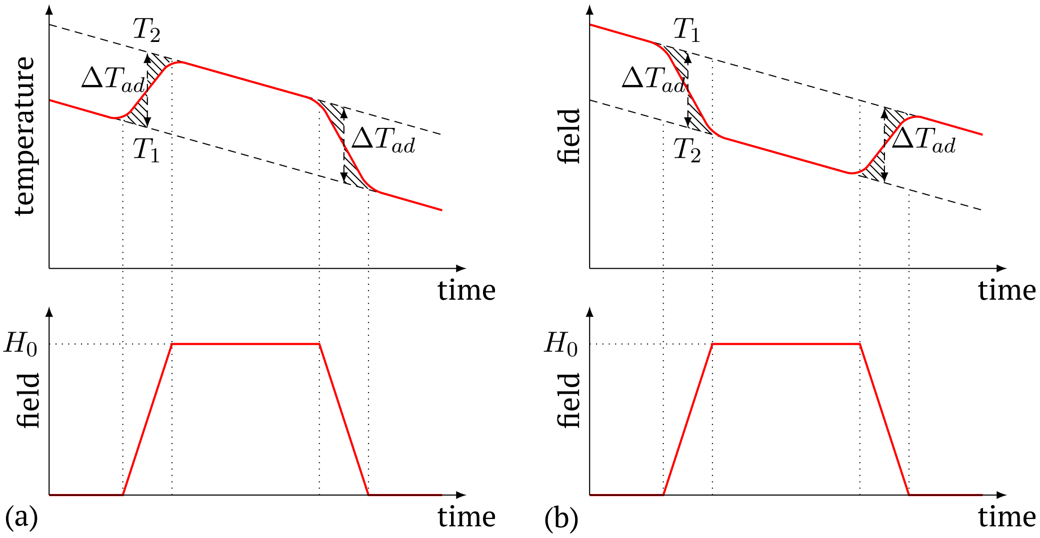

Figure 3.2: A sketch of ΔT_{ad} and magnetic field vs. experiment time for conventional (a) and inverse (b) magnetocaloric effects

embedded in the sample. Either a hole is drilled in the sample and the thermocouple is fixed into the hole, or the thermocouple is placed between two sliced halves of the sample.

In fig. 3.2, we show a sketch of ΔT_{ad} and magnetic field vs. experiment time. The lower figures show the time-profile of the field, and the upper figures show the time-profile of the sample-temperature for the cases of the conventional (a) and inverse (b) MCE.

We use the following protocol for the ΔT_{ad} measurements.

1. The desired temperature of the sample is stabilized. Usually the temperature

of the helium flow and the heater in the sample zone are set to be the same. Exchange gas is present between cylinders, and in the sample space.

2. The exchange gas is subsequently pumped out, and the sample temperature is monitored for about $600\ s$.
3. Magnetic field is applied. Field is $3\ T$ to $5\ T$ depending on the experiment and rises at a rate of 0.015 T/s
4. After the magnetic field reaches its maximum value, the field is held constant, and the temperature is monitored over another $600\ s$.
5. Magnetic field is set to zero at a rate of 0.015 T/s
6. After the magnetic field reaches zero, the temperature is monitored over another $600\ s$.
7. Another field-cycle can be started, or
8. exchange gas is introduced, and the system is stabilized at the next desired temperature.

The non-adiabatic behavior of the system is accounted for by the linear extrapolation of the data taken at $H = 0$ and $H = H_0$. ΔT_{ad} is estimated from the difference between T_2 and T_1, and the line between these points cuts equal shaded areas (see fig. 3.2).

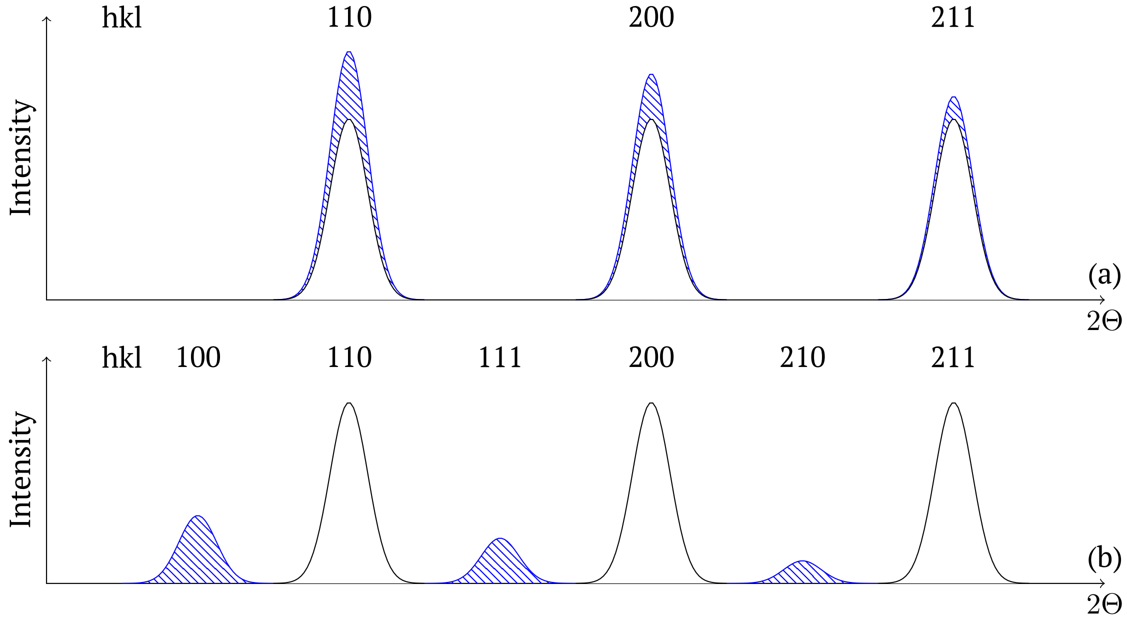

Figure 3.3: Schematic neutron diffraction patterns from a bcc polycrystalline (a) ferromagnet and (b) antiferromagnet. The shaded areas represent the magnetic scattering contributions which decrease with Θ because magnetic cross section f_{mag} decreases, taken from [85]

3.5 Neutron scattering techniques

A wide variety of techniques based on the scattering of certain beams of particles are currently used for probing atomic-scale structural and dynamic properties of materials. An "ideal" probe would be the one with variable wavelength, covering the scale from the spacings between the atoms to the short-range ordering in crystals and polymers. The particle wavelength should also be of order of an atom in the lattice to study its dynamics. It should have zero charge to avoid strong scattering with electrons and charged nuclei and should penetrate deeply in the material. A small magnetic moment is also desired so magnetic correlations and magnetic order/disorder can be studied. The neutron covers these specifications, and this is why neutron scattering is widely used as a powerful tool to understand material properties at the atomic scale.

In this work, we use elastic neutron scattering to determine the magnetic and the atomic structure under magnetic field in the temperature range $5 \leq T \leq 300$ K. The XYZ polarization analysis method was employed to investigate weak magnetic correlations in states with low net magnetization.

3.5.1 Elastic neutron scattering

Conventional X-rays and thermal neutrons are very similar in wavelength. 0.9-4.0 $\mathring{A}$ covers the emission spectra of most common anode materials (Cr, Fe, Co, Cu, Mo), but the scattering properties are quite different. X-rays scatter from electrons and yield information on electron densities in the crystal lattice, while neutrons scatter either from nuclei, or from the magnetic moments of unpaired electrons, probing the density distribution of nuclei or magnetic moments in the material (e.g. as shown on fig. 3.3. Thus X-ray diffraction and neutron scattering can be used as complementary methods for structural and magnetic analysis of the solid state.

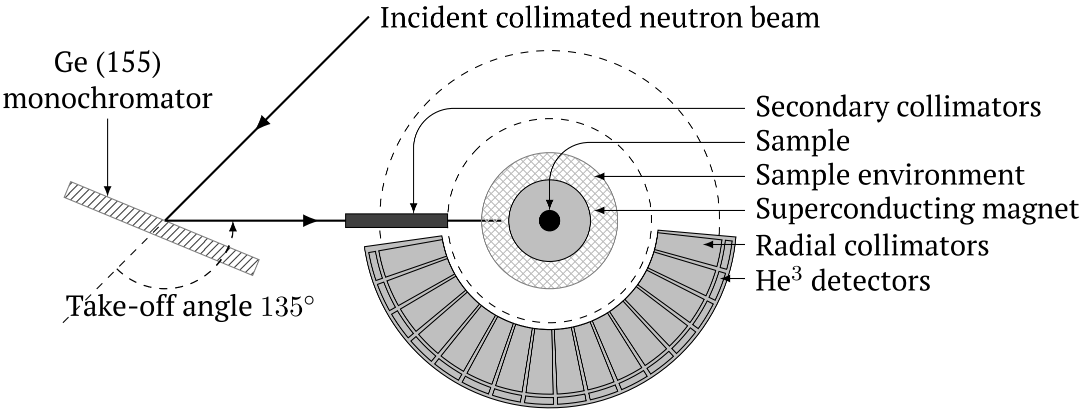

Figure 3.4: The layout of the D2B diffractometer at the ILL facility, Grenoble, France, adopted from [15].

For neutron diffraction experiments in this work, we have used the high-resolution D2B spectrometer at the Institut Laue Langevin (ILL), Grenoble, France [86] for elastic neutron scattering studies.

The layout of the spectrometer is shown in fig. 3.4. An incident polychromatic beam of the thermal neutrons is reflected from a germanium monochromator at a take-off angle of $135°$ and is diffracted. We use $\lambda_{incident} = 1.595\ \mathring{A}$ for our experiments. The focused beam passes through secondary collimators and scatters from the sample. The maximum beam size at the sample is $2 \times 5\ cm^2$. Bragg reflections from the sample are measured at the detector bank consisting of 128 ^3He detectors. The bank can be moved to cover the range $5° < 2\Theta < 165°$. A complete diffraction pattern is obtained after about 25 steps of $0.05°$ in 2Θ, as the detectors are spaced with $1.25°$ intervals. Time spent for each scan improves statistics.

The sample environment allows the temperature to be varied between $1.5\ K$ and $1000\ K$, and magnetic fields up to $5\ T$ can be applied.

3.5.2 Polarized neutron scattering

The fact that neutron is a fermion with spin $1/2$ is very important for neutron scattering studies. By interacting with the nuclear spin, it can give information on the nuclear spin structure, and by interacting with the spin resulting from unfilled electron shells of the atom it can give information on the magnetic moment of the atom. Both of these interactions are significantly weaker than Bragg scattering, but still can yield important information on spin correlations and magnetic ordering in materials.

We have also used the DNS spectrometer at the Forschungsreaktor München (FRM II), Garching, Germany [87] for the polarized neutron scattering studies. This diffuse, cold neutron scattering spectrometer is especially designed for the studies of elastic diffuse scattering of polarized neutrons and can probe different types of magnetic ordering in the sample. A diagram of the spectrometer is shown in fig. 3.5. The incident monochromatic unpolarized beam is polarized by a supermirror bender polarizer. It can then be flipped by a π-flipper, and subsequently scatters at the sample. The scattered beam is polarized again with supermirror analyzers each positioned in front of 24 ^3He detectors. The detector bank can be moved to cover the range $0° < 2\Theta < 150°$ and counts are averaged among the detectors, similar as in the D2B setup. In order to align the neutron polarization to an arbitrary direction at the sample position, XYZ-coils are used. Such a layout allows to separate

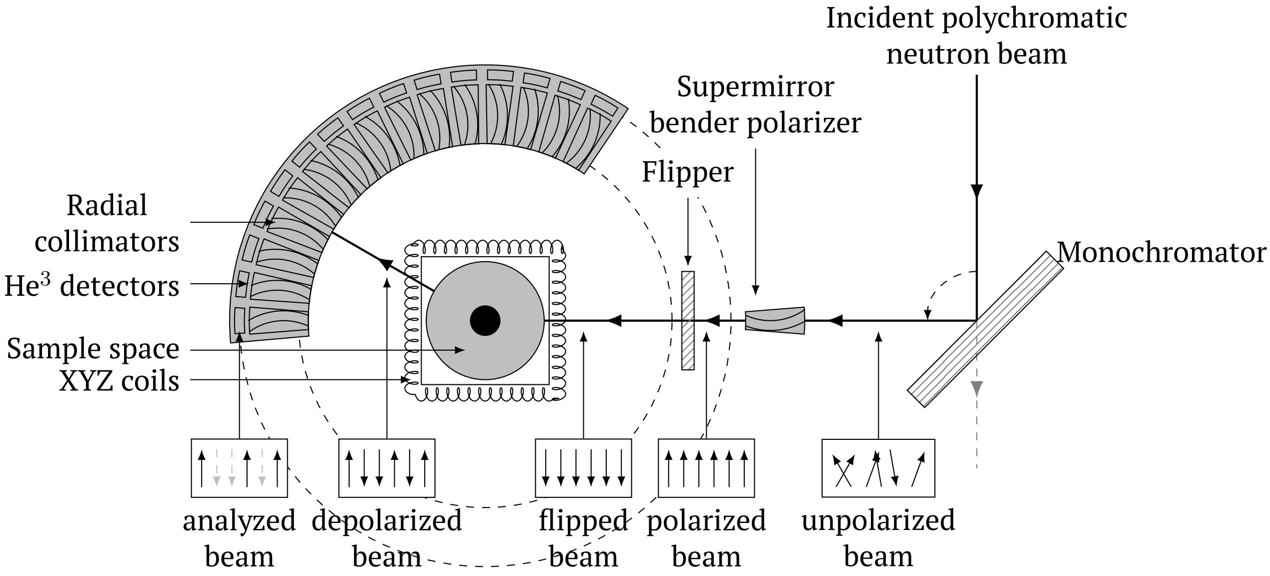

Figure 3.5: The layout of the DNS diffractometer at the FRM II facility, Garching, Germany, adopted from [15].

nuclear coherent (σ^{nuc}), spin-incoherent (σ^{inc}), and magnetic (σ^{m}) scattering cross sections from sole geometric considerations. `Nuclear coherent` (also reffered to as `spin-coherent`) scattering is an average, polarization-independent part of the neutron scattering on nuclei. `Nuclear incoherent` (`spin-incoherent`) scattering is the part of the neutron scattering arising from the random distribution of nuclear spins (if any), and the `magnetic` scattering is the scattering due to dipole-dipole interaction between a neutron and the magnetic field from the unpaired electrons. The sample environment allows to perform measurements in the temperature range $3.5 \leq T \leq 500$ K and in the fields up to $5\ T$.

The spectrometer is calibrated with the background measurement and measurement using vanadium and quartz samples. Neutron scattering from vanadium can be considered isotropic, as spin-incoherent nuclear cross section is much larger than spin-coherent one ($5.187\ barns$ vs. $0.0184\ barns$, respectively). Therefore, the absolute cross sections can be determined via a comparative scattering of from a vanadium sample. The analyzer efficiency is corrected using the nickel sample, as it gives only diffuse scattering having no nuclear spin.

In addition to the scattering cross sections, this spectrometer also allows measuring the flipping ratio. The flipping ration is a measure of the neutron beam depolarization defined as the ratio of spin-up and spin-down states of the neutron beam traversing the sample: $R_F = \frac{n\uparrow+1}{n\downarrow+1}$. $R_F = 1$ and $R_F \gg 1$ mean full depolarization of the beam and polarized beam, respectively. Due to technical reasons, the flipping ratio usually does not exceed value of 20 — 30 on the DNS spectrometer. When the polarized neutron beam traverses the sample with zero net magnetization, the flipping ratio remains constant. However, even small amount of randomly oriented ferromagnetic domains can significantly depolarize the beam resulting in a drop of R_F. This happens because, when the neutron encounters a domain, it begins to precess around the magnetization direction of the domain. Therefore, flipping ratio measurements can be a very sensitive tool for probing ferromagnetic domain formation. Flipping ratio measurement can be performed by using a detector with an analyzer positioned on the direct beam traversing the sample. If this is not possible due to the technical reasons (as in the DNS spectrometer), one can measure the ratio of spin-up and spin-down neutrons by positioning a detector on a structural reflection peak. In the current work, R_F is the ratio of spin up and spin down electrons measured with a detector positioned at $q = 2.05\ \mathring{A}^{-1}$ [1] , covering the whole (200) Bragg peak in the austenite phase and (202) in the martensite phase of our samples. In this work we used an incident neutron beam with wavelength $\lambda_{incident} = 4.2\ \mathring{A}$. A cryofurnace was used as a sample environment allowing to change sample's temperature between $3.5\ K$ and $500\ K$. Temperature dependent measurements of the flipping ratio and XYZ-neutron polarization analysis were performed for each sample.

XYZ polarization analysis

As mentioned above, it is possible to separate nuclear, spin-coherent and spin-incoherent contributions from the total scattering solely from geometric considerations. The conditions for the application of this method is that the sample should be isotropic, which is usually true for powder-samples, and that the net magnetization of the sample should be close to zero, so beam does not depolarize by magnetic domains. In this section, we will discuss the method and its application in selected prototype systems.

As it was shown by R.M. Moon et al. [88], one should perform two measurements with spin-flip (SF) and non-spin-flip (NSF) conditions with the beam-polarization along x, y and z axis. The *spin-flip* measurement is performed when supermirror polarizer and analyzer are antiparallel, and *non-spin-flip* is performed in a parallel orientation, respectively. XYZ-coils are three pairs of orhtogonal coils which are used to align neutron polarization in an arbitrary direction at the sample. Incident neutron beam is already polarized in z-direction and thus z-coil can be used to compensate the guide field in the sample area and turn it back, and x and y coils can adiabatically turn the polarization in x-y plane. Depending on the collocation of the extrenal field **H** (and thus neutron polarization vector **P**) and scattering vector **Q** different scattering conditions arise. In their work on triple-axis neutron spectrometer R.M. Moon et al. pointed out several general scattering conditions shown on table 3.1.

field/scattering vector	SF intensity	NSF intensity
$\mathbf{H} \parallel \mathbf{Q}$	$\sigma^{mag} + \frac{2}{3}\sigma^{inc} + \sigma^{bgr}$	$\sigma^{nuc} + 0\sigma^{mag} + \frac{1}{3}\sigma^{inc} + \sigma^{bgr}$
$\mathbf{H} \perp \mathbf{Q}$	$\frac{1}{2}\sigma^{mag} + \frac{2}{3}\sigma^{inc} + \sigma^{bgr}$	$\sigma^{nuc} + \frac{1}{2}\sigma^{mag} + \frac{1}{3}\sigma^{inc} + \sigma^{bgr}$

Table 3.1: Separation rules for scattering cross sections depending on collocation of the magnetic field and the scattering vector. By σ^{nuc}, σ^{mag}, σ^{inc}, σ^{bgr} we denote the nuclear coherent, magnetic, nuclear incoherent cross sections and the background intensity.

One can derive scattering cross section components for each experimental case using these rules. As an example let us consider the case where the neutron polarization vector **P** is parallel to the z-axis ($\mathbf{P} \parallel \hat{z}$), the scattering vector **Q** is parallel to the y-axis ($\mathbf{Q} \parallel \hat{y}$) and the total spin is characterized by its projections on the three axes: s_x, s_y, s_z (fig. 3.6) [15].

Spin-flip (SF) scattering occurs from the nuclear spin components perpendicular to **P** (σ_x^{inc} and σ_y^{inc}) and from the magnetization components perpendicular to

---

[1] Reciprocal units q[$\mathring{A}^{-1}$] are usually used to compare spectra obtained with different wavelengths as peak positions are preserved in this representation. $q = \frac{2 \cdot \sin\Theta}{\lambda_{incident}}$; where $\lambda_{incident}$ is incident wavelength, [$\mathring{A}$]; and Θ is half of the Bragg angle, 2Θ, used in X-Ray spectra. Peak positions in q-range correspond to interplanar distances d_{hkl}, so $q = \frac{1}{d_{hkl}}$.

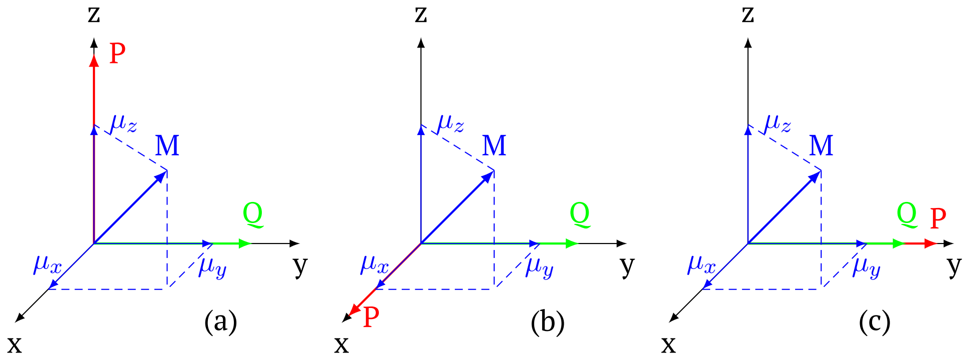

Figure 3.6: Scattering geometry of XYZ neutron polarization experiment with polarization vector **P** parallel to z-axis (a), x-axis (b), y-axis (c). The scattering vector is set to be parallel to y-axis. **M** denotes total spin of either nuclei or electron shell incident neutron scatters on. s_x, s_y, s_z are its components.

P (σ_x^{mag}). No SF scattering occurs along the y-direction because $\mathbf{Q} \parallel \mu_0\hat{y}$. Non-spin-flip (NSF) scattering is caused by the nuclear spin and magnetic components parallel to **P** (σ_x^{inc} and σ_x^{mag}):

$$\begin{array}{lll}
\mathbf{P} \parallel \hat{z} & \text{SF:} & \sigma_x^{mag}+\sigma_x^{inc}+\sigma_y^{inc}=\sigma^{mag}+2\sigma^{inc} \\
 & \text{NSF:} & \sigma_z^{mag}+\sigma_z^{inc}+\sigma^{nuc}=\sigma^{mag}+\sigma^{inc}+\sigma^{nuc} \\
\hline
\mathbf{P} \parallel \hat{x} & \text{SF:} & \sigma_z^{mag}+\sigma_x^{inc}+\sigma_y^{inc}=\sigma^{mag}+2\sigma^{inc} \\
 & \text{NSF:} & \sigma_z^{mag}+\sigma_z^{inc}+\sigma^{nuc}=\sigma^{mag}+\sigma^{inc}+\sigma^{nuc} \\
\hline
\mathbf{P} \parallel \hat{y} & \text{SF:} & \sigma_x^{mag}+\sigma_z^{mag}+\sigma_x^{inc}+\sigma_z^{inc}=2\sigma^{mag}+2\sigma^{inc} \\
 & \text{NSF:} & \sigma_y^{inc}+\sigma^{nuc}=\sigma^{inc}+\sigma^{nuc}
\end{array}$$

As a result of scattering cross sections separation one obtains the angular dependence $\frac{d\sigma}{d\Omega}(q)$ of each of the scattering cross section. While $\sigma^{nuc}(q)$ is similar to the conventional diffraction data, the q-dependence of the magnetic cross section $\sigma^{mag}(q)$ is of particular interest, as it is possible to obtain information on the magnetic ordering. As an example, we consider three basic cases of isotropic scattering, ferromagnetic correlations, and antiferromagnetic correlations.

In fig. 3.7(a), the magnetic cross section is plotted as a function of the wave vector q ($\lambda_{incident} = 4.8\ \mathring{A}$) in the *(001)* direction for $HoBa_2Cu_3O_7$ at $300\ K$. As it can be seen from the graph, this superconducting high-T_C cuprate shows isotropic scattering, in other words the magnetic cross section is constant over the q-range. [89].

In fig. 3.7(b), the effective paramagnetic moment $M(q)$ is plotted as function of the wave vector q for iron powder sample measured at two temperatures. α-Fe (bcc) iron orders ferromagnetically below $T_C = 1044\ K$, and at $T_{\alpha\rightarrow\gamma} = 1183\ K$ pure iron undergoes a structural transition between bcc α and fcc γ phases. Neutron polarization measurements were undertaken at $1120\ K$ in the α phase (open circles) and at $1320\ K$ in the γ phase (filled circles). Both spectra show considerable forward scattering below $1\ \mathring{A}^{-1}$. Note the different scales for $M(q)$ below and above $1\ \mathring{A}^{-1}$. The observed correlations are both strongly ferromagnetic [90].

In fig. 3.7(c) the effective paramagnetic moment $M(q)$ is plotted as function of the wave vector q in the (h00) direction for the single crystal chromium sample. Below Neel temperature $T_N = 311\ K$ chromium orders antiferromagnetically with a modulated sinusoidal structure. At T_N chromium undergoes first order antiferromagnetic-paramagnetic transition. Polarized neutron scattering measurements were performed at $367\ K$ ($1.18\ T_N$), $472\ K$ ($1.52\ T_N$) and $687\ K$ ($1.18\ T_N$). The only significant

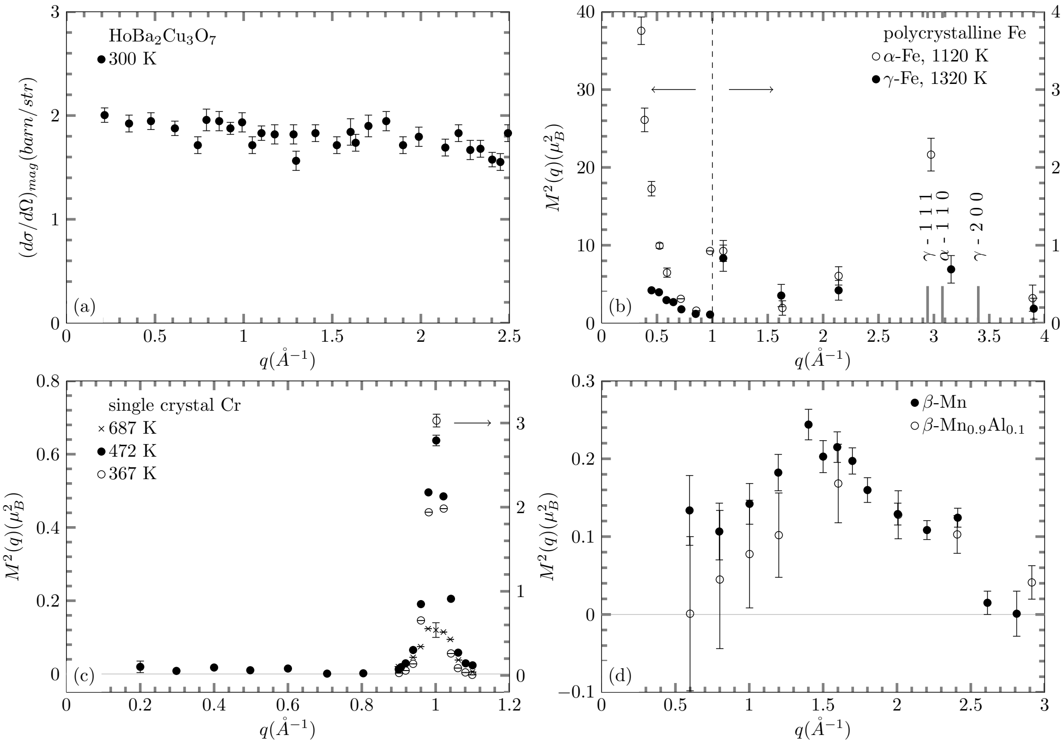

Figure 3.7: The q-dependence of the effective paramagnetic moments $M(q)$ in the case of:
(a) isotropic scattering in Rare-earth $HoBa_2Cu_3O_7$ at 300 K,
(b) forward scattering above Curie temperature in α and γ iron,
(c) itinerant antiferromagnetism in Cr,
(d) antiferromagnetic correlations in β-Mn and β-$Mn_{0.9}Al_{0.1}$,
adopted from [89], [90], [91] and [92], respectively.

paramagnetic scattering is observed around the *(100)* reflection, while the effective paramagnetic moment at lower q's is almost zero. These observations support the model of itinerant antiferromagnetism in chromium. [91]

In fig. 3.7(d), the effective paramagnetic moment $M(q)$ is plotted as a function of the wave vector q for β-Mn (filled circles) and β-$Mn_{0.9}Al_{0.1}$ (open circles) powder samples measured at $T = 290\ K$. β-Mn exhibits a nearly temperature-independent susceptibility $\chi(T)$, related to the absence of a local magnetic moment. Doping β-Mn with a small amount of Al leads to the formation of local moments in Mn and spin-glass behavior at the low temperatures. Polarized neutron scattering measurements were performed on these materials to clarify nature of magnetic interactions in these materials. Both samples show a large scattering peak at $1.5\ \AA^{-1}$ and $1.6\ \AA^{-1}$ for β-Mn and β-$Mn_{0.9}Al_{0.1}$, respectively. Such behavior is related to the presence of antiferromagnetic correlations as a result of frustration in the magnetic interactions, as in the case of β-Mn. Doping with Al releases the spin configuration degeneracy due to frustration and leads to spin-glass like state [92].

Although a powerful method, XYZ-polarization analysis has limitations. XYZ-polarization analysis inherently relies on low net magnetization of the sample (e.g. paramagnetic state) and thus on a high flipping ratio. In this case one can separate scattering terms, determine different scattering contributions and finally uncover the nature of the magnetic interactions in the sample.

However, this method is inapplicable in the ferromagnetically ordered state due to low R_F, and one should use complementary methods to probe the behavior of magnetic interactions on the whole temperature scale. For example, one could use Mössbauer spectroscopy or X-ray magnetic circular dichroism (XMCD) for these purposes. In this work, we used ferromagnetic resonance (FMR) to study the temperature behavior of the magnetism below magnetic order-disorder transition temperatures. An introduction to FMR measurement techniques will be given in the next section.

3.6 Ferromagnetic resonance on powder samples

The `ferromagnetic resonance` (FMR) is a powerful spectroscopic technique peeking into magnetic coupling, anisotropies and spin-lattice relaxation by measuring the precessional motion of magnetization in the sample. The idea of the FMR was first introduced by V.K. Arkad'yev in 1911 [93, 94]. The ferromagnetic resonance was experimentally discovered in 1946-1947 by J. Griffiths [95] and E.K. Zavoiskii [96] independetly. Extensive history of magnetic resonance development was recently reviewed by A.V. Kessenikh [97].

The FMR experiments are performed with a sample in a resonant microwave cavity fixed between the poles of electromagnet, reflected microwaves are detected by a detector diode behind the cavity. Microwave absorption intensity, proportional to this reflection, is measured while the external magnetic field is swept. Typical resonance curve and measured absorption are shown in fig. 3.8(a) and (b), respectively.

The simple model for precessing non-interacting spins (isotropic precessional case) leads to the resonance field $H_0 = \frac{\omega_0}{\gamma}$ (called isotropic value), where ω_0 is resonance frequency and γ is the gyromagnetic ratio, the characteristic of the total magnetic moment in the sample. Measured resonance field value (resonance line) equals isotropic one if the sample is in paramagnetic state. Magnetic anisotropy acts as an additional effective field changing the resonance field for a ferromagnet. Antiferromagnetic coupling between the magnetic moments in the lattice results in the resonance line lying usually far above isotropic value. Presence of crystallographic, magnetocrystalline, shape and stress anisotropies results in shift of resonance lines, as magnetic spins precess around combined anisotropy and external magnetic field. This also means that analysis of ferromagnetic resonance in polycrystalline or powder samples is difficult, as superposition of absorption peaks from various orientations result in broadening of the whole observed resonance line. However, if a few resonance lines are present in the signal, it is possible to determine resonance field for an anisotropy distribution present in powder.

From the gyromagnetic ratio γ one can determine material-dependent g-factor. For the electron it equals $g_e = -\frac{2m_e\gamma}{e} = -2.0023$. The g-factors of the pure metals are 2.09 (Fe), 2.25 (Co) and 2.21 (Ni), g-factor of some alloys: 2.12 ($FeNi$), 2.18 ($CoNi$), 2.01 (Cu_2MnAl Heusler alloy) [98]. The difference between g-factor of the electron g_e and one in metals is due to presence of the orbital moment and the contribution to the spin moment. Ratio of the orbital moment to the spin moment in 3d metals can be derived from the Kittel's formula [99, 100]: $\frac{g-2}{2} = \frac{\langle \mathbf{m_o} \rangle}{\langle \mathbf{m_s} \rangle}$. This shows that contribution of orbital moment $\mathbf{m_o}$ is small, less then 10%, although essential to magnetism, in particular magnetic anisotropy.

Also, comparison of g-factors derived from the ferromagnetic resonance (g_{res}) and gyromagnetic Einstein–de Haas and Barnett effects (g_{gyro}) can give additional valuable information on interactions between electrons in the materials [101, 102].

In our case, the FMR experiments were performed using the microwave frequency ($9.449\ GHz$, X-band). The external field up to $1.6\ T$ was applied in a sweep mode, with the modulation amplitude of $2\ mT$ and the modulation frequency $\omega_{mod} = 100\ KHz$. The measurement temperature was stabilized using helium-flow cryostat in the temperature range between $5\ K$ and $300\ K$, and using nitrogen-flow cryostat in temperature range from $200\ K$ to $450\ K$. Annealed powder samples (about $1\ mg$) were sealed off in suprasil tubes under vacuum (≈1 mbar) preventing atmospheric oxygen freezing in the sample space and oxidizing the samples. The ferromagnetic resonance spectra were recorded as the function of field and temperature.

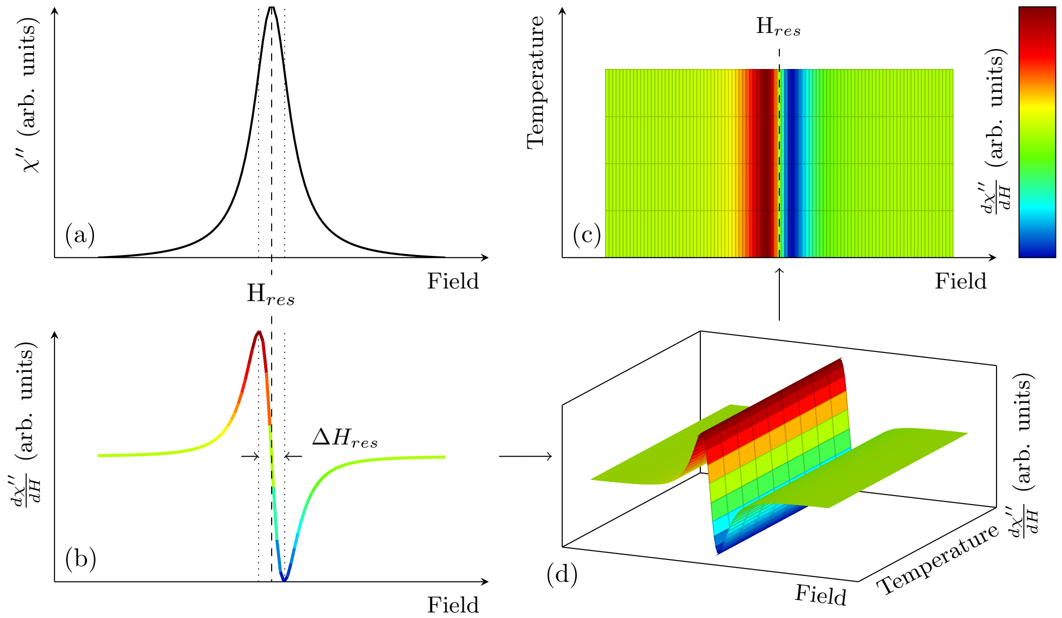

Figure 3.8: Field dependence of the transverse susceptibility $\chi''(H)$ in the vicinity of the resonance field (a), obtained by the integration of the measured signal $\frac{d\chi''}{dH}(H)$ (b). Temperature dependence of the measured absorption signal $\frac{d\chi''}{dH}(H,T)$ can be visualized either as a 3D plot (c), or as a colormap plot (d), using color as a measured signal intensity coordinate. Rapid change of color in the middle of the plot corresponds to the resonance field H_{res}.

3.6.1 FMR data representation

The field dependence of the imaginary part of the transverse susceptibility $\chi''(H)$ in the vicinity of the resonance field shows a resonance behaviour. We show a sketch of such dependence in the vicinity of the resonance field in fig. 3.8(a). The resonance field H_{res}, corresponds to the maximum point on the graph and marked by a dashed line. The width of the resonance at half of the maximum (FWHM) is marked by dotted line.

The FMR signal, measured in the experiment, is the microwave absorption, its derivation with resprect to the field is proportional to the first derivative of the transverse susceptibility with respect to the external field, $\frac{d\chi''}{dH}(H)$. We show the field dependence of the measured signal $\frac{d\chi''}{dH}(H)$ on fig. 3.8(b). The intensity of the signal, plotted with ordinate is additionally colorcoded, so the maximum is colored with red, minimum with blue and "zero-level" is green. As the measured signal is the first derivative of the transverse susceptibility, the resonance field H_{res} position coincides with the point were measured signal graph changes its sign, and resonance width can be calculated as the distance between local extrema.

The result of the series of the measurements is a temperature dependence of absorption signal $\frac{d\chi''}{dH}(H,T)$. The resulting plot is built up as a stack of consequent field-dependent FMR spectra temperature ordered by measurement temperature, and each spectrum is plotted with finite step in temperature range with linearly interpolated points between the experimental data. On fig. 3.8(d) we show temperature dependence of the measured signal, which is represented as a a 3D-plot. Again, as on the previous plot, the intensity coordinate is colorcoded in the same way. While such plot is quite depictive, if several resonance lines are present in the measured signal, such representation becomes difficult to read.

One possible way to simplify the data representation is to plot the data as 2D colormap, keeping the field and temperature coordinates and plotting the signal intensity in color.

We show the example of such plot on fig. 3.8(c). Intensity of the measured signal is represented with the color bar, so positive intensities are associated with colors from green to red, and negative ones with colors from green to blue. And the absolute maximum and minimum of the whole graph are associated with red and blue, respectively. So the temperature behavior of the signal intensity and width is seen from the colorgraph. However, if the magnitude of the FMR signal significantly (e.g. by the order of magnitude) changes with temperature then resolution of the colormap graph is not enough and the temperature region with low signal would not reveal a contrast of colors.

The other possible way is to normalize intensity of each spectrum to the unit segment $[0, 1]$. In this case the resolution of the graph is higher and the temperature behaviour of the resonance line positions is more clear. However, the information on intensity behavior is lost in this case.

In both cases the resonance field can be seen as an abrupt change of the color (e.g. from red to blue) on the abscissae-axis (field dependence). Comparing the position of the resonance line with reference line $\omega/\gamma = \frac{2\pi\cdot 9.449*10^9[Hz]}{1761*10^{11}[rads^{-1}T^{-1}]} = 337\,mT$ (what corresponds to $g_{res} = 2$), one can get an understanding of the temperature behavior of the magnetic interactions in the system.

4 Results on Ni-Mn-based martensitic Heusler alloys

4.1 Temperature dependence of the magnetization of Ni-Mn-based Heusler alloys

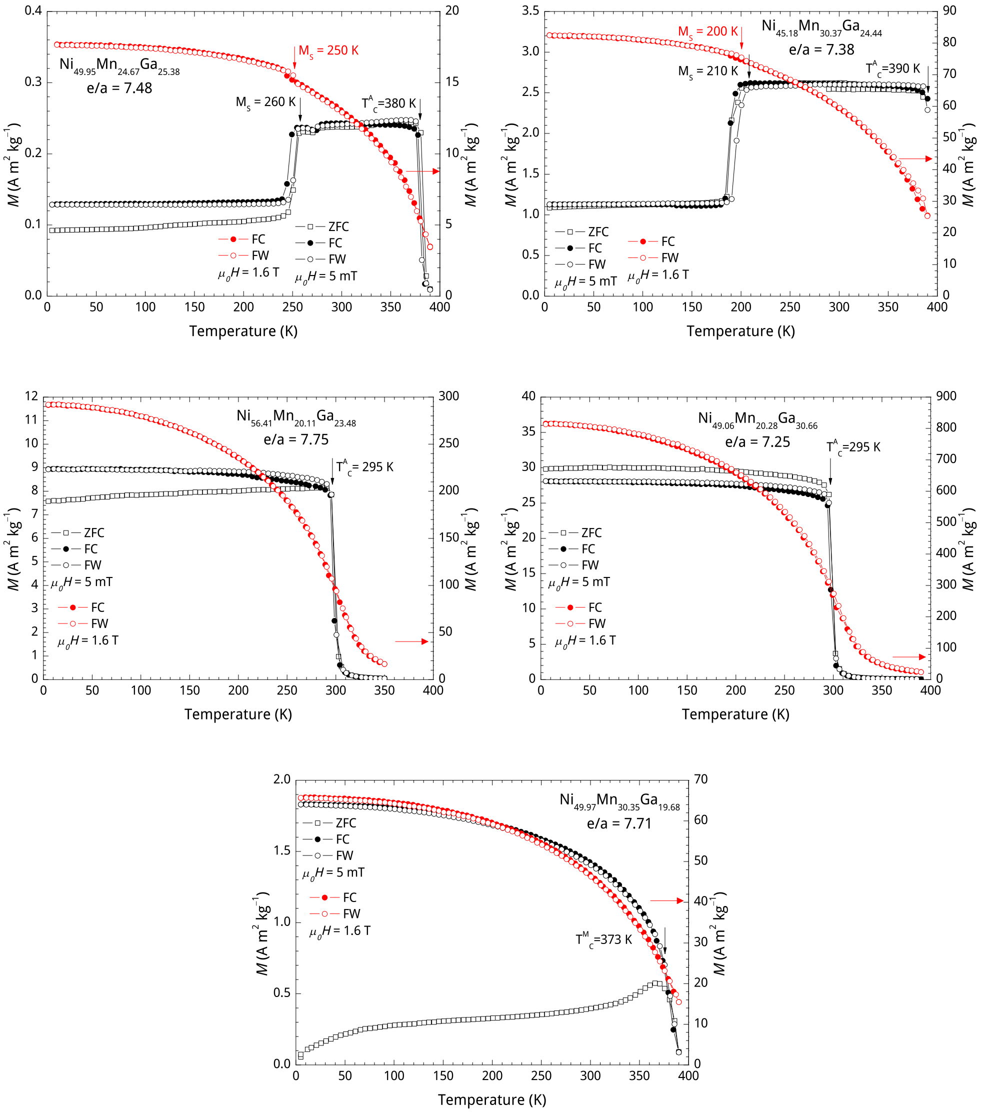

Figure 4.1: Temperature dependence of magnetization measured in 5 mT (black color) and 1.6 T (red color) under ZFC (open squares), FC (filled circles) and FW (open circles) protocols of the following $Ni-Mn-Ga$ based samples: $Ni_{49.95}Mn_{24.67}Ga_{25.38}$ (a), $Ni_{45.18}Mn_{30.37}Ga_{24.44}$ (b), $Ni_{56.41}Mn_{20.11}Ga_{23.48}$ (c), $Ni_{49.06}Mn_{20.28}Ga_{30.66}$ (d), $Ni_{49.97}Mn_{30.35}Ga_{19.68}$ (e).

Ni-Mn-Ga series

In fig. 4.1 we show the temperature dependence of the magnetization for various $Ni - Mn - Ga$ based samples with Mn-rich and Mn-deficient compositions.

The first sample to be discussed is the $Ni_{49.95}Mn_{24.67}Ga_{25.38}$ sample with the composition close to stoichiometry with valence electron concentration $e/a = 7.48$. Temperature dependence of the magnetization $M(T)$ measured under ZFC, FC and FW protocols in 5 mT and 1.6 T magnetic field is shown in fig. 4.1 (a).

This sample undergoes magnetic order-disorder transformation in the austenite state at $T_C^A = 380\ K$ seen as an abrupt non-hysteretic change of the magnetization. On further cooling, $M(T)$ slightly decreases and exhibits small kink at $270\ K$ related to premartensite building, and then it abruptly drops as sample starts transforming into martensite at $M_s = 260$ K and remains almost constant down to $5\ K$. Considerable difference between ZFC and FW branches is related to magnetic anisotropy. Temperature dependence of the magnetization measured in $1.6\ T$ field shows that the saturation magnetization in the martensite phase is higher than in the austenite phase; and that martensite start temperature shifts to lower temperatures by $\approx 10\ K$ $(-6.25K/T)$.

Figure 4.1 (b) shows temperature dependence of the magnetization for Ni-deficient $Ni_{45.18}Mn_{30.37}Ga_{24.44}$ sample. In this sample $5\ at.\%$ of Ni are substituted by Mn, so it partly occupies Ni sublattice. Thus valence electron concentration is lowered to $e/a = 7.38$. The temperature behavior of the magnetization is similar to the stoichiometric sample. In 5 mT field, this sample undergoes FM-PM transition in the austenite state at $T_C^A = 390\ K$, and structural transition at $M_s = 210\ K$. However magnetic anisotropy is lower in this sample as FW and ZFC curves almost retrace each other. Magnetization of the low-temperature phase in $1.6\ T$ magnetic field is higher than high-temperature one, and structural transition temperature shifts towards low temperatures ($M_s = 200\ K$, $-6.25K/T$).

Figure 4.1 (c) shows temperature dependence of the magnetization for the Ni-rich $Ni_{56.41}Mn_{20.11}Ga_{23.48}$ sample. In this sample, $5\ at.\%$ of Mn are substituted by Ni, occupying Mn sublattice. Thus valence electron concentration is raised to $e/a = 7.75$. The sample undergoes FM-PM transition in the austenite state at $T_C^A = 295\ K$ and then $M(T)$ slightly rises towards lower temperatures as in a typical ferromagnet. However, in contrast to $M(T)$ of a pure FM alloy, in this case ZFC curve splits with the FC and FW curves, suggesting the presence of non-FM entities in the sample. Compared to the previous sample no structural transition is detected in the magnetically ordered state. Both FC and FW curves in $1.6\ T$ field feature smeared-out magnetic order-disorder transition and no magnetic thermal hysteresis is observed.

Next sample to be discussed is Mn-deficient ($e/a = 7.25$) $Ni_{49.06}Mn_{20.28}Ga_{30.66}$ sample, where $5\ at.\%$ of Mn are substituted by Ga, thus diluting Mn in its sublattice. Temperature dependence of the magnetization shown in fig. 4.1 (d) exhibits similar behavior of the magnetization as the previous sample. No sign of the thermal hysteresis is observed below Curie temperature $T_C^A = 295\ K$. Below T_C^A ZFC curve in 5 mT lies higher than FC and FW curves (which retrace each other). As in the previous sample FC and FW curves retrace each other in $1.6\ T$ field.

The last sample to be discussed in Ni-Mn-Ga series is Mn-rich ($e/a = 7.71$) $Ni_{49.97}Mn_{30.35}Ga_{19.68}$ sample. In contrast to the previous sample here Mn atoms substitute Ga atoms in the lattice by $5\ at.\%$. $M(T)$ under different conditions in 5 mT and 1.6 T fields is shown in fig. 4.1 (e). In the plotted region the sample does not undergo any transitional hysteresis as no hysteresis in FC and FW curves is observed. However, slow declination of magnetization with temperature can be attributed to magnetic order-disorder transition in the martensitic state at $T_C^M = 373\ K$, while the structural transition temperature lies at higher temperatures in the PM state (e.g compare with $M(T)$ of $Ni_{50}Mn_{36}Sb_{14}$ fig. 2.10(d)). Thus, the behavior of the ZFC curve in $5\ mT$ field can be explained as a reduction of magnetic anisotropy with the temperature. FC and FW magnetization curves measured in $1.6\ T$ retrace each other and exhibit magnetic order-disorder transition.

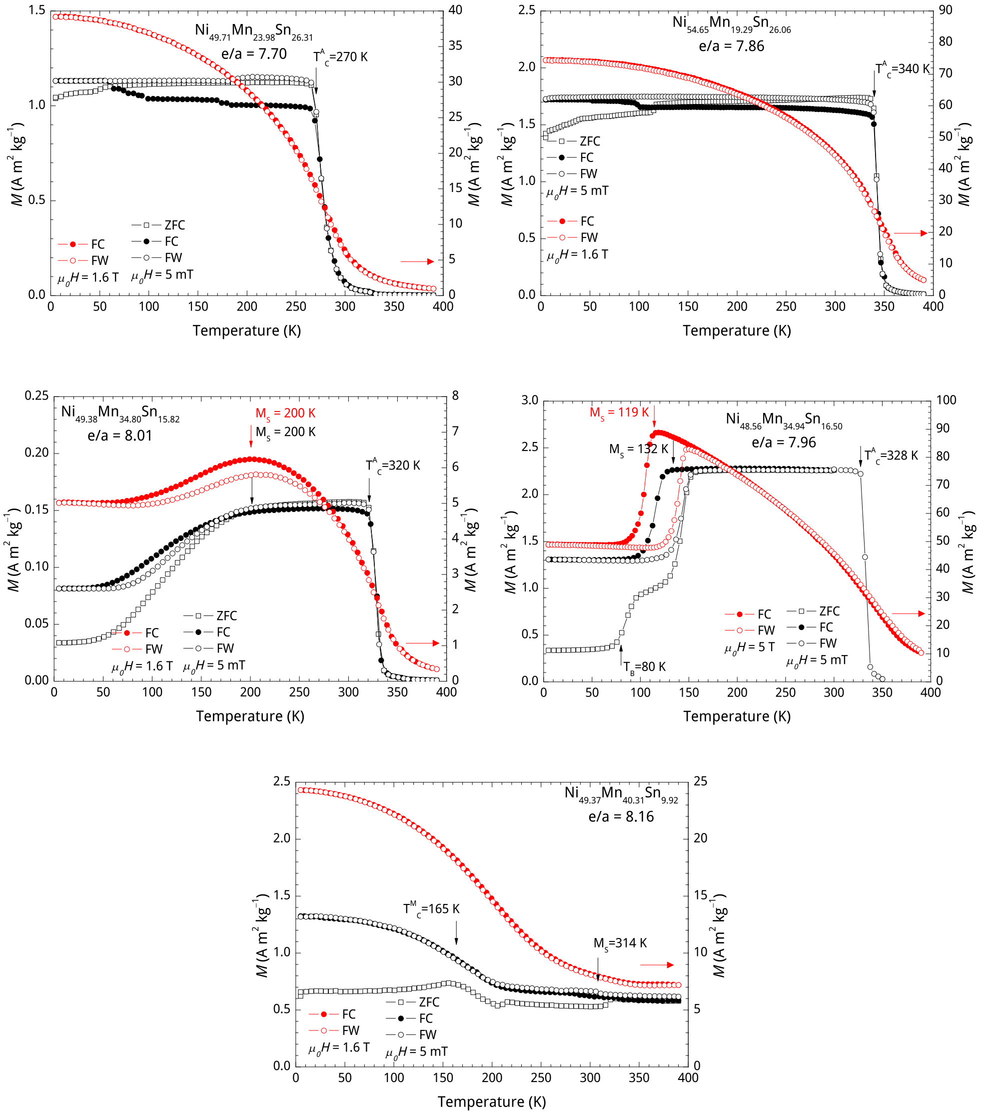

Figure 4.2: Temperature dependence of magnetization measured in $5\ mT$ (black color) and $1.6\ T$ (red color) under ZFC (open squares), FC (filled circles) and FW (open circles) protocols of the following $Ni - Mn - Sn$ based samples: $Ni_{49.17}Mn_{23.98}Sn_{26.31}$ (a), $Ni_{54.65}Mn_{19.29}Sn_{26.06}$ (b), $Ni_{49.38}Mn_{34.80}Sn_{15.82}$ (c), $Ni_{48.56}Mn_{34.94}Sn_{16.50}$ (d), $Ni_{49.37}Mn_{40.31}Sn_{9.92}$ (e).

Ni-Mn-Sn series

In fig. 4.2 we show temperature dependencies of the magnetization $M(T)$ of various $Ni - Mn - Sn$ based samples with Mn-rich and Mn-deficient compositions.

Figure 4.2 (a) shows temperature dependence of the magnetization $M(T)$ of the

$Ni_{49.17}Mn_{23.98}Sn_{26.31}$ sample ($e/a = 7.70$). This sample is close to stoichiometric Ni_2MnSn composition, however its Mn and Ni concentration is lower. This sample undergoes FM-PM transition in the austenitic state at $T_C^A = 270\ K$. No sign of transitional thermal hysteresis is observed, so the sample does not transform. FC and FW curves measured in $1.6\ T$ retrace each other, showing only smeared out PM-FM transition.

Figure 4.2 (b) shows Ni-rich, Mn-deficient $Ni_{54.65}Mn_{19.29}Sn_{26.06}$ sample ($e/a = 7.86$). Its behavior is much similar to the previous case of the close-to-stoichiometry $Ni_{49.17}Mn_{23.98}Sn_{26.31}$ sample: it undergoes magnetic ordered-disordered transition in the austenite phase at $T_C^A = 328\ K$, while no transitional hysteresis is observed.

Figure 4.2 (c) shows temperature dependence of the magnetization of Mn-rich $Ni_{49.38}Mn_{34.80}Sn_{15.82}$ sample ($e/a = 8.01$). The sample orders ferromagnetically in the austenite state below $T_C^A = 320\ K$, then $M(T)$ initially remains almost constant, and then starts decreasing as the sample transforms into the martensite around down to structural transition temperature $M_s = 200\ K$. As martensite concentration rises, magnetization goes down, and then remains constant as transition finishes. It is difficult to determine characteristic temperatures of the structural transition solely from the 1.6 T data.

Figure 4.2 (d) shows temperature dependence of the magnetization of the Mn-rich $Ni_{48.56}Mn_{34.94}Sn_{16.50}$ sample ($e/a = 7.96$). This sample undergoes transition between FM and PM states in the austenite phase at $T_C^A = 328\ K$. On further cooling $M(T)$ remains constant until the start of martensitic transition at $M_s = 132\ K$. On further cooling below martensitic transition finish temperature, $M(T)$ remains constant until $5\ K$. On heating from ZFC state, magnetization remains constant until temperature $T_B = 80\ K$, and then abruptly rises. This feature is exhibited only on the ZFC curve, thus it is related to the decay of blocking around this temperature. Second abrupt rise of the magnetization is related to building of the austenitic phase. 1.6 T temperature dependence of the magnetization features martensitic transition shifted to the lower temperatures by $\approx 13\ K$ ($\approx 2.6K/T$).

The last sample to be discussed in Ni-Mn-Sn series is the Mn-rich $Ni_{49.37}Mn_{40.31}Sn_{9.92}$ ($e/a = 8.16$) sample. The temperature dependence of the magnetization of this sample is shown in fig. 4.2 (e). In temperature range between $5\ K$ and $400\ K$ it exhibits smeared out magnetic order disorder transition in martensitic state around $T_C^M \approx 165\ K$. As FC and FW curves retrace each other in this temperature range, we conclude that no structural transition is detected. However it is possible that it lies at higher temperatures in PM state (e.g compare with $M(T)$ of $Ni_{50}Mn_{37}Sn_{13}$ fig. 2.10(c), where A_s lies in PM state). Both FC and FW curves measured in $1.6\ T$ show smeared out magnetic transition in martensitic state.

Ni-Mn-In series

In fig. 4.3 we show temperature dependencies of the magnetization of various $Ni-Mn-In$ samples and $Ni-Mn-In$ doped with Sn and Co samples.

Figure 4.3 (a) shows $M(T)$ for $Ni_{50.00}Mn_{35.34}In_{14.66}$ sample ($e/a = 7.91$) under field of 5 mT and 5 T. The sample resides in paramagnetic austenite state above $T_C^A = 312\ K$ and below this temperature it orders ferromagnetically. On further cooling, magnetization passes its maximum and rapidly decreases starting at $M_s = 300\ K$ as sample transforms into martensite. As austenite-to-martensite ratio $\frac{a}{m}$ decreases the total magnetization of the sample goes down and reaches its minimum around $M_f \approx 250\ K$. Between M_f and $T_C^M = 180\ K$ sample resides in PM-like state and becomes ferromagnetic again below Curie temperature of the martensite. Below this temperature large separation between ZFC and FC/FW curves is observed. This is related to magnetic anisotropy in the martensitic state: magnetic domain configuration depends on external field on cooling below T_C^M. Temperature dependence of the magnetization measured at $5\,T$ shows that martensitic transformation shifts towards lower temperatures by $15\ K$ ($\approx 3\ K/T$).

Figure 4.3 (b) shows $M(T)$ for $Ni_{51.36}Mn_{32.87}In_{15.77}$ sample with the same valence electron concentration $e/a = 7.91$. However, in this sample Ni and In concentrations are higher, and Mn concentration is lower. The sample undergoes PM-FM transition in austenite state at $T_C^A = 288\ K$, then on further cooling it starts transforming into the martensite at $M_s = 260\ K$. As concentration of the non-ferromagnetic martensite increases its magnetization decreases, passing its minimum at 235 K, and then the sample undergoes magnetic transition in marten-

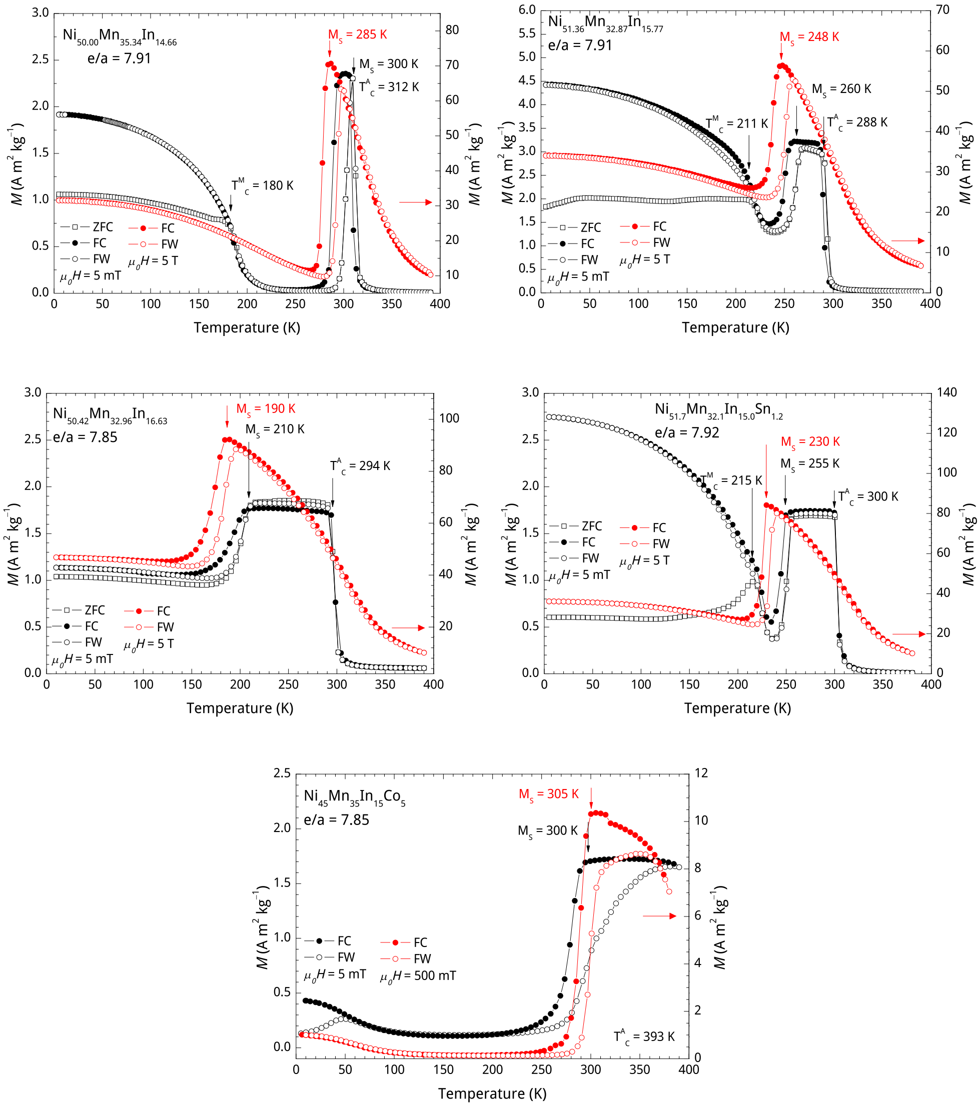

Figure 4.3: Temperature dependence of magnetization measured in $5\ mT$ (black color) and $5\ T$ (red color) under ZFC (open squares), FC (filled circles) and FW (open circles) protocols of the following samples: $Ni_{50.00}Mn_{35.34}In_{14.66}$ (a), $Ni_{51.36}Mn_{32.87}In_{15.77}$ (b), $Ni_{50.42}Mn_{32.96}In_{16.63}$ (c), $Ni_{51.7}Mn_{32.1}In_{15.0}Sn_{1.2}$ (d), $Ni_{45}Co_5Mn_{35}In_{15}$ (e).

sitic state at $T_C^M = 211\ K$. In this sample low magnetization region in martensitic state is significantly reduced compared to that of the $Ni_{50.00}Mn_{35.34}In_{14.66}$ sample. Temperature dependence of the magnetization measured in $5\ T$ field shows that the structural transition temperature M_s is shifted towards lower temperatures by $12\ K$ ($\approx 2.4\ K/T$).

Figure 4.3 (c) shows $M(T)$ for $Ni_{50.42}Mn_{32.96}In_{16.63}$ sample with lower valence electron concentration than in previous cases ($e/a = 7.85$). This sample orders ferromagnetically in the austenitic state below $T_C^A = 294\ K$. On further cooling $M(T)$ remains almost constant until the sample starts transforming into the martensite below $M_s = 210\ K$. In contrast to the previous cases the drop of the magnetization in the end of the structural transition is much lower and sample does not exhibit magnetic transition in the martensitic state (alternatively it could be above M_s, e.g. compare with $M(T)$ of $Ni_{50}Mn_{27}Sn_{23}$ fig. 2.10(a)). Comparison of the FC curves measured in $5\ mT$ and $5\ T$ gives the shift of the transformation temperature of $\approx 4\ K/T$.

Next is the case of the $Ni_{51.7}Mn_{32.1}In_{15.0}Sn_{1.2}$ sample, its temperature dependence of the magnetization is shown in fig. 4.3 (d). This sample has Ni, Mn and In concentrations close to the $Ni_{51.36}Mn_{32.87}In_{15.77}$ sample (see fig. 4.3 (b)), but additionally it is doped with Sn, so the valence electron concentration is slightly higher ($e/a = 7.92$ vs. 7.91). However its temperature dependence of the magnetization is similar to the $Ni_{51.36}Mn_{32.87}In_{15.77}$ sample. It orders ferromagnetically below $T_C^A = 300\ K$, starts transforming into the martensite at $M_s = 255\ K$, and the orders ferromagnetically again in the martensitic state at $T_C^M = 215\ K$. $5\ T$ field magnetization measurements show that shift of the transformation temperature is $\approx 3\ K/T$.

The last case to be discussed is $Ni_{45}Co_5Mn_{35}In_{15}$ ($e/a = 7.85$), shown in fig. 4.3 (e). In this sample Ni was substituted by 5% at. of Co, so Co occupied Ni sublattice. This sample undergoes FM-PM transition in the austenitic state at $T_C^A = 393\ K$. On cooling it starts transforming into martensite at $M_s = 300\ K$. With growth of the non-ferromagnetic martensitic phase magnetization drops significantly almost to zero. Unlike the other $Ni - Mn - In$ based samples the low magnetization region continues down to $50\ K$, where magnetization starts rising again. The difference between FC and FW curves are similar to the spin-glass behavior and suggests the presence of the frozen state at lower temperatures.

Composition	T_C^M, (K)	$M_s, (K)$	$T_C^A, (K)$	$M_s fieldshift, (T/H)$	e/a
$Ni_{54.65}Mn_{19.29}Sn_{26.06}$	-	-	340	-	7.86
$Ni_{49.71}Mn_{23.98}Sn_{26.31}$	-	-	270	-	7.70
$Ni_{49.38}Mn_{34.80}Sn_{15.82}$	-	200	320	?	8.01
$Ni_{48.56}Mn_{34.94}Sn_{16.50}$	-	132	328	2.6	7.96
$Ni_{49.37}Mn_{40.31}Sn_{9.92}$	165	?	-	?	8.16
$Ni_{56.41}Mn_{20.11}Ga_{23.48}$	-	-	295	-	7.75
$Ni_{49.97}Mn_{30.35}Ga_{19.68}$	373	?	?	?	7.71
$Ni_{49.95}Mn_{24.67}Ga_{25.38}$	?	260	380	6.25	7.48
$Ni_{45.32}Mn_{30.33}Ga_{24.35}$	?	210	390	-6.25	7.38
$Ni_{49.06}Mn_{20.28}Ga_{30.66}$	-	-	295	-	7.25
$Ni_{45}Co_{5}Mn_{35}In_{15}$	50	300	393	1	7.85
$Ni_{50.42}Mn_{32.96}In_{16.63}$	?	210	294	4	7.85
$Ni_{50.00}Mn_{35.34}In_{14.66}$	180	300	312	3	7.91
$Ni_{51.36}Mn_{32.87}In_{15.77}$	211	260	288	2.4	7.91
$Ni_{51.7}Mn_{32.1}In_{15}Sn_{1.2}$	215	255	300	5	7.92

Table 4.1: List of the samples with determined characteristic transition temperatures.

4.2 Field-cycling dependence of the adiabatic temperature change

4.2.1 $Ni_{50}Mn_{35}Sn_{15}$

The temperature dependence of the adiabatic temperature change ΔT_{ad} for the $Ni_{48.6}Mn_{34.9}Sn_{16.5}$ sample is shown in fig. 4.4(a), the temperature dependence of the magnetization in $5\ mT$ and $5\ T$ measured in the same temperature region is shown in fig. 4.4(b).

The sample was cooled in zero-field to $T_i = 100\ K$ prior to the warming to the measurement temperature. The conventional MCE is observed below $A_s = 125\ K$ on both applying and removing the $5\ T$ field. As the system resides on the reverse transformation branch above this temperatures, the inverse MCE is observed on the application of the field. However, the removing of the field gives the rise to further cooling, thus the conventional MCE is observed. Above the austenite finish temperature $A_f \approx 160\ K$ the conventional MCE is observed with higher magnitude than in the martensite state. The maximum inverse adiabatic temperature change of $-2.5\ K$ is observed at $150\ K$. We also performed measurements on the forward transformation branch shown by open triangles in fig. 4.4(a). In this case the system was cooled from $T_i = 180\ K$ in the austenitic state. Both measurements at $142\ K$ and $155\ K$ showed the conventional MCE on the applying and removing of the magnetic field.

In fig. 4.5 we show the field-cycling dependence of the adiabatic temperature change measured in $5\ T$. Prior to the measurement system was cooled down to $T_i = 100\ K$ in zero-field, and then heated up to $151\ K$ in zero field so it resides on the reverse transformation branch in a mixed state. Initial application of the $5\ T$ field at point ① results in the adiabatic cooling with $\Delta T_{ad} = -2.5\ K$ (inverse MCE), consequent removing of the field at point ② further cools the system by $\Delta T_{ad} = -0.4\ K$ (conventional MCE). The system always exhibits the conventional MCE with the constant magnitude $|\Delta T_{ad}| = 0.4\ K$ on further cycles, when field is applied (point ③) and removed (point ④).

4.2.2 $Ni_{50}Mn_{35}In_{15}$ and $Ni_{52}Mn_{33}In_{15}$

The temperature dependence of the adiabatic temperature change ΔT_{ad} for the $Ni_{50.0}Mn_{35_3}In_{14.7}$ sample is shown in fig. 4.6(a). Prior to each measurement the sample was cooled down to $T_i = 180\ K$ in zero field to ensure that it is fully martensitic. Afterwards it was heated up in the zero-field to the measurement temperature, where the $5\ T$ field was adiabatically applied and removed. The sample exhibits a small conventional MCE below the austenite start temperature $A_s = 288\ K$. In the temperature range between $A_s < T < A_f$ the sample resides on the reverse transformation branch of the martensitic transition and exhibits the inverse MCE. In this region the adiabatic temperature change ΔT_{ad} on applying the field is always larger then on removing the field. This irreversibility happens due to transformational hysteresis losses. The maximum effect of $2\ K$ is observed, when the system resides close to the inflection point of the reverse transformation branch of the magnetization thermal hysteresis ($\approx 290\ K$, see fig. 4.6(b)).

Figure 4.6(c) shows the temperature dependence of the adiabatic temperature change ΔT_{ad} of the $Ni_{51.3}Mn_{32.9}In_{15.8}$ sample. Prior to each measurement the sample was brought to the martensitic state at $T_i = 200\ K$ and then heated up in zero field to the measurement temperature. Below $A_s \approx 229\ K$ the system shows the conventional MCE ($0.1\ K/T$), while in the martensitic transformation region

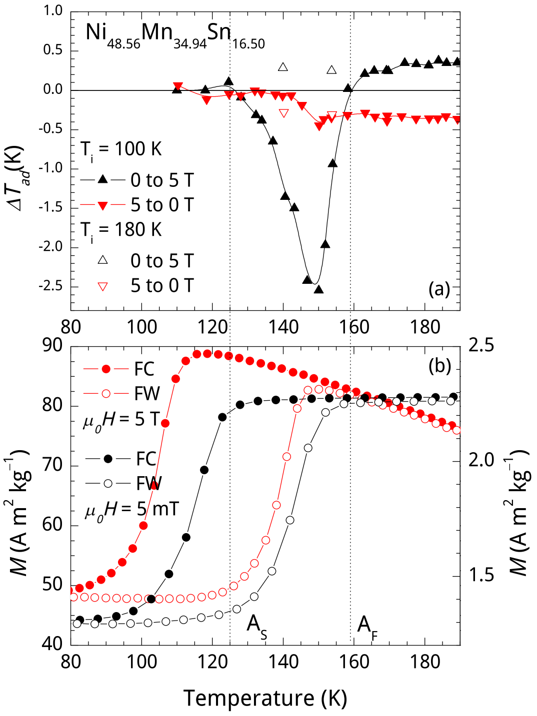

Figure 4.4: The temperature dependence of the adiabatic temperature change $\Delta T_{ad}(T)$ on $5\ T$ magnetic field change (a) and magnetization $M(T)$ (b) for $Ni_{48.6}Mn_{34.9}Sn_{16.5}$. Dashed lines relate positions of austenite growth start A_s and finish A_f temperatures determined from $5\ mT$ magnetization curve.

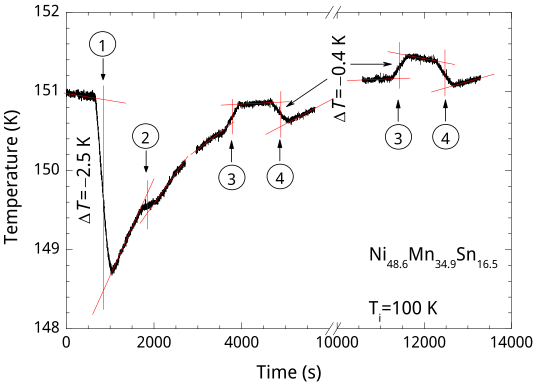

Figure 4.5: ΔT_{ad} of $Ni_{48.6}Mn_{34.9}Sn_{16.5}$ in a $5T$ magnetic-field-change. Point ① denotes field-increase-start, at which the temperature of the sample begins to decrease: inverse MCE. The field is decreased at point ②. Further applying ③ and removing ④ of the field causes warming and cooling, respectively: conventional MCE.

($229\ K < T < 260\ K$) it exhibits the inverse MCE. The maximum ΔT_{ad} observed equals $\approx 1\ K$, when the system is in the vicinity of the inflection point on the reverse transformation branch of the magnetization thermal hysteresis ($\approx 249\ K$, see fig. 4.6(d)).

We performed adiabatic $3\,T$ field-cycling experiments on $Ni_{51.3}Mn_{32.9}In_{15.8}$ sample. The sample was initially zero-field cooled down to $T_i = 100\ K$ and warmed in zero field to the measurement temperature, so that it resided on the reverse transformation branch. The results are shown in fig. 4.7(a): the initial application of the magnetic field (point ①) results in the negative temperature change $\Delta T_{ad} = 1.5\ K$ (inverse MCE), and all subsequent removing and applying the field result in reversible temperature change $|\Delta T_{ad}| = 0.7\ K$. Reversing the field direction at any cycle does not affect the magnitude of ΔT_{ad}.

$3\ T$ field-cycling measurement of the system residing on the forward transformation branch is shown in fig. 4.7(b). The sample was heated up to austenite state ($T_i = 280\,K$) in zero-field and subsequently cooled down to a mixed austenite/martensite state on the forward transformation branch at $251\ K$. On the initial application of the field (point ①) the system cools down by $0.7\ K$, exhibiting the inverse MCE. Unlike previous cases, on the field removal (point ②) the heating of the same magnitude is observed. On following field-change cycles the temperature change is reversible: $|\Delta T_{ad}| = 0.7\ K$.

4.2.3 $Ni_{50}Mn_{34}In_{15}Sn_1$

Figure 4.8 shows the temperature dependence of the adiabatic temperature change for the $Ni_{51.7}Mn_{32.1}In_{15.0}Sn_{1.2}$ sample in the $3\ T$ magnetic field. Prior to the each measurement the sample was zero-field cooled to $T_i = 140\ K$ and warmed up to the measurement temperature. So the sample resided on the reverse transformation branch of the transformation hysteresis. Below $A_s = 231\ K$ the system exhibits conventional MCE with the adiabatic temperature change $\Delta T_{ad} \approx 0.3\ K$. During the martensitic transition the sample exhibits inverse MCE. As in the previous cases the adiabatic temperature change on the applying the field (red filled symbols) is greater than on removing it (black filled symbols). The maximum adiabatic temperature change equals $-4.7\ K$ at $255\ K$ (close to $A_f = 260\ K$). Above A_f system again exhibits conventional MCE.

The result of the $3\ T$ field-cycling measurement is shown in fig. 4.9. The system was initially cooled in zero-field to $T_i = 140\ K$ and then heated up to 253.6 K. At this temperature system resides on the reverse transformation branch in a mixed state. Initially applying $3\ T$ field (point ①) leads to the negative adiabatic temperature change $\Delta T_{ad} = -4.7\ K$, and on removing the field (point ②) sample heats by $1.8\ K$. On the second application of the field (point ③) system cools by $1.8\ K$. On the following removal of the field (point ④) temperature slightly drops and then rises by $0.8\ K$. All subsequent cycles exhibit smaller temperature changes and the characteristic "hump" in the temperature dependence.

4.2.4 Transitional hysteresis

In fig. 4.10(a)-(b) we show the results on the thermal cycling of the magnetization in the region of the structural transition for the $Ni_{48.6}Mn_{34.9}Sn_{16.5}$ and the $Ni_{51.3}Mn_{32.9}In_{15.8}$ samples, respectively. Prior to each measurement, the samples were cooled below M_f in zero-field, where they are in the pure martensite state, and then heated up to the measurement temperature.

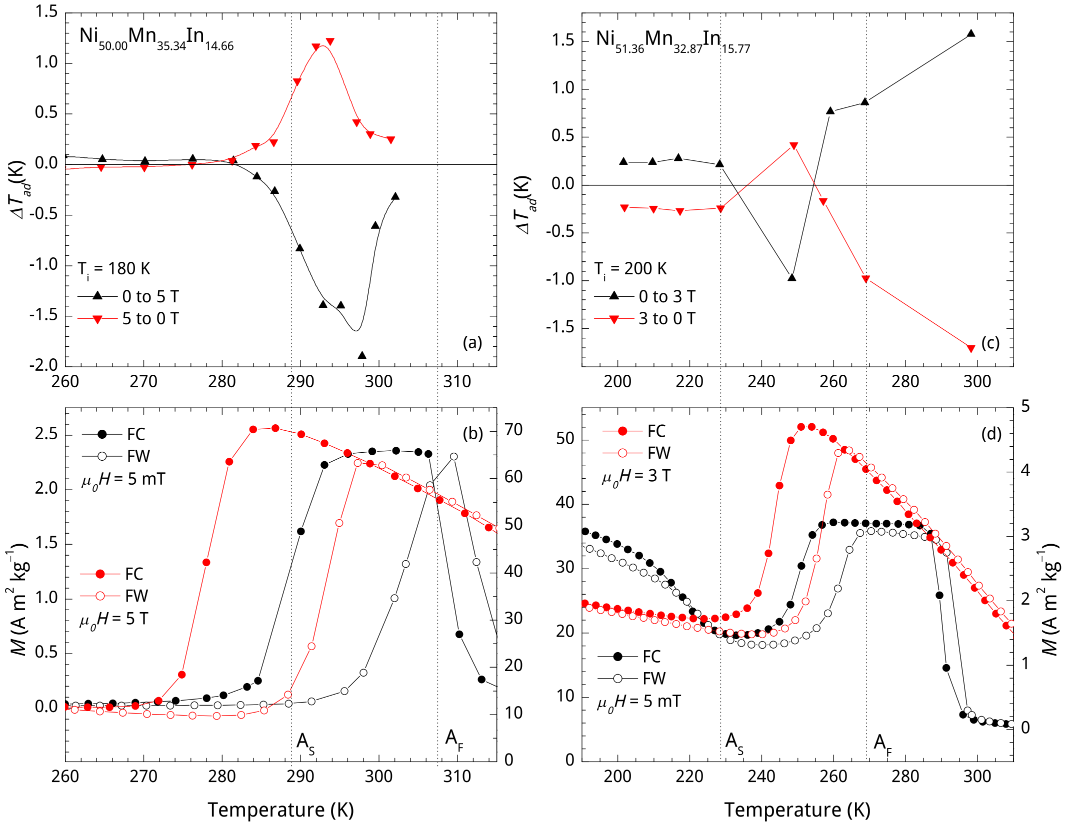

Figure 4.6: The temperature dependence of the adiabatic temperature change $\Delta T_{ad}(T)$ in a $5\ T$ magnetic-field-change (a) and magnetization $M(T)$ (b) for $Ni_{50.0}Mn_{35_3}In_{14.7}$.
The temperature dependence of the adiabatic temperature change $\Delta T_{ad}(T)$ in a $3\ T$ magnetic-field-change (c) and magnetization $M(T)$ (d) for $Ni_{51.3}Mn_{32.9}In_{15.8}$. Dashed lines relate positions of austenite growth start A_s and finish A_f temperatures determined from $5\ mT$ magnetization curves.

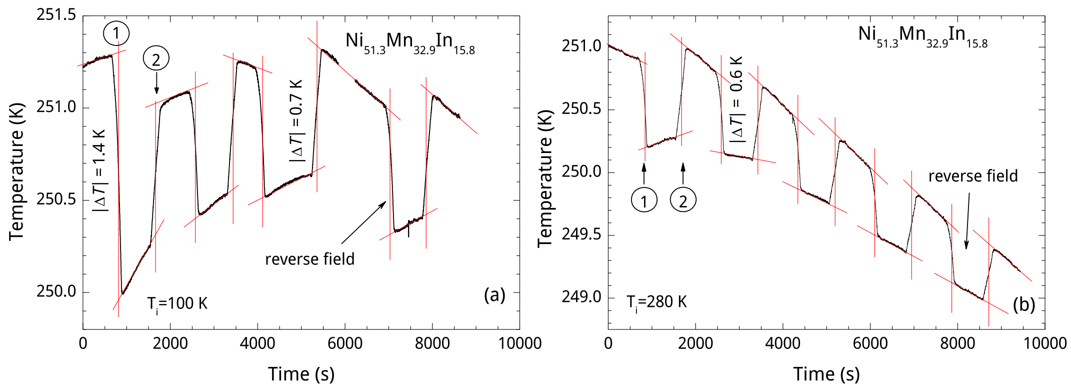

Figure 4.7: Field-cycling measurements between 0 and 3 T beginning in (a) the reverse and (b) the forward transformation branches for $Ni_{51.3}Mn_{32.9}In_{15.8}$. Points similar to ① and ② denote field-increase-start and field-decrease-start, respectively. A field-reversal at any particular cycle does not affect the behavior of ΔT_{ad}.

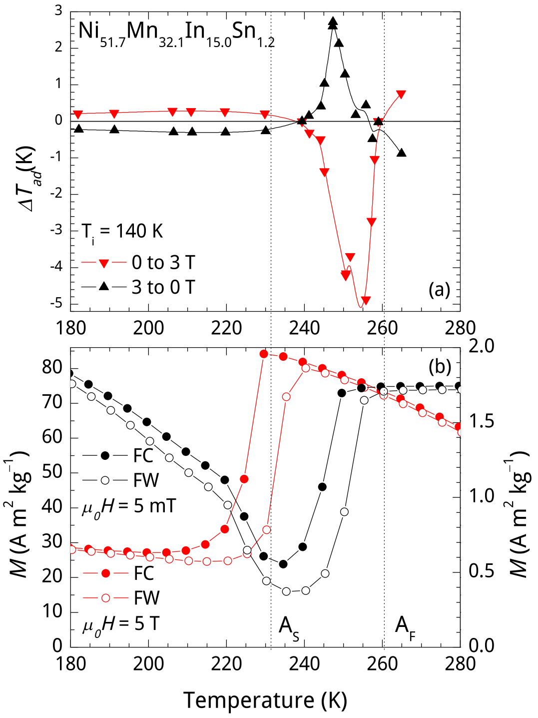

Figure 4.8: The temperature dependence of the adiabatic temperature change $\Delta T_{ad}(T)$ in a 3 T magnetic-field-change (a) and magnetization $M(T)$ (b) for $Ni_{51.7}Mn_{32.1}In_{15.0}Sn_{1.2}$. Dashed lines relate positions of austenite growth start A_s and finish A_f temperatures determined from $5\ mT$ magnetization curve.

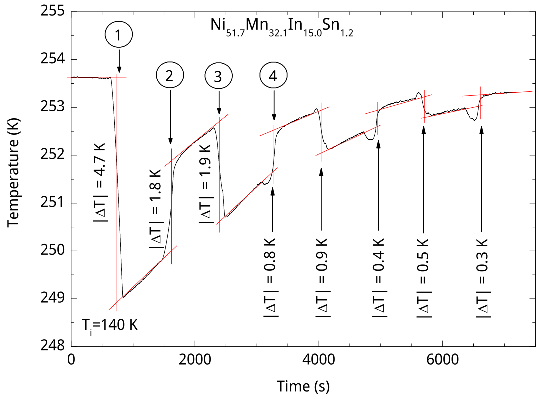

Figure 4.9: ΔT_{ad} of $Ni_{51.7}Mn_{32.1}In_{15.0}Sn_{1.2}$ in a 5 T magnetic-field-change. Point ① denotes field-increase-start, at which the temperature of the sample begins to decrease: inverse MCE. The field is decreased at point ②. Further applying ③ and removing ④ of the field causes cooling and warming with a reduced magnitude. On each field change starting from point ③ results in a "hump" on temperature dependence besides cooling or heating.

In the case of fig. 4.10(a), the sample was heated up to $145\ K$, where the state of the sample is at a point on the reverse transformation branch of the thermal hysteresis (point *a*). At this temperature the sample partially transforms into austenite. The austenite-to-martensite ratio on the reverse transformation branch can be estimated as

$$\frac{a}{m} = \frac{[M(T) - M(A_s)]}{[M(A_f) - M(A_s)]} \tag{4.1a}$$

where $M(A_s)$ and $M(A_f)$ are the magnetization values at the austenite start and finish temperatures, and $M(T)$ is the magnetization at a temperature within the transition ($A_s < T < A_f$).

Thus, $\frac{a}{m}$ rises on heating up to point *a*. On cooling from *a* to *b* ($T > M_s$), M(T) (and thus $\frac{a}{m}$) initially remains constant, then starts decreasing and approaches M_s, and below M_s it rapidly decreases until point *b* as martensite rebuilds in the sample. On heating from point *b*, austenite starts rebuilding at A_s and the system returns to point *a*. Cycling between *a* and *b* shows that system remains in a minor loop, and thus $\frac{a}{m}$ is reversible on this path.

However, if the system is cooled without reaching M_s (path between points *c* and *d*), $M(T)$ practically does not change, and $\frac{a}{m}$ remains constant. The similar case is observed when the system is heated from the state on the forward transformation branch.

The case of $Ni_{51.3}Mn_{32.9}In_{15.8}$ is shown in fig. 4.10(b). In this case when the system is cooled from the mixed state on the reverse transformation branch (point *a*) austenite-to-martensite ratio $\frac{a}{m}$ is initially constant, but as soon as the temperature is below M_s, M(T), and thus $\frac{a}{m}$, drops rapidly towards point *b* due to transformation towards the martensitic state. As in the previous case, repeating this process results in a minor loop (loop 1). A similar loop (loop 2) is observed on heating from the state on the forward transformation branch.

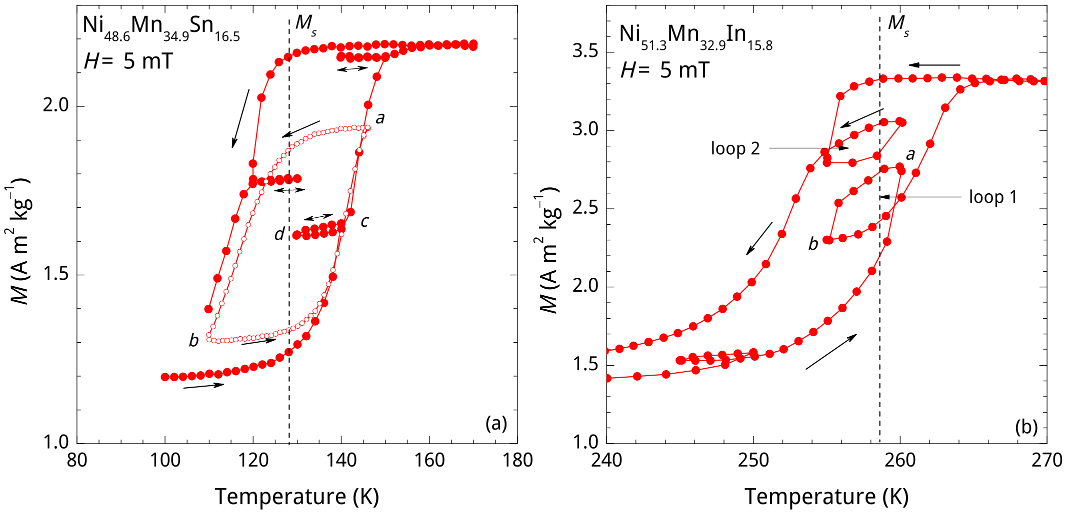

Figure 4.10: Minor loops within the thermal hysteresis of the magnetization under $5\ mT$ for $Ni_{48.6}Mn_{34.9}Sn_{16.5}$ (a) and $Ni_{51.3}Mn_{32.9}In_{15.8}$ (b).

4.3 Magnetic interactions in Ni-Mn-Ga and Ni-Mn-Sn alloys

4.3.1 Magnetic interactions in ordered magnetic state

On figs. 4.11 to 4.19 we show the summarized results for the different samples in $Ni - Mn - Ga$ and $Ni - Mn - Sn$ series. Each data set consists of the temperature dependence of the magnetization measured under FW protocol in $5\ mT$ and $1.6\ T$ fields, temperature dependence of the FMR spectrum $\frac{d\chi''}{dH}(H,T)$ represented in raw and normalized (as described in section 3.6.1) colormaps, and normalized FMR spectra $\frac{d\chi''}{dH}(H)$ at the selected temperatures.

Ni-Mn-Ga series

The first sample to be discussed is close to the stoichiometry $Ni_{49.95}Mn_{24.67}Ga_{25.38}$ with valent electron concentration e/a = 7.48. In fig. 4.11(a) we the show temperature dependence of the magnetization measured under FW protocol in $5\ mT$ and $1.6\ T$ in temperature range between $5\ K < T < 420\ K$. In $5\ mT$ the sample starts undergoing the structural martensitic transition at $A_s = 242\ K$ and then at higher temperatures it undergoes magnetic order-disorder transition in the austenite state at $T_C^A = 380\ K$.

In fig. 4.11(b) we show the temperature dependence of the measured FMR signal $\frac{d\chi''}{dH}(H,T)$. The signal magnitude below $A_s = 242\ K$ is lower than above A_s, and thus seen as a flat region due to the limited colormap graph resolution. Above A_s FMR line is at $\approx 0.25\ T$ (as seen on fig. 4.11(d), spectra measured at $300\ K$) and shifts towards isotropic value ω/γ at higher temperatures, above austenitic Curie temperature $T_C^A = 380\ K$ the FMR line equals isotropic value (fig. 4.11(d), spectra measured at $420\ K$ (PM state).

In fig. 4.11(c) we show the temperature dependence of the normalized FMR signal $\frac{d\chi''}{dH}(H,T)$. Below A_s the FMR signal consists of two resonance lines: below and above isotropic value, while above A_s only a single line below ω/γ is detected. The characteristic FMR-spectra, measured at $100\ K$, is shown on fig. 4.11(d). The resonance line above ω/γ lies at $H \approx 1.2\ T$ at $5\ K$ and shifts towards $1.1\ T$ as temperature rises up to A_s. The resonance line below ω/γ lies at $H \approx 0.2\ T$ below A_s and $H \approx 0.25\ T$ in the temperature region between $A_s < T < T_C^A = 380\ K$. Above the Curie temperature the system is paramagnetic as resonance line lies at the isotropic value.

Next case to be discussed is Mn-rich Ni-deficient $Ni_{45.18}Mn_{30.37}Ga_{24.44}$ sample (e/a = 7.38). According to the magnetization data shown on fig. 4.12(a) in the temperature region between $5\ K < T < 470\ K$ this sample undergoes two transitions: a structural transition from the martensite to the austenite phase starting at $A_s = 185\ K$, and a magnetic order-disorder transition in the austenite phase at $T_C^A = 390\ K$.

The temperature dependence of the measured FMR signal (fig. 4.12(b)) is somewhat similar to the previous case: the raw FMR signal above the structural transition is higher than the one below A_s. Above A_s one line below ω/γ is observed. On increasing temperature it shifts towards isotropic value, and equals it above T_C^A. The temperature dependence of the normalized FMR signal (fig. 4.12(c)) shows more detailed picture for the martensite phase (below the structural transition temperature A_s). Two resonance lines are observed below A_s: at $\approx 1\ T$ and $\approx 0.15\ T$ (e.g. consider normalized FMR signal measured at $100\ K$ on fig. 4.12(d)). Above A_s up to $\approx 270\ K$ only a single resonance line at $H \approx 0.2\ T$ is observed. However, above $\approx 270\ K$ an additional line emerges at $\approx 50\ mT$. The characteristic normalized spectra measured at $300\ K$ is shown on (fig. 4.12(d).

On further heating this line shifts towards the isotropic value, and equals $H \approx 344\,mT$ above $T_C^A = 390\ K$ (e.g. normalized FMR signal measured at $470\ K$ on fig. 4.12(d)).

The temperature dependence of the magnetization of the Mn-deficient $Ni_{49.06}Mn_{20.28}Ga_{30.66}$ sample is shown on fig. 4.13(a). No sign of the structural transition is observed in the temperature region between $5\ K < T < 400\ K$. However, the sample undergoes the magnetic order-disorder transition in the austenite state at $T_C^A = 295\ K$. In fig. 4.13(b) we show the temperature dependence of the measured FMR signal $\frac{d\chi''}{dH}(H,T)$ in the temperature range between $5\ K < T < 450\ K$. Below the T_C^A the measured signal shows a single resonance line at $H \approx 0.3\ T$ with the magnitude rising with the temperature. Above the Curie temperature the line lies at $H = \omega/\gamma$ and the system is paramagnetic.

The temperature dependence of the normalized FMR signal $\frac{d\chi''}{dH}(H,T)$, shown on fig. 4.11(c), provides more detailed information on the temperature behavior of the FMR spectrum. At low temperatures FMR signal consists of the two resonance lines: one is at $H \approx 0.3\ T$, while the second line is at $H \approx 0.1\ T$. The intensity of the second FMR line in comparison to the first one decreases with temperature, so above $250\ K$ second line is not observed anymore. One can see this tendency comparing the FMR spectra measured at $100\ K$ and $230\ K$ shown on fig. 4.13(d).

Above $T_C^A = 295\ K$ only single resonance line is present at $H = 344\ mT$. The characteristic spectrum $\frac{d\chi''}{dH}(H)$ measured at $370\ K$ is shown on fig. 4.13(d).

The last sample to be discussed in the Ni-Mn-Ga series is the Mn-rich $Ni_{49.97}Mn_{30.35}Ga_{19.68}$ sample (e/a = 7.71). We show on fig. 4.14(a) the temperature dependence of the magnetization measured under FW protocol in $5\,mT$ and $1.6\,T$ in temperature range between $5\ K < T < 400\ K$. In the plotted region magnetization $M(T)$ gradually decreases and no sign of the structural transition is observed. Thus decrease in magnetization is related to the magnetic transition in the martensite state at $T_C^M = 373\ K$[1].

The measured raw FMR signal is shown on fig. 4.14(b). Below $T_C^M = 373\ K$ this data shows a single line above ω/γ, which appears at $200\ K$ and then shifts towards isotropic value as the temperature increases. Only a single resonance line at isotropic value is observed above T_C^M. In contrast to the samples mentioned before we have a slowly increasing FM-AF exchange with decreasing temperature.

The normalized FMR signal is shown on fig. 4.14(c). Below T_C^M two resonance lines, lying below and above ω/γ are observed (e.g. FMR spectrum measured at $100\,K$ on fig. 4.14(d)). One resonance line lies at $H \approx 0.1\,T$ at $5\,K$ and shifts towards isotropic value as the temperature increases. The other one lies at $H = 0.55\,T$ and shifts towards higher fields up to $150\,K$, and then approaches isotropic value, which it reaches above $300\,K$. The FMR spectrum measured at $300\,K$ (fig. 4.14(d)) exhibits asymmetrical signal below isotropic value. This signal can be reconstructed as one FM line lying below ω/γ and AF line lying just over isotropic value. As the temperature increases this AF line vanishes. Above $400\ K$ resonance line lies at isotropic value, as seen on FMR spectrum measured at $450\ K$ (fig. 4.14(d))

---

[1] E.g. compare with the FW branch of magnetization $M(T)$ of $Ni_{50}Mn_{37}Sn_{13}$ on fig. 2.10(c) and fig. 2.10(e)

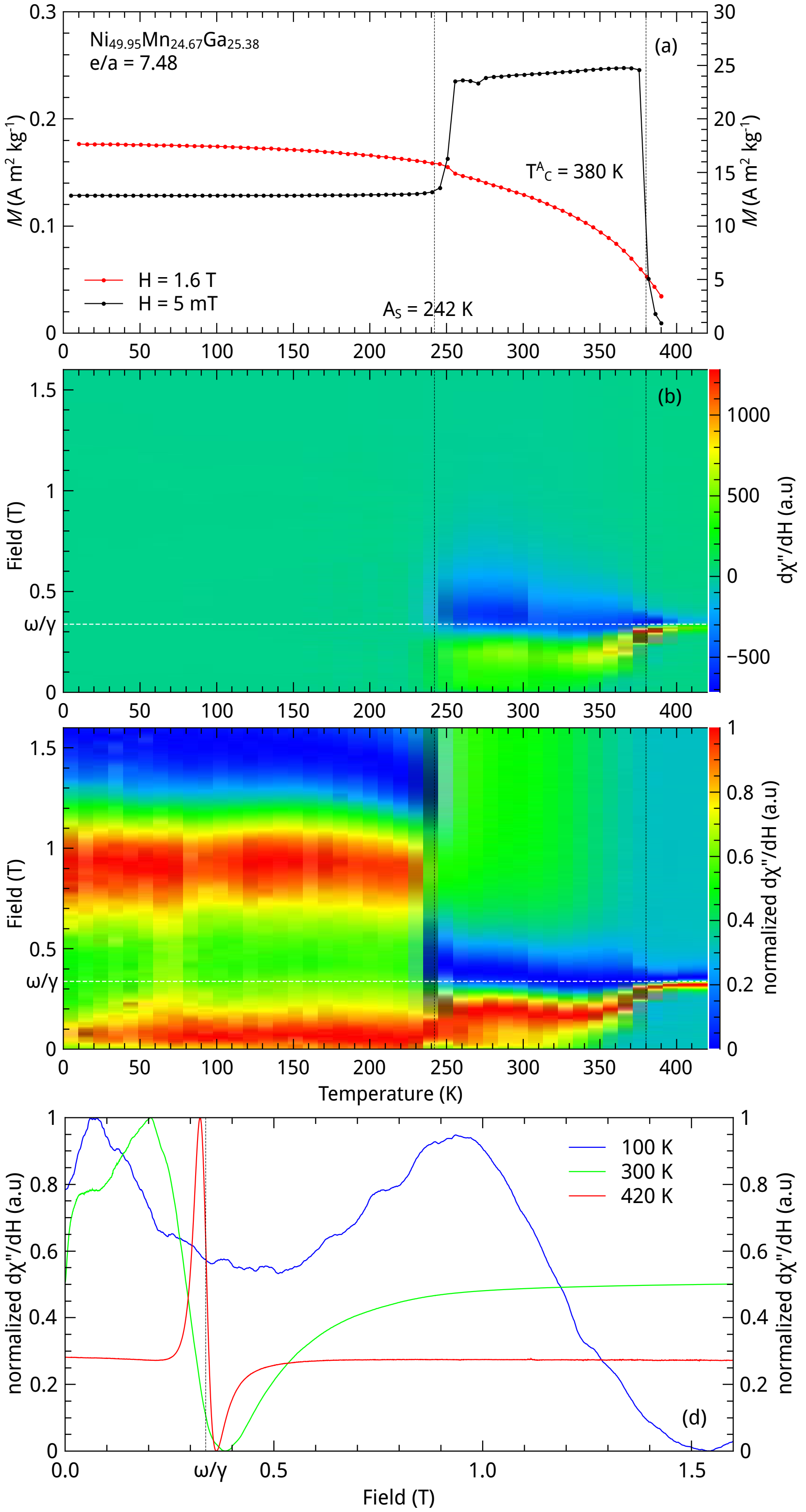

Figure 4.11: Temperature dependence of the measured FMR signal ($\frac{d\chi''}{dH}$) (b) and normalized measured FMR signal ($\frac{d\chi''}{dH}$) (c) with magnetization measured under FW protocol in $5\ mT$ and $1.6\ T$ field (a) of $Ni_{49.95}Mn_{24.67}Ga_{25.38}$. Fig. (d) shows the FMR spectra measured on increasing field at the selected temperatures.

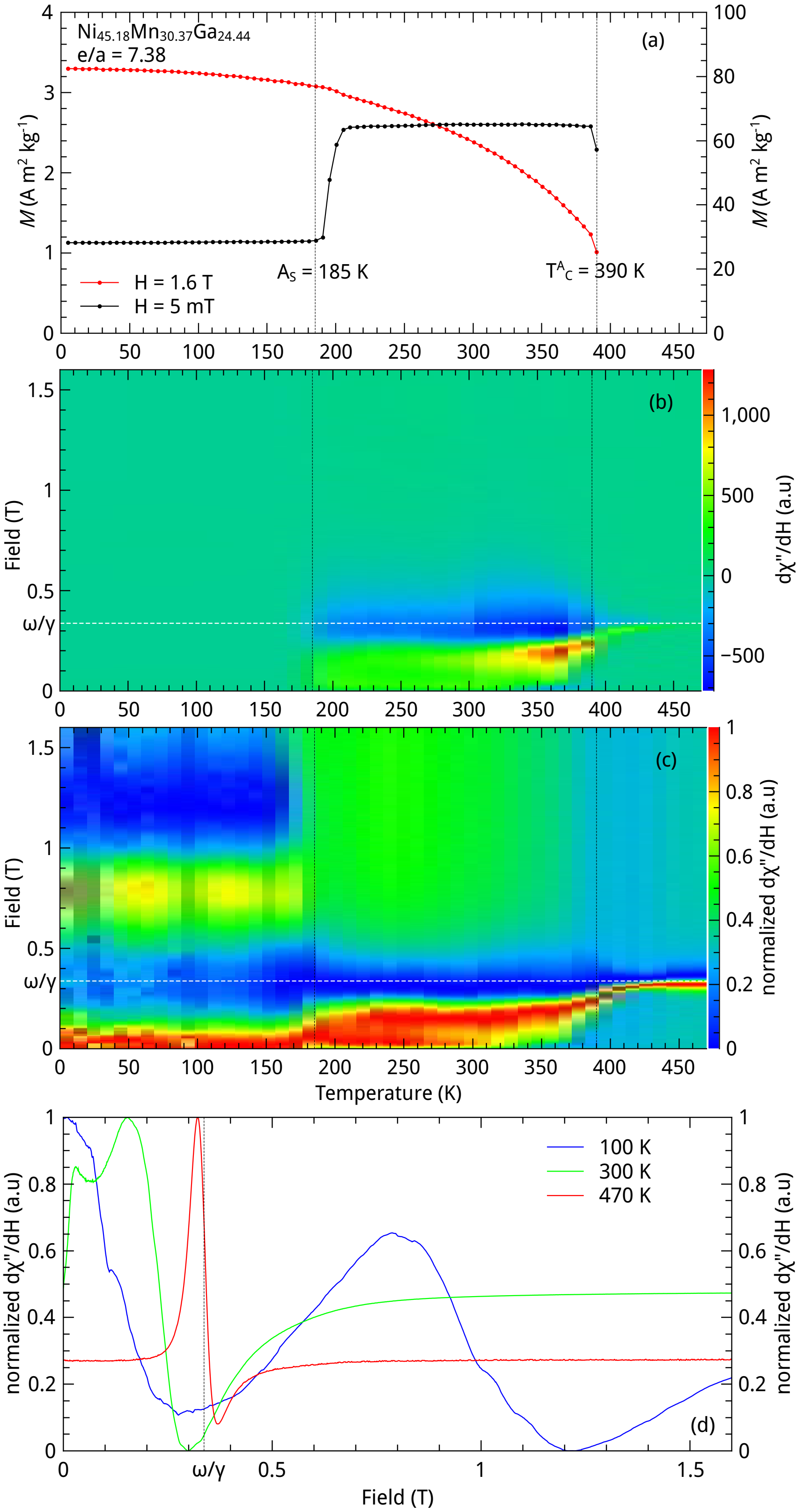

Figure 4.12: Temperature dependence of the measured FMR signal $(\frac{d\chi''}{dH})$ (b) and normalized measured FMR signal $(\frac{d\chi''}{dH})$ (c) with magnetization measured under FW protocol in $5\ mT$ and $1.6\ T$ field (a) of $Ni_{45.18}Mn_{30.37}Ga_{24.44}$ Fig. (d) shows the FMR spectra measured on increasing field at the selected temperatures.

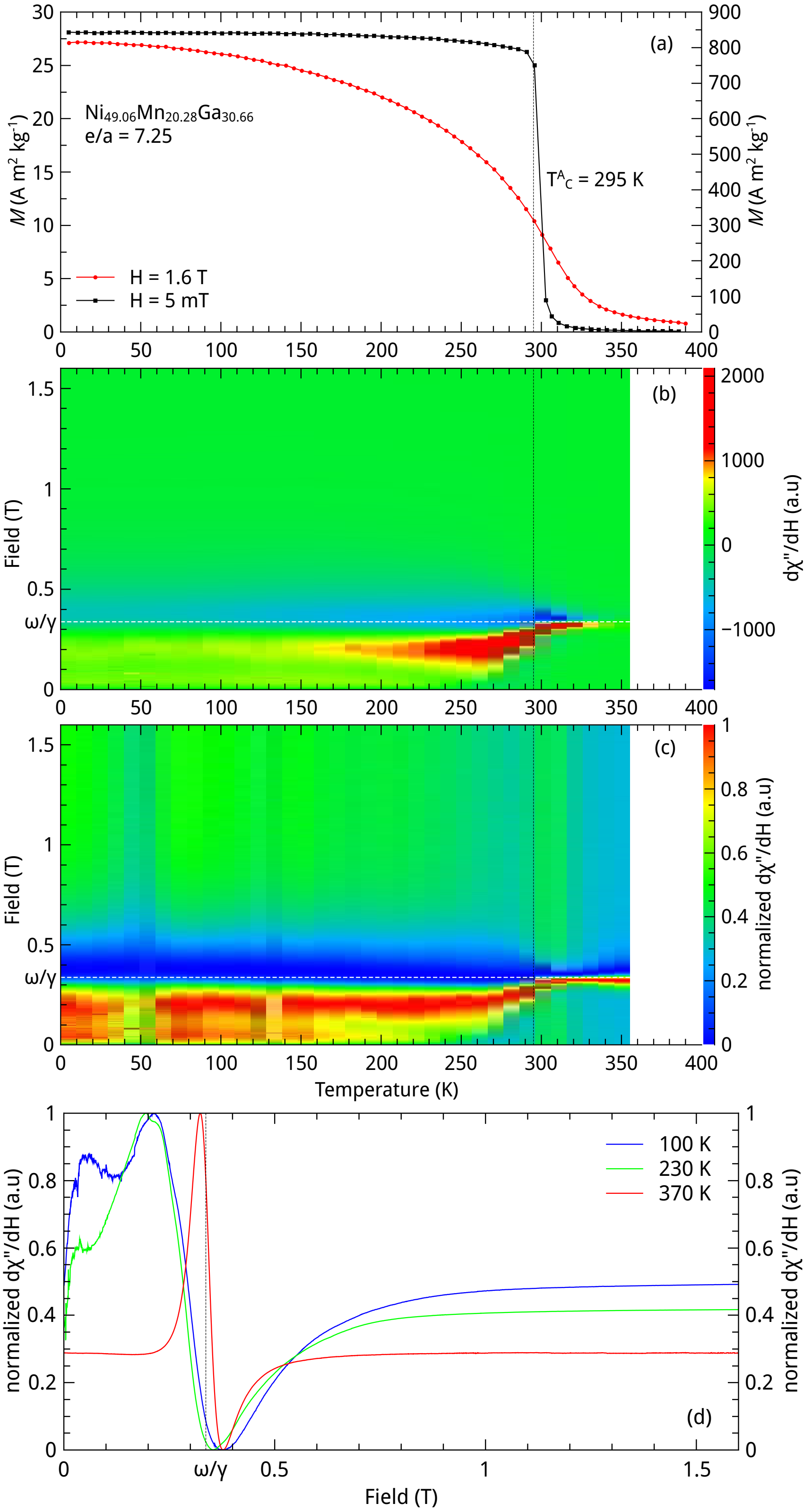

Figure 4.13: Temperature dependence of the measured FMR signal ($\frac{d\chi''}{dH}$) (b) and normalized measured FMR signal ($\frac{d\chi''}{dH}$) (c) with magnetization measured under FW protocol in $5\ mT$ and $1.6\ T$ field (a) of the $Ni_{49.06}Mn_{20.28}Ga_{30.66}$ sample. Fig. (d) shows the FMR spectra measured on increasing field at the selected temperatures.

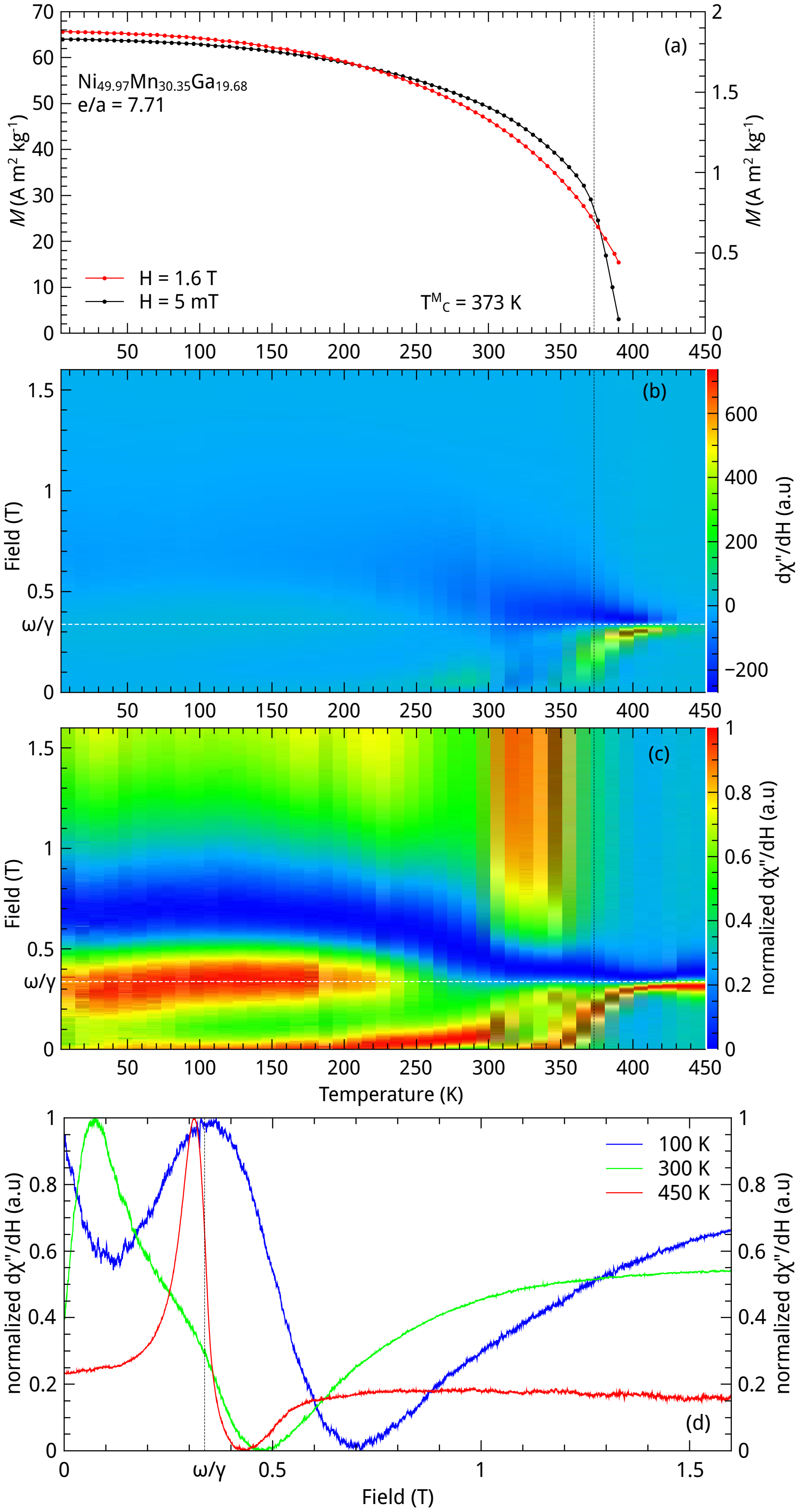

Figure 4.14: Temperature dependence of the measured FMR signal $(\frac{d\chi''}{dH})$ (b) and normalized measured FMR signal $(\frac{d\chi''}{dH})$ (c) with magnetization measured under FW protocol in $5\ mT$ and $1.6\ T$ field (a) of the $Ni_{49.97}Mn_{30.35}Ga_{19.68}$ sample. Fig. (d) shows the FMR spectra measured on increasing field at the selected temperatures.

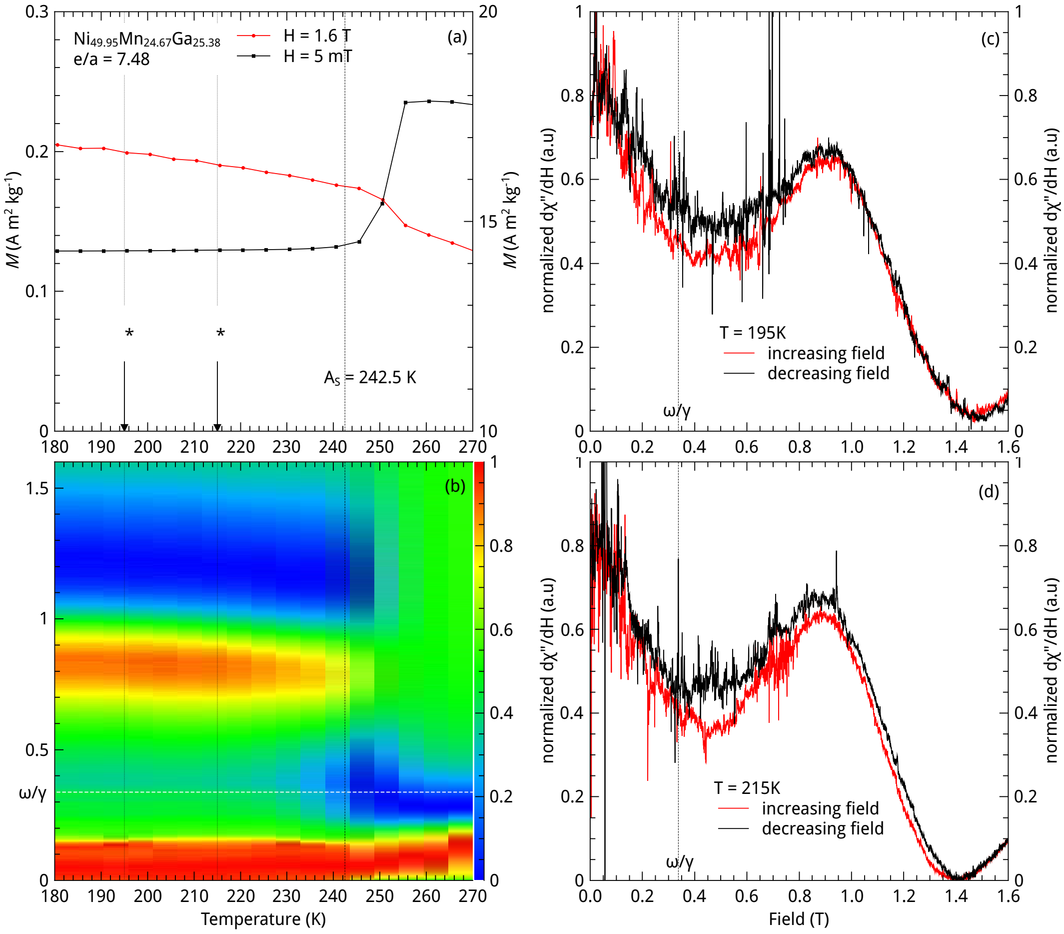

Figure 4.15: Temperature dependence of the normalized FMR signal $\frac{d\chi''}{dH}(H,T)$ (b) with magnetization measured under FW protocol in $5\ mT$ and $1.6\ T$ field (a) of $Ni_{49.95}Mn_{24.67}Ga_{25.38}$ sample. Field dependence of normalized FMR signal $\frac{d\chi''}{dH}(H)$ on increasing and decreasing field at $195\ K$ (c) and $215\ K$ (d). Asterisks on fig. (a) mark temperatures of field-cycling measurements shown on fig. (c) and (d).

Field cycling effects in Ni_2MnGa

We studied the effect of the field cycling on the measured FMR signal $\frac{d\chi''}{dH}(H,T)$ in the $Ni_{49.95}Mn_{24.67}Ga_{25.38}$ sample in the martensite state at different temperatures. For these measurements we deposited a small amount of the powder sample ($\leq 0.5\ mg$) on the adhesive tape and put it into the evacuated suprasil tube. Several field-dependent measurements were performed at chosen temperatures. After stabilizing the temperature, the field was increased to the maximum ($H = 1.6\ T$) and then decreased to zero, while $\frac{d\chi''}{dH}(H)$ was measured.

The results of these measurements are shown on fig. 4.15(c) and (d).

In fig. 4.15(a) we show temperature dependence of the magnetization $M(T)$ measured under FW protocol in $5\ mT$ and $1.6\ T$ in the temperature range between $180\ K < T < 270\ K$. In $5\ mT$ field sample starts undergoing structural transition from the martensite to the austenite phase at $A_s = 242.5\ K$ and is austenitic at $A_f \approx 256\ K$. In $1.6\ T$ it is difficult to determine A_s temperature, however it doesn't seem to shift considerably and equals $\approx 256\ K$ as in $5\ mT$. For the convenience A_s and A_f temperatures determined by the magnetization studies are shown by the dashed lines on the fig. 4.15(a) and (b).

We show the temperature dependence of the normalized FMR signal $\frac{d\chi''}{dH}(H,T)$ measured on increasing field on fig. 4.15(b). Below $T \approx 256\ K$ the FMR signal consists of two lines: below and above isotropic value ($\omega/\gamma \approx 330\ mT$). Above this temperature there is only single FM line below isotropic value. The approximate position of the FMR line, lying below the isotropic value, is about $0.2\ T$, at temperatures above $242.5\ K$ it shifts towards isotropic value. The position of the line above isotropic value is $\approx 1.1\ T$ and it remains constant up to austenite finish temperature $A_f \approx 256\ K$, while above this temperature it is not detected.

In fig. 4.15(c) we show the field dependence of the normalized FMR signal $\frac{d\chi''}{dH}(H)$ measured on increasing (black line) and decreasing (red line) field at $T = 195\ K < A_s$. Both signals feature two FMR lines: below and above isotropic value. The signal measured on the increasing field lies higher than the one measured on the decreasing field (in fields up to $0.9\ T$) and show higher noise magnitude than the one measured on decreasing field.

In fig. 4.15(d) we show the field dependence of the normalized FMR signal $\frac{d\chi''}{dH}(H)$ measured on increasing and decreasing field at $T = 215\ K < A_s$. This case is similar to the one shown on fig. 4.15(c). However, in this case the increasing-field signal lies higher than the decreasing-field one in fields up to $1.4\ T$.

Ni-Mn-Sn series

First, we discuss the case of the close to the stoichiometry $Ni_{49.17}Mn_{23.98}Ga_{26.31}$ sample with the valence electron concentration e/a = 7.70. Magnetization data in the temperature region between $5\ K < T < 400\ K$ for this sample is shown on fig. 4.16(a). According to this data, in the depicted region the sample undergoes only magnetic order-disorder transition in the austenitic state at the temperature $T_C^A = 270\ K$.

We show the temperature dependence of the measured FMR signal $\frac{d\chi''}{dH}(H,T)$ on fig. 4.16(b). Initially, at $5\ K$, the resonance line lies slightly above isotropic value ($H \approx 346\ mT$) and shifts towards ω/γ as the temperature increases. However, at $T = 90\ K$ resonance line position abruptly changes to $H = 305\ mT$, so it lies below ω/γ. On further heating the line position shifts towards lower fields and its magnitude rises, and up to $T = 270\ K$ then moves to isotropic value as the sample passes the Curie temperature.

The temperature dependence of the normalized FMR signal $\frac{d\chi''}{dH}(H,T)$ is shown on fig. 4.16(c). It shows the same resonance line behavior as on the previous graph. Additionally, it is seen from the graph that the FMR signal width remains constant up to $\approx 250\ K$. The characteristic spectrum measured at $100\ K$ is shown on fig. 4.16(d).The resonance line position is estimated as $0.3\ T$, the asymmetry of the signal shape is related to the presence of the angle distribution of the anisotropy in the powder. Above $\approx 250\ K$ the resonance line shifts towards the isotropic value, while it width decreases (see the FMR spectrum measured at $300\ K$ on fig. 4.16(d).) Above $320\ K$ the resonance line lies at $H = \omega/\gamma$, as it can be seen on fig. 4.16(d) ($400\ K$).

The next case to be discussed here is the Ni-rich Mn-deficient $Ni_{54.65}Mn_{19.29}Sn_{26.06}$ sample with e/a = 7.86. In fig. 4.17(a) we show the temperature dependence of the magnetization for this sample in the temperature range between $5\ K$ and $400\ K$. In the plotted region the sample undergoes FM-PM transition in the austenitic state at $T_C^A = 340\ K$, while no structural transition is observed. We show the temperature dependence of the measured FMR signal $\frac{d\chi''}{dH}(H,T)$ on fig. 4.17(b). The behavior of the FMR spectrum is much similar to the previous case of the $Ni_{49.17}Mn_{23.98}Ga_{26.31}$ sample. It is difficult to determine resonance line position below $60\ K$ due to the low resolution of the colormap. Above $60\ K$ the resonance line lies at $H \approx 210\,mT$. On further heating above $280\ K$ the resonance line shifts towards ω/γ and resides at this value above $340\ K$. The temperature dependence of the normalized signal (fig. 4.17(c)) shows the same behavior as on the previous figure. Initially, the resonance line position is slightly below the isotropic value ($H \approx 300\ mT$). On further heating the line position doesn't change up to $T = 60\ K$, where it changes abruptly to $H = 210\,mT$. The characteristic spectrum measured at $100\ K$ is shown on fig. 4.17(d). The asymmetry of the measured signal is attributed to the distribution of anisotropies in the powder sample. On further heating the line position remains constant up to $280\ K$, where it starts shifting towards the isotropic value with the increasing temperature, while its width decreases. The normalized signal measured at $300\ K$ (fig. 4.17(d)) is slightly shifted towards ω/γ and features smaller width than the one measured at $100\ K$. Above $T_C^A = 280\ K$ the line position equals to the isotropic value as could be seen from the signal measured at $400\ K$.

In fig. 4.18(a) we show the temperature dependence of the magnetization of the Mn-rich $Ni_{49.38}Mn_{34.80}Sn_{15.82}$ sample (e/a = 8.01) measured under $5\ mT$ and $1.6\ T$ magnetic field. On heating this sample undergoes the structural transition from the martensite to the austenite, which starts at $A_s = 70\ K$. The transition finishes at the austenite finish temperature $A_f \approx 200\ K$. On further heating the sample undergoes magnetic order-disorder transition in the austenitic state at $T_C^A = 320\ K$.

In fig. 4.18(b) the temperature dependence of the measured FMR signal $\frac{d\chi''}{dH}(H,T)$ is shown. It is difficult to determine the line positions below $150\ K$ due to the low contrast of the colormap graph. However, above $150\ K$ one resonance below isotropic value is observed. The signal magnitude rises with the temperature up to $280\ K$, and the line position shifts to higher fields and equals isotropic value above $330\ K$.

Figure 4.18(c) shows the resonance line behavior in more detail. Below $160\ K$ two resonance lines below and above ω/γ are observed. The line below ω/γ lies at $H \approx 150\,mT$ and shifts to higher fields with temperature. The line above ω/γ lies at $H \approx 700\,mT$ at $5\ K$ and shifts towards $H \approx 500\,mT$ at $150\ K$ and then vanishes above this temperature. For example the characteristic spectrum measured at $100\ K$ (shown on fig. 4.18(d)) features 2 resonance lines at $H \approx 150\,mT$ and $550\,mT$, respectively.

Above $200\ K$ the width of the FM increases as it shifts towards isotropic value. The characteristic FMR signal measured at $300\ K$ shows 2 resonance lines: one at $H \approx 300\,mT$ and the second one at very low field values. Above $340\ K$ the FMR line lies at $H = \omega/\gamma$ (e.g. the signal measured at $380\ K$, shown on fig. 4.18(d)).

The last sample to be discussed is the $Ni_{49.37}Mn_{40.31}Sn_{9.92}$ with valence electron concentration e/a = 8.16. In fig. 4.19(a) we show temperature dependence of the magnetization $M(T)$. According to the data, the sample does not transform in this temperature range, however it undergoes the magnetic transition in the martensite state at $T_C^M = 280\ K$. In fig. 4.19(b) the temperature dependence of the measured FMR signal is shown. It is difficult to determine line positions below $100\ K$ due to the low contrast of the colormap graph. However, above $100\ K$ there is one resonance line at $H = 100\ mT$ shifting to the ω/γ value as temperature increases. The FMR signal exhibits maximum intensity at $T = 210\ K$. While, above $280\ K$ it is again difficult to determine the line position due to the low contrast of the colormap graph.

Figure 4.19(c) shows resonance line behavior in more detail. At $5\ K$ there are two resonance lines present: at $H \approx 160\ mT$ and $H \approx 450\ mT$. The first line position remains constant up to $150\ K$, then it shifts towards isotropic value which it reaches at $220\ K$. On heating the second line shifts to higher fields up to $30\ K$ and then moves towards the isotropic value. It reaches the isotropic value at $110\ K$.

Two characteristic spectra measured at $5\ K$ and $100\ K$ (fig. 4.19(d)) show several resonance lines lying below and above ω/γ.

However, the characteristic spectra measured at $250\ K$ shows several FM lines up to $H = \omega/\gamma$. Above $300\ K$ another resonance line is observed at low fields: it starts at $30\ mT$, above $310\ K$ shifts to $80\ mT$ with the increasing temperature. The characteristic FMR spectrum measured at $470\ K$ (fig. 4.19(d)) shows the superposition of the two resonance lines: one lying below ω/γ, and the second one close to the isotropic value.

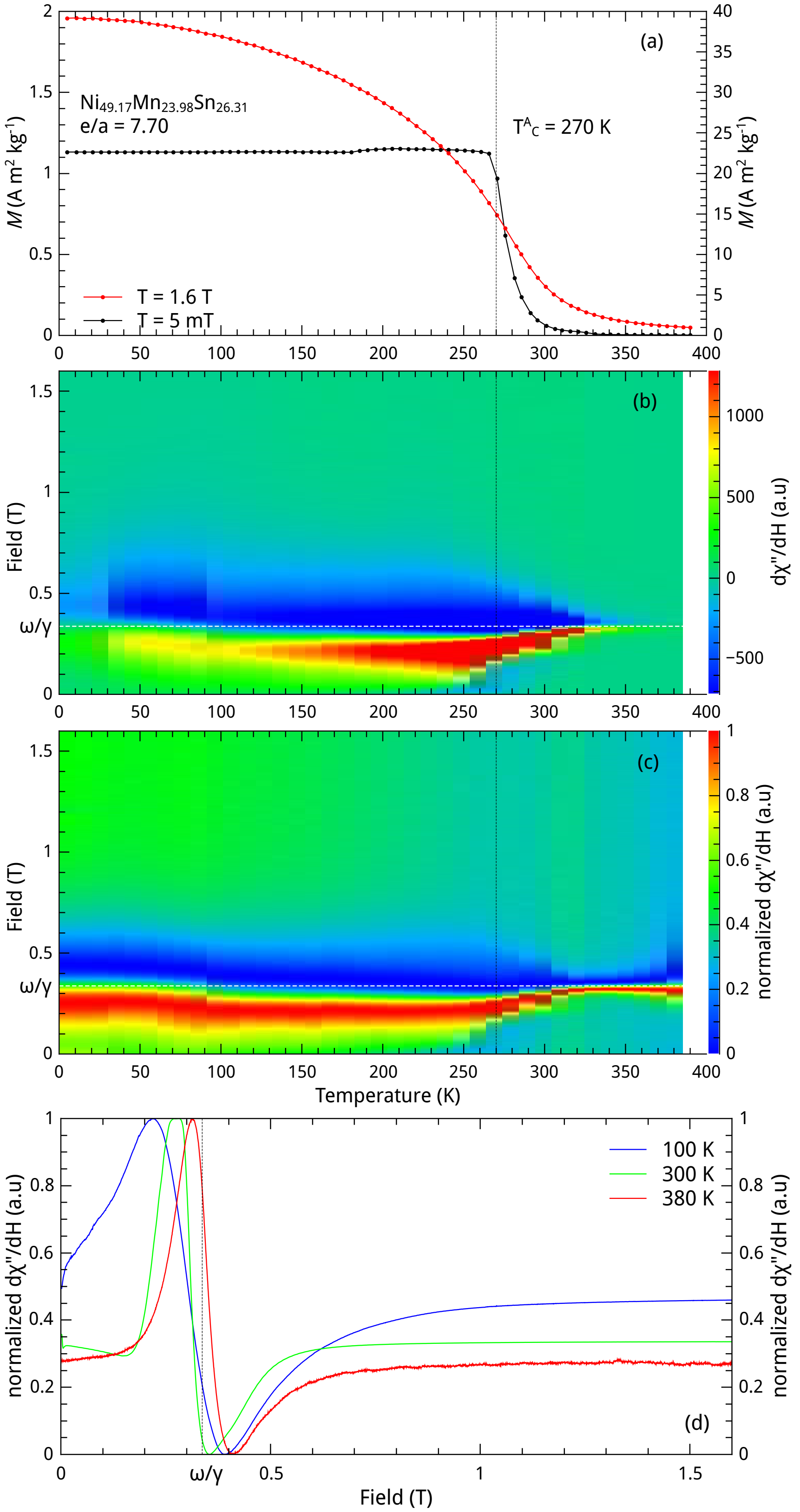

Figure 4.16: Temperature dependence of the measured FMR signal ($\frac{d\chi''}{dH}$) (b) and normalized measured FMR signal ($\frac{d\chi''}{dH}$) (c) with magnetization measured under FW protocol in $5\ mT$ and $1.6\ T$ field (a) of the $Ni_{49.17}Mn_{23.98}Sn_{26.31}$ sample.Fig. (d) shows the FMR spectra measured on increasing field at the selected temperatures.

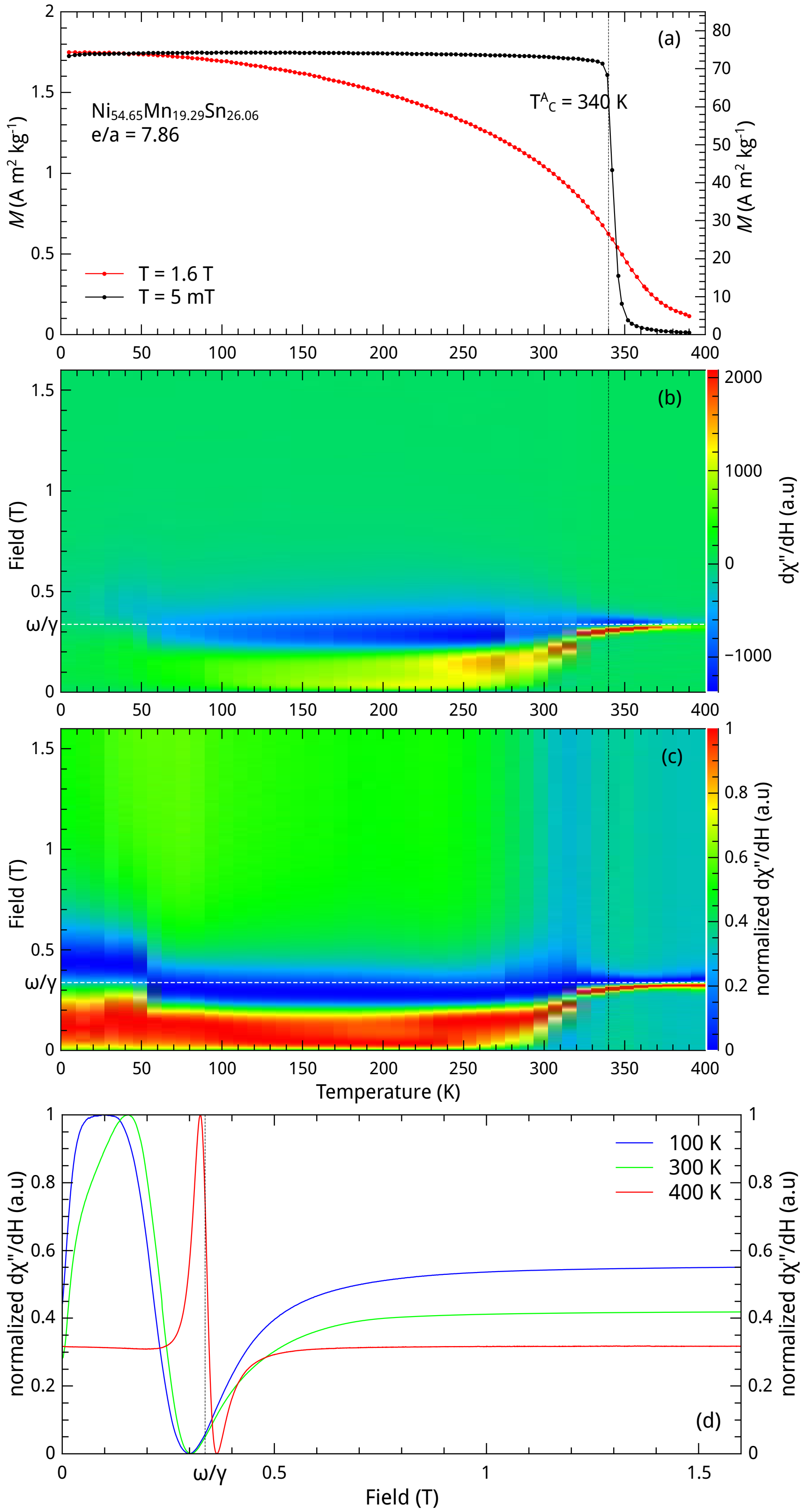

Figure 4.17: Temperature dependence of the measured FMR signal ($\frac{d\chi''}{dH}$) (b) and normalized measured FMR signal ($\frac{d\chi''}{dH}$) (c) with magnetization measured under FW protocol in $5\ mT$ and $1.6\ T$ field (a) of the $Ni_{54.65}Mn_{19.29}Sn_{26.06}$ sample. Fig. (d) shows the FMR spectra measured on increasing field at the selected temperatures.

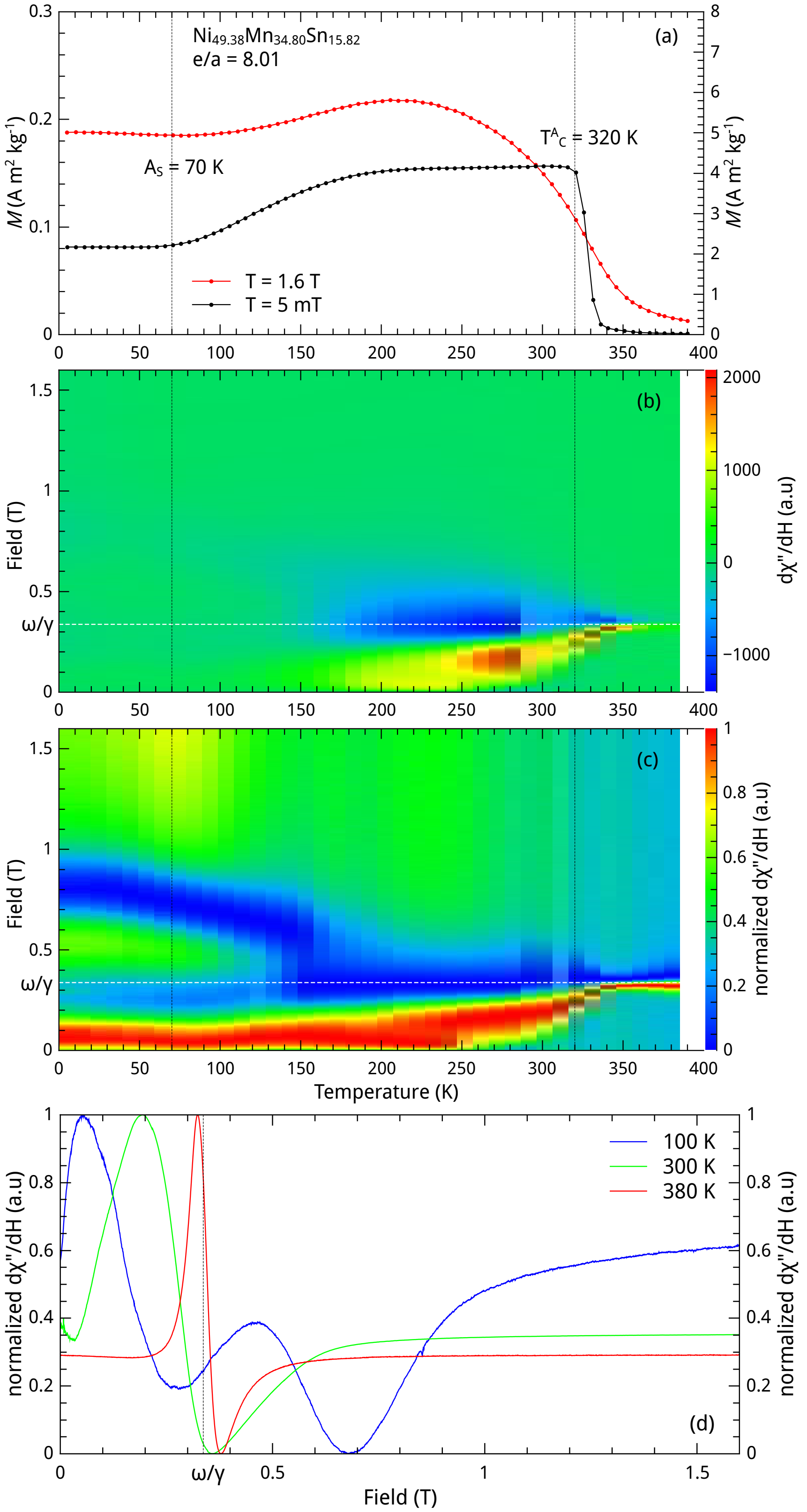

Figure 4.18: Temperature dependence of the measured FMR signal ($\frac{d\chi''}{dH}$) (b) and normalized measured FMR signal ($\frac{d\chi''}{dH}$) (c) with magnetization measured under FW protocol in $5\ mT$ and $1.6\ T$ field (a) of the $Ni_{49.38}Mn_{34.80}Sn_{15.82}$ sample. Fig. (d) shows the FMR spectra measured on increasing field at the selected temperatures.

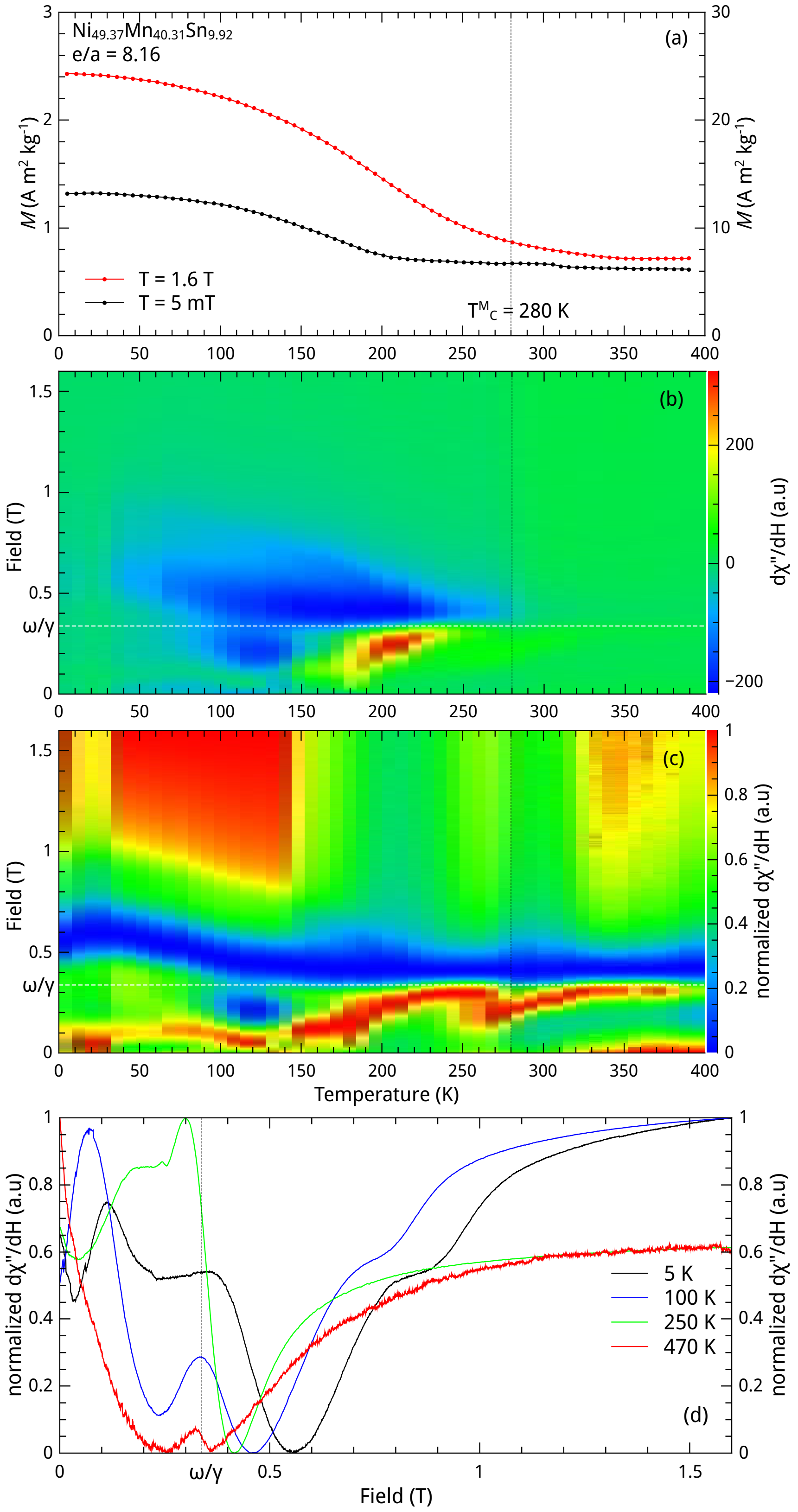

Figure 4.19: Temperature dependence of the measured FMR signal ($\frac{d\chi''}{dH}$) (b) and normalized measured FMR signal ($\frac{d\chi''}{dH}$) (c) with magnetization measured under FW protocol in $5\ mT$ and $1.6\ T$ field (a) of the $Ni_{49.37}Mn_{40.31}Sn_{9.92}$ sample. Fig. (d) shows the FMR spectra measured on increasing field at the selected temperatures.

4.3.2 Magnetic interactions in disordered magnetic state

For each sample we have measured the temperature dependence of the magnetization from the ZFC state (a) and the flipping ratio (b) (see e.g. fig. 4.20) and performed polarized neutron scattering measurements in the paramagnetic austenite state ($T = 500\ K$). The scattering data were then separated into nuclear (c) and magnetic (d) cross sections as described in section 3.5.2.

Ni-Mn-Ga series

The temperature dependence of magnetization between $300\ K$ and $400\ K$ of the $Ni_{45.18}Mn_{30.37}Ga_{24.44}$ sample is shown in fig. 4.20(a). In this region, the magnetization slowly decreases with increasing temperature and begins to drop as it approaches the Curie temperature in the austenite state ($T_C^A \approx 390\ K$).

The temperature dependence of the flipping ratio R_F measured between $300\ K$ and $500\ K$ is shown in fig. 4.20(b). The flipping ratio R_F equals 1 in the magnetically ordered state since the polarized neutron beam is depolarized by ferromagnetic domains, while above T_C^A, where the sample is in the paramagnetic state, R_F abruptly rises to ≈ 30.

Additionally, neutron depolarization measurement were made at $T = 500\ K > T_C^A$. The results of the cross section separation are shown in fig. 4.20(c) and (d). According to the q-dependence of the nuclear cross section (fig. 4.20(c)) at this temperature, the sample is in the cubic austenitic state with $L2_1$ symmetry (lattice parameter $a = 5.95(5)\ \AA$).

The q-dependence of the magnetic cross section $q(\AA^{-1})$ exhibits substantial forward scattering at low q-values and a hump in the diffuse scattering in q-range $1.2 < q(\AA^{-1}) < 2.2$. The drops at 1.8 and 2.1 $\AA^{-1}$ are related to separation errors at structural peak positions. Such scattering is explained by the presence of both ferromagnetic and antiferromagnetic correlations in the paramagnetic austenite phase.

In the Mn-rich $Ni_{49.97}Mn_{30.35}Ga_{19.68}$ sample, Ni occupies its own sublattice, while Mn occupies its own and also 20% of the Ga sublattice. In fig. 4.21(a), the temperature dependence of the magnetization on warming from the ZFC state is shown in range between $300\ K$ and $400\ K$. Initially, the magnetization increases as the temperature approaches T_C^M and then drops. Therefore, the flipping ratio $R_F(T)$ (fig. 4.21(b)) exhibits the opposite behavior: below T_C^M the beam is depolarized, and above T_C^M it rises up to 22 then slowly decreases.

We performed polarized neutrons scattering measurements at $400\ K$ and $500\ K$. In fig. 4.21(c) the nuclear cross sections at $400\ K$ (black symbols) and at $500\ K$ (red symbols) are shown. At the lower temperature, the sample is in the martensite state with orthorhombic $Pnnm$ structure (lattice parameters $a = 5.92(2)\ \AA$, $b = 5.58(6)\ \AA$, $c = 6.25(4)\ \AA$. At the higher temperature, the sample is in the austenitic state, although a certain amount of martensite is present as seen by the presence of reflections related to the martensite structure with lower intensity (the peak positions are shown by the black arrows). Austenite has a cubic lattice with parameter $a = 5.93(2)\ \AA$.

In fig. 4.21(d) the magnetic cross sections at $400\ K$ (black symbols) and $500\ K$ (red symbols) are shown. The q-dependence of the magnetic cross section exhibits forward scattering at low q-value and diffuse scattering in the range $1.2 < q(\AA^{-1}) < 2.3$. The magnetic cross section at $500\ K$ exhibits similar behavior, however the values lie slightly higher than at $400\ K$.

In $Ni_{49.95}Mn_{24.67}Ga_{25.38}$ each Ni, Mn and Ga atom occupies its own sublattice. According to the temperature dependence of the magnetization shown in fig. 4.22(a),

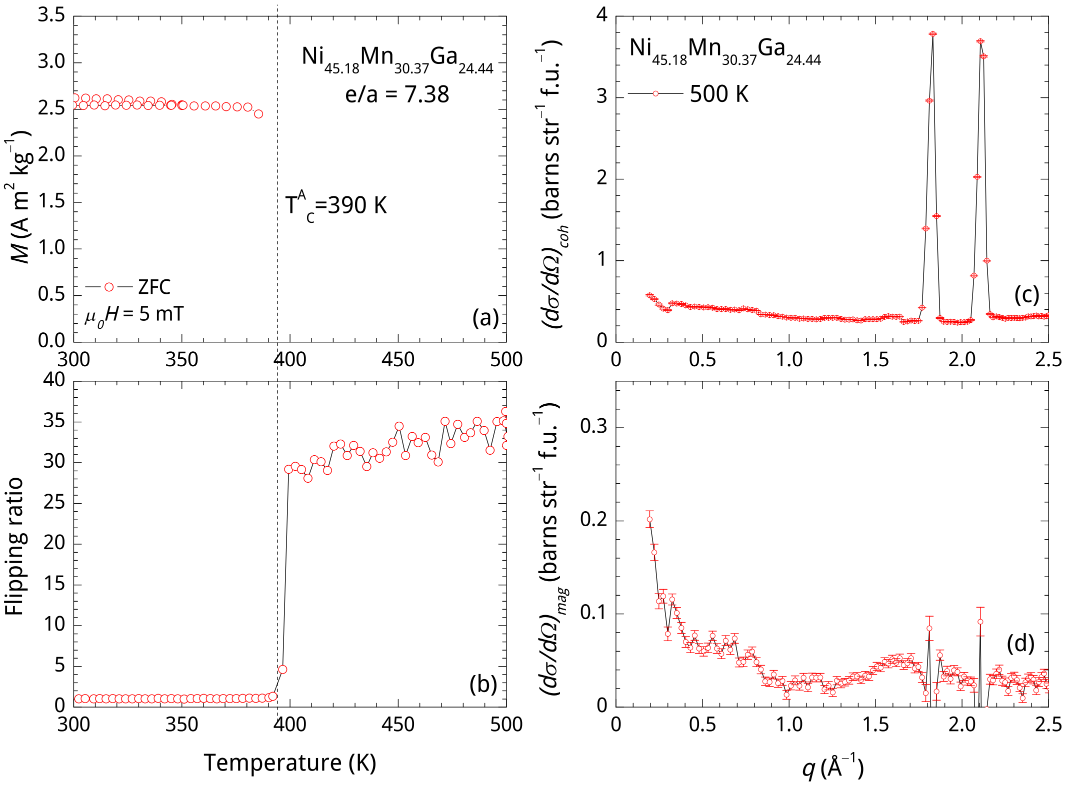

Figure 4.20: Temperature dependence of magnetization measured from ZFC state in $5\ mT$ (a), flipping ratio (b); nuclear (c) and magnetic (d) cross sections at $500\ K$ for $Ni_{45.18}Mn_{30.37}Ga_{24.44}$ sample.

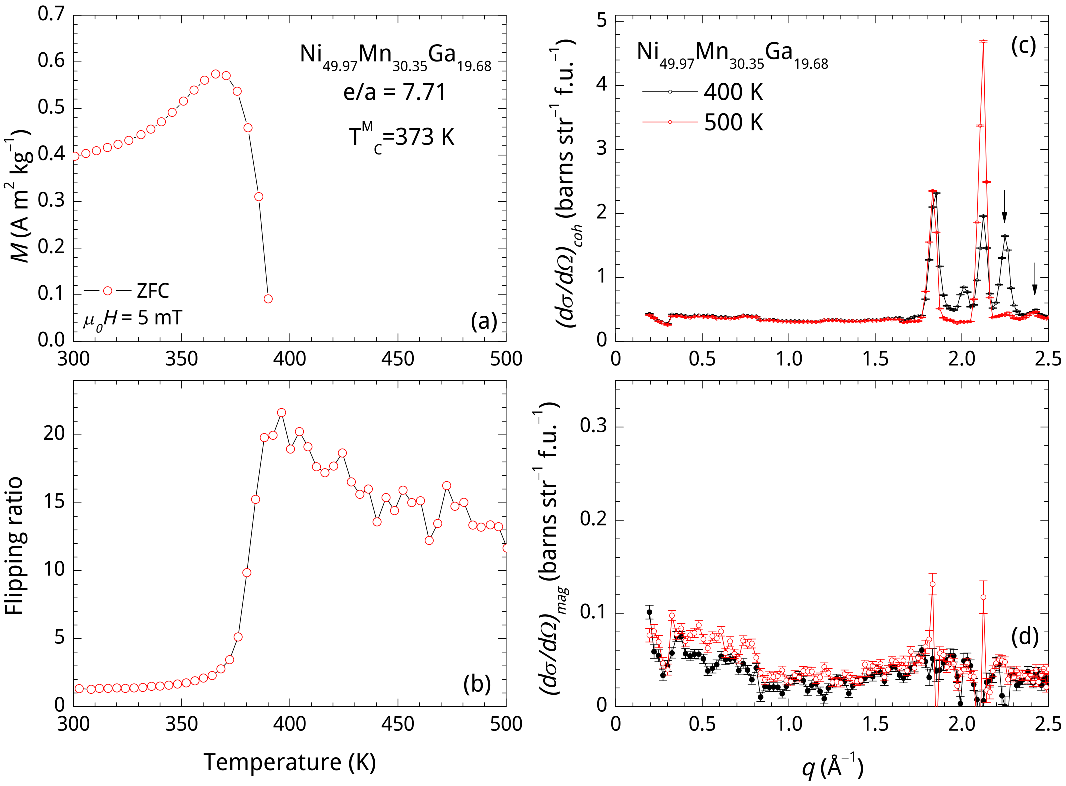

Figure 4.21: Temperature dependence of magnetization measured from ZFC state in $5\ mT$ (a), flipping ratio (b); nuclear (c) and magnetic (d) cross sections at $400\ K$ and $500\ K$ for $Ni_{49.97}Mn_{30.35}Ga_{19.68}$ sample.

the sample undergoes a FM↔PM transition at $T_C^A = 380\ K$. The temperature dependence of the flipping ratio shown in fig. 4.22(b) exhibits similar behavior: below $T_C^A = 380\ K$ FM domains depolarize the beam, while above T_C^A the flipping ratio is high ($R_F \approx 30$), indicating that no FM domains above $380\ K$ are present.

The nuclear cross section data (see fig. 4.22(c)) shows that $Ni_{49.95}Mn_{24.67}Ga_{25.38}$ is in the austenite state at $500\ K$ with $L2_1$ crystallographic symmetry. The lattice parameters derived from the the nuclear cross section spectrum is $a = 5.92(9)\ \mathring{A}$. The magnetic cross sections measured at the same temperature exhibits forward scattering at low q-values. However, the hump in the diffuse scattering at $1.3 < q(\mathring{A}^{-1}) < 2.5$ is considerably lower than for the case of the previously discussed samples.

Ni-Mn-Sn series

As was shown in section 4.1, the close-to-stoichiometry sample with $e/a = 7.70$, $Ni_{49.17}Mn_{23.98}Sn_{26.31}$, undergoes a magnetic transition around $T_C^A = 280\ K$ so that between $300\ K$ and $400\ K$, $M(T)$ is close to 0 (see fig. 4.23(a)). The temperature dependence of the flipping ratio starts with $R_F(T) \approx 20$ at $300\ K$, corresponding to the state with low magnetization, and rises with increasing the temperature up to $R_F \gtrsim 25$.

The nuclear scattering given in fig. 4.23 shows that the sample is in the cubic austenite state with lattice parameter $a = 5.93(5)\ \mathring{A}$ ($L2_1$ symmetry). The magnetic cross sections shows considerable forward scattering at low q-values and diffuse scattering between $1.0 < q(\mathring{A}^{-1}) < 2.5$.

On warming the Mn-rich $Ni_{49.38}Mn_{34.80}Sn_{15.82}$ sample with $e/a = 8.01$ from the ZFC state in $5\ mT$, the magnetization exhibits a considerable drop due to the ferromagnetic-to-paramagnetic transition at $T_C^A = 320\ K$ as seen in fig. 4.24(a). The temperature dependence of the flipping ratio R_F is shown in fig. 4.24(b). It remains constant up to $T \approx 325\ K$ and then starts rising towards $R_F \approx 35$ at $375\ K$ and remains constant up to $500\ K$.

The nuclear scattering in fig. 4.24(c) shows that at $500\ K$ the sample is austenitic with lattice parameter $a = 6.15(2)\ \mathring{A}$.

The magnetic scattering at the same temperature exhibits considerable forward scattering at low q-values, and finite diffuse scattering for $1.2 < q(\mathring{A}^{-1}) < 2.0$.

For the Ni-rich, Mn-deficient $Ni_{54.65}Mn_{19.29}Sn_{26.06}$ sample with $e/a = 7.86$, the ZFC magnetization drops at Curie temperature $T_C^A = 345\ K$ (fig. 4.25(a)). The beam is depolarized at $300\ K$, and the flipping ratio R_F increases towards 20 as the temperature rises above the Curie temperature T_C^A (see fig. 4.25(b)).

The nuclear scattering spectrum at $500\ K$ shown in fig. 4.25(c) suggests that at $500\ K$ the sample is in the austenite state with lattice parameter $a = 6.11(1)\ \mathring{A}$. The magnetic cross section (fig. 4.25(d)) also shows forward scattering and some diffuse scattering around $q = 1.8\ \mathring{A}^{-1}$.

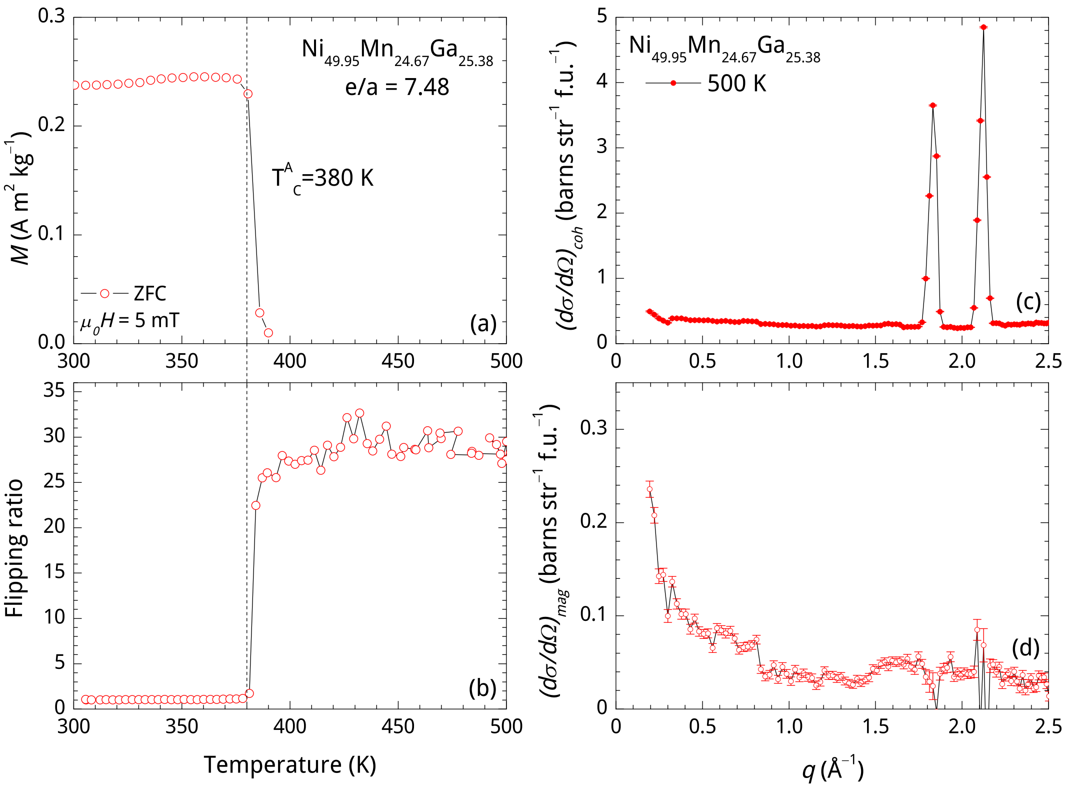

Figure 4.22: Temperature dependence of magnetization measured from ZFC state in $5\ mT$ (a), flipping ratio (b); nuclear (c) and magnetic (d) cross sections at $500\ K$ for $Ni_{49.95}Mn_{24.67}Ga_{25.38}$ sample.

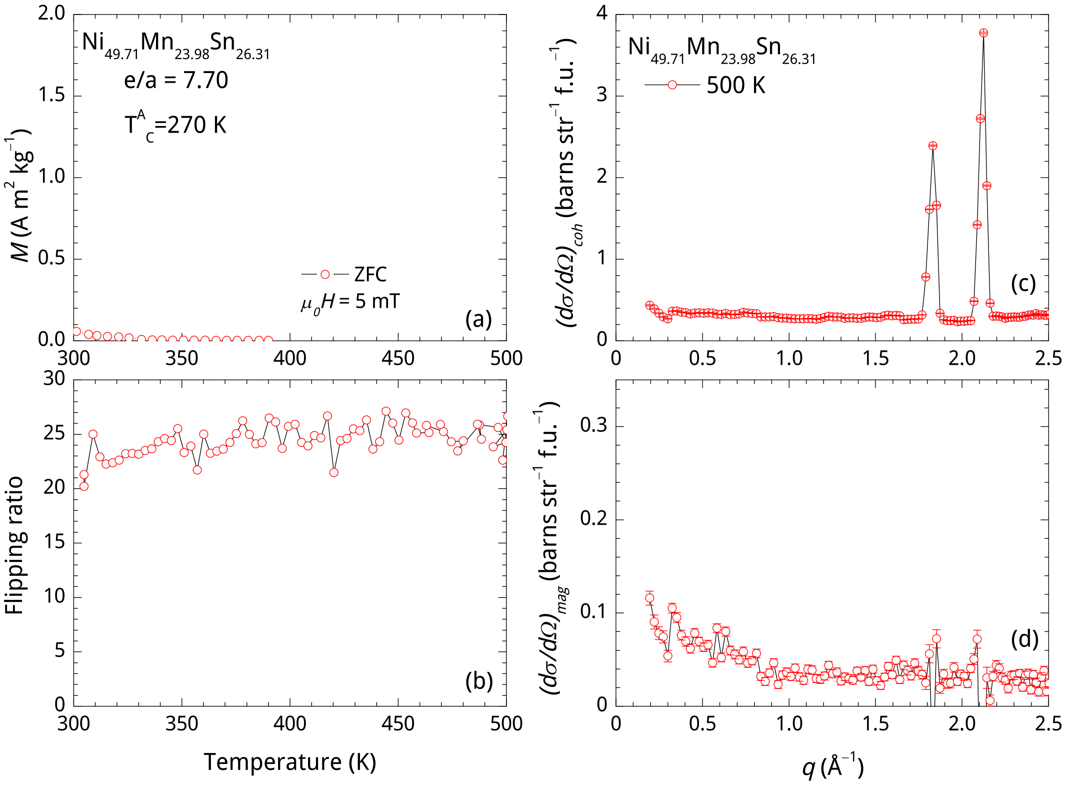

Figure 4.23: Temperature dependence of magnetization measured from ZFC state in $5\ mT$ (a), flipping ratio (b); nuclear (c) and magnetic (d) cross sections at $500\ K$ for $Ni_{49.17}Mn_{23.98}Sn_{26.31}$ sample.

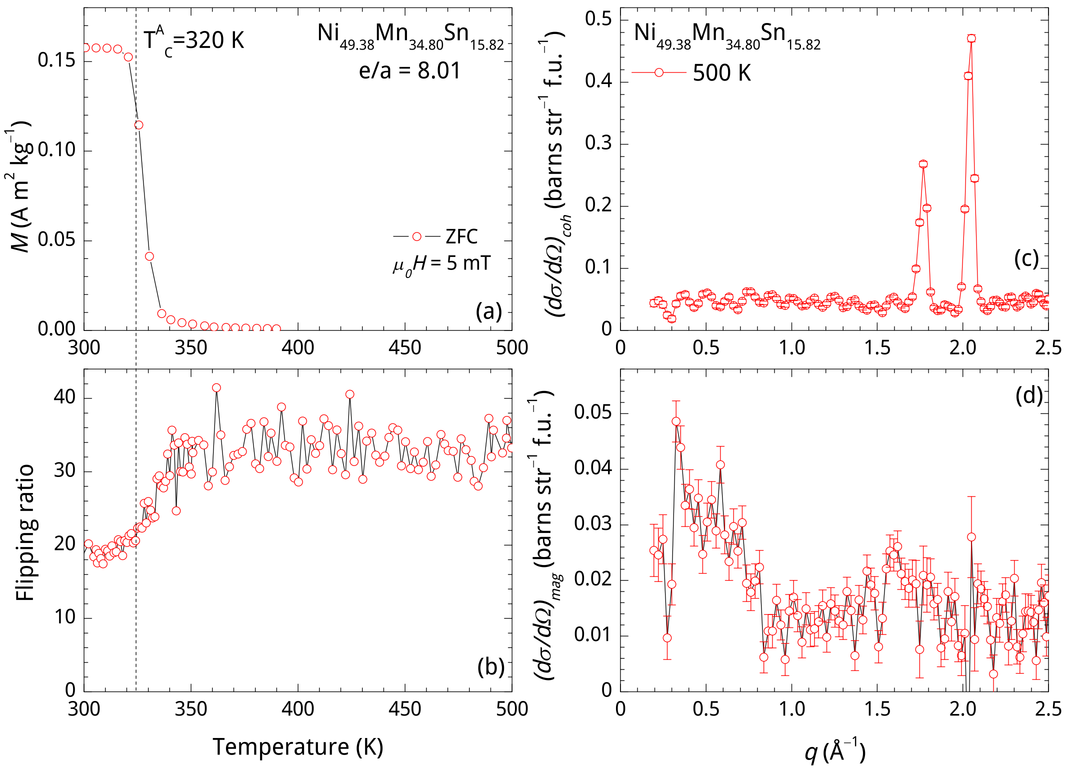

Figure 4.24: Temperature dependence of magnetization measured from ZFC state in $5\ mT$ (a), flipping ratio (b); nuclear (c) and magnetic (d) cross sections at $500\ K$ for $Ni_{49.38}Mn_{34.80}Sn_{15.82}$ sample.

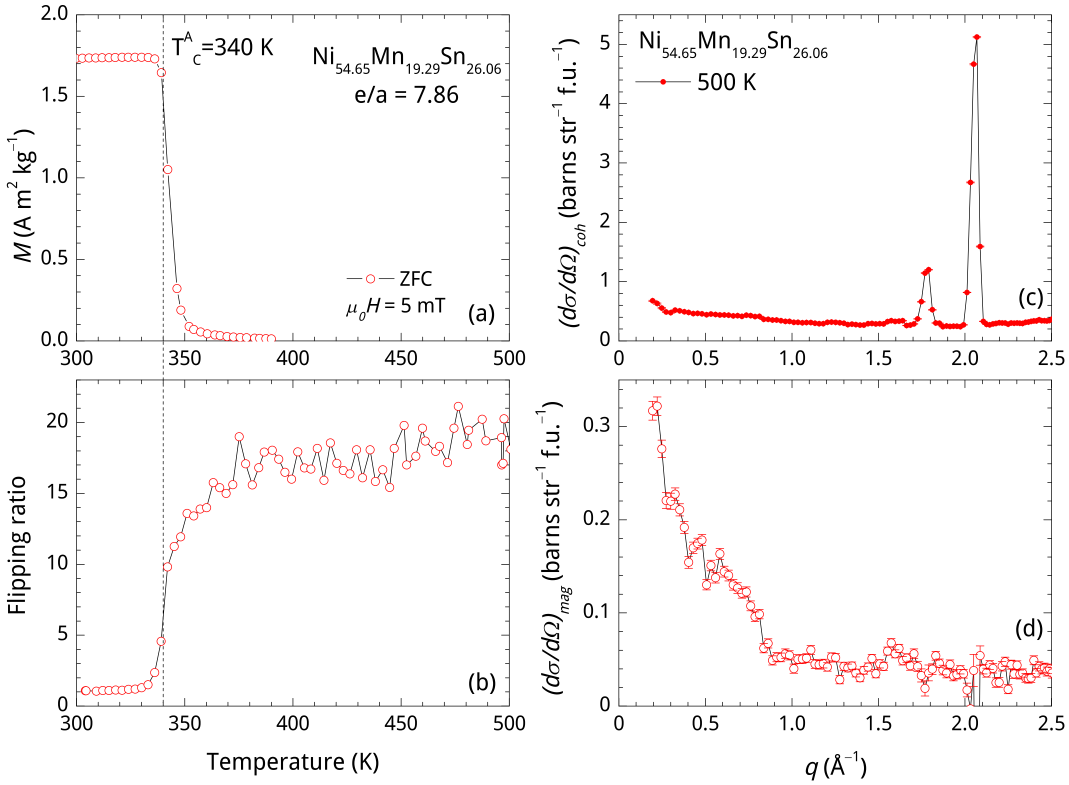

Figure 4.25: Temperature dependence of magnetization measured from ZFC state in $5\ mT$ (a), flipping ratio (b); nuclear (c) and magnetic (d) cross sections at $500\ K$ for $Ni_{54.65}Mn_{19.29}Sn_{26.06}$ sample.

4.4 Temperature behavior of neutron depolarization in $Ni_{45}Co_5Mn_{35}In_{15}$

We present the `differential scanning calorimetry measurements` (DSC) performed on the $Ni_{45}Mn_{35}In_{15}Co_5$ sample in the temperature range between $200\ K$ and $520\ K$ in fig. 4.26(a). The data points measured on cooling and warming are marked with blue and red colors, respectively. We choose the transition temperatures as the points where the temperature dependence of the specific heat $\frac{dQ}{dT}(T)$ starts to deviate from the baseline (e.g. see schematic drawing in fig. 2.1). The dashed lines running through the figures in fig. 4.26 provide a guide for transition temperatures, denoted with arrows and labels.

On warming, the sample undergoes a structural transition from the martensite to the austenite phase. The transition is seen as a peak in the $\frac{dQ}{dT}(T)$ diagram. The transition start and finish temperatures A_s and A_f are determined as $255\ K$ and $306\ K$, respectively. On further warming, the sample, when in the austenite state, undergoes a magnetic order-disorder transition, observed as a rapid drop of the specific heat at $T_C^A = 393\ K$. No other transition is observed by the DSC measurement up to $520\ K$.

On cooling from $520\ K$ the sample passes through the Curie temperature at $393\ K$, seen as a small kink in the $\frac{dQ}{dT}(T)$ diagram. On further cooling, it undergoes the structural transition from the austenite to the martensite seen as a drop in the specific heat. The transition start and finish temperatures M_s and M_f are determined as $289\ K$ and $242\ K$, respectively. No further transition is detected down to $200\ K$.

The temperature dependence of the magnetization $M(T)$ of the $Ni_{45}Mn_{35}In_{15}Co_5$ sample measured on warming (red open circles) and cooling (blue filled circles) in $5\ mT$ field is shown in fig. 4.26(b). The sample is ferromagnetic in the austenite phase between $T_C^A = 393\ K$ and $M_s = 289\ K$, than on cooling the magnetization drops as the amount of the non-FM martensite increases. Below $M_f = 242\ K$ magnetization is close to zero, and the magnetization rises on further cooling towards $5\ K$. On warming the magnetization rises from nearly zero, exhibiting the local maximum at $\approx 50\ K$ and then dropping close to zero again. At about $200\ K$ magnetization slowly rises again, and at $A_s = 255\ K$ it abruptly increases as the FM austenite phase grows. Above $A_f = 306\ K$ slope decreases and magnetization increases up to Curie temperature $T_C^A = 393\ K$, and then drops.

In fig. 4.26(c) the temperature dependence of the flipping ratio R_F (see section 3.5.2) of the $Ni_{45}Mn_{35}In_{15}Co_5$ sample is shown. When the sample is cooled from $500\ K$ $R_F(T)$ is $\approx$ 23 and drops to 1 as the sample undergoes paramagnetic-to-ferromagnetic transition at $T_C^A = 393\ K$, and the neutron beam depolarizes due to the randomly oriented ferromagnetic domains. On further cooling R_F equals 1 until $\approx 250\ K$ and then slowly rises as the net magnetization decreases with growth of the non-FM martensite. However, R_F is still close to 1 at $M_f = 242\ K$ and rises up to 4 only at $160\ K$ and remains constant down to $3.5\ K$. On warming R_F slightly rises from 3.4 at $3.5\ K$ to 4 at $240\ K$ and then slightly decreases. At $A_s = 255\ K$ the slope increases, and R_F drops to 1 at $279\ K$ as net magnetization rises with the austenite growth. On further warming R_F equals 1 up to $405\ K$, and then abruptly rises to 23. We relate the difference between the cooling and warming branches close to Curie temperature T_C^A to the technical issues of the sample temperature measurement above $T > 300\ K$.

The flipping ratio in the ferromagnetic austenite state equals approximately $\approx$ 23, while in the martensitic state its value is around 4. The value is not completely regained because of the magnetic ordering in the martensitic state, which appears to be a complex mixture of FM and AFM phases. We show the field dependence of the magnetization $M(H)$ at different temperatures in fig. 4.27. The sample was warmed from $5\ K$ to $280\ K$, and the magnetization was measured on applying and removing of the field at chosen temperatures. Thus, at $5\ K$ (green line) the magnetization exhibits hysteresis and saturates at $1.5\ T$. On further warming, at $150\ K$ the magnetization shows the linear paramagnetic behavior,which is the same on both increasing and decreasing field. At $250\ K$, slightly below $A_s = 255\ K$, it shows linear behavior up to $3.8\ T$ and then the slope increases. On decreasing field from $5\ T$ magnetization exhibits linear behavior with higher slope than on increasing field. The exhibited behavior arises because of the field-induced growth of the austenite phase. At $275\ K$ and $280\ K$ (below $A_f = 306\ K$) this behavior is more pronounced.

In fig. 4.28(a) the q dependence of the scattering cross sections is shown for the $Ni_{45}Mn_{35}In_{15}Co_5$ sample measured at $500\ K$ and $3.5\ K$. The high temperature spectra represent separated nuclear and magnetic scattering contributions, while the low temperature spectrum represents the total scattering shifted upwards by +1 unit for clarity. Reflections in the spectra for HT phase are indexed with horizontal labels, and LT - with vertical ones, respectively. At high temperatures the $Ni_{45}Mn_{35}In_{15}Co_5$ sample resides in the cubic $L2_1$ austenite phase with the lattice parameter $\approx 6.087\ \mathring{A}$. The magnetic cross section in fig. 4.28(b) measured at $500\ K$ shows substantial forward scattering at low q values in paramagnetic state ($T_C^A = 393\ K$). The hump of the diffuse scattering between $1.2 \leq q \leq 2.6\ \mathring{A}^{-1}$ can be related to the presence of weak AFM correlations even at high temperatures in the austenite phase [28]. A drop at $q \approx 2.1\ \mathring{A}^{-1}$ corresponds to the separation error of the nuclear and magnetic contributions around (200) Bragg peak.

According to the low temperature X-ray diffraction measurements performed on the same sample [103], low temperature martensite phase is 7M orthorhombic lattice. However, the neutron scattering spectrum measured at $3.5\ K$ shows orthorhombic structure $Pmmm.$ with lattice parameters $a = 4.21(8)$, $b = 30.35(3)$, $c = 6.03(9)$, resulting in following relation between the lattice parameters in martensite and austenite lattices: $a_M \approx \frac{1}{\sqrt{2}}a_A$, $b_M \approx \frac{7}{\sqrt{2}}a_A$ and $c_M \approx a_A$

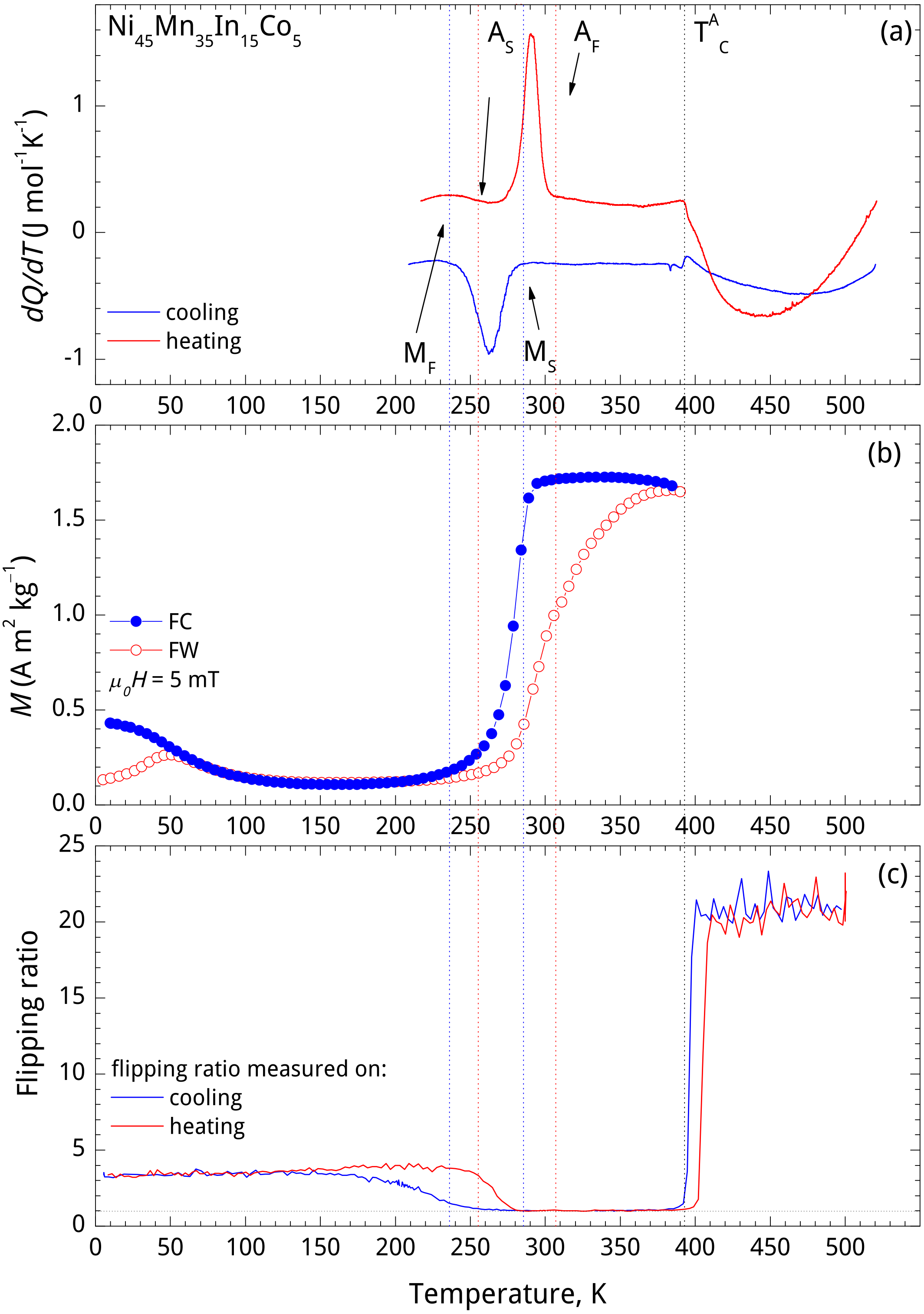

Figure 4.26: Characterization of the $Ni_{45}Mn_{35}In_{15}Co_5$ sample for polarization analysis experiments. Temperature dependence of calorimetric curves $dQ/dT(T)$ (a), magnetization $M(T)$ (b) and flipping ratio $R_F(T)$ (c) on warming and cooling. The dashed lines reference the temperatures of start and end of the structural transition on warming and cooling and magnetic order-disorder transformation defined by DSC.

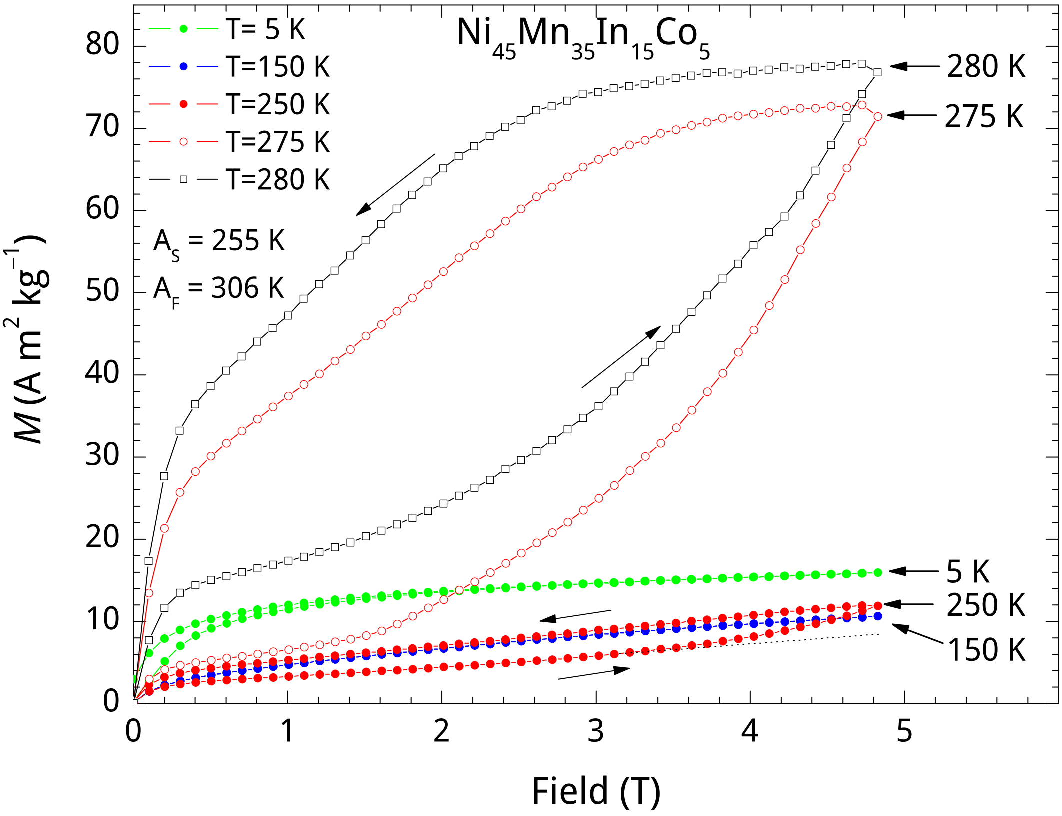

Figure 4.27: Field dependence of magnetization $M(H)$ of the $Ni_{45}Mn_{35}In_{15}Co_5$ sample plotted for selected temperatures. Austenite start A_s and finish A_f temperatures are determined by DSC (see fig. 4.26)

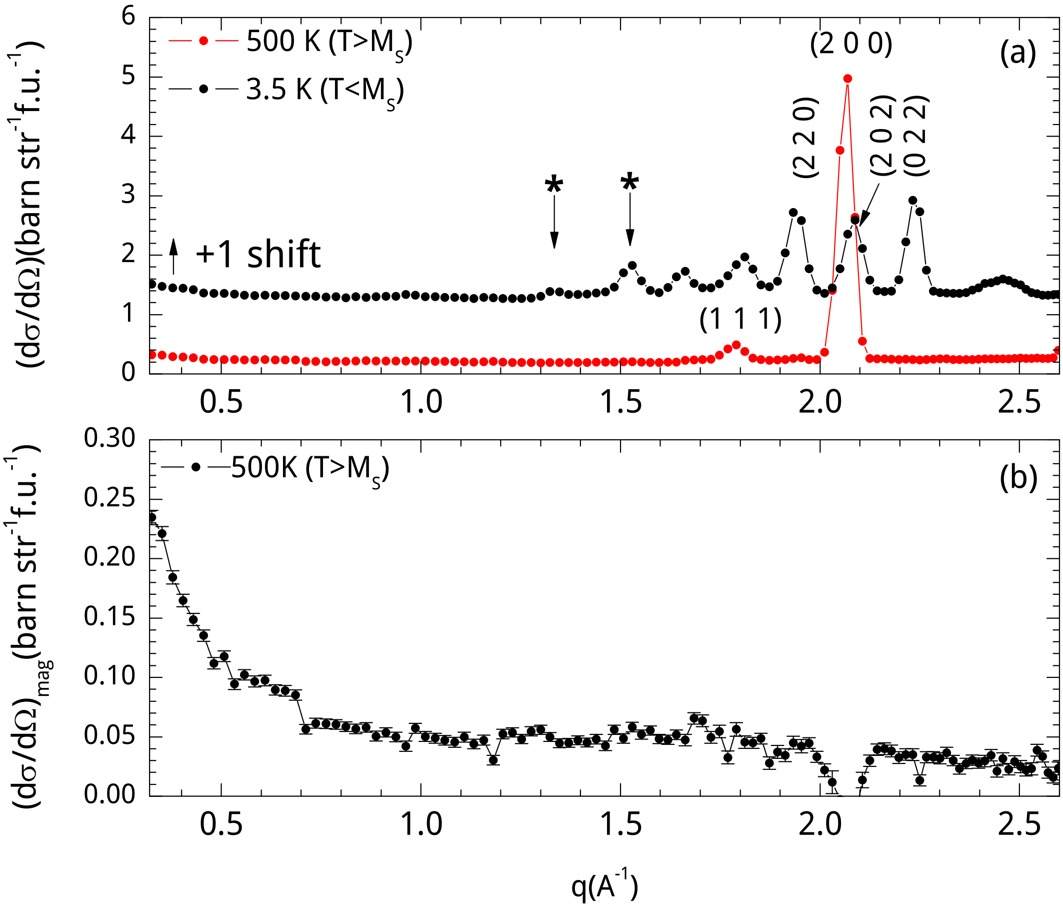

Figure 4.28: (a) The q dependence of the nuclear-coherent cross sections in the austenitic ($500\ K$) and the total scattering in the martensitic ($3.5\ K$) states ($M_s = 289\ K$) of $Ni_{45}Mn_{35}In_{15}Co_5$. The nuclear cross section plotted in the range $1.2 \leq q \leq 2.6\ \AA^{-1}$. No reflections are found at lower q in either spectra. The data for $3.5\ K$ are shifted by +1 for clarity.
(b) The magnetic cross section at $500\ K$ ($T_C \approx 400\ K$). A characteristic shoulder in range $1.2 \leq q \leq 2.0\ \AA^{-1}$ indicates the presence of weak AFM interactions in austenite state. A drop at $q \approx 2.1\ \AA^{-1}$ corresponds to the separation error of the nuclear and magnetic contributions around (200) Bragg peak.

4.5 Field dependent neutron diffraction study of $Ni_{50}Mn_{33}In_{17}$

We performed the field dependent neutron diffraction measurements on the sintered powder $Ni_{50.42}Mn_{32.96}In_{16.63}$ sample using the D2B neutron diffractometer equipped with low temperature cryostat and superconducting magnet. An initially melted ingot was ground with a ball miller using ZrO_2 balls. Then, $8\ g$ powder sample was annealed at $1073\ K$ for 4 weeks. As a result powder was sintered, so the reorientation of powder particles on the application of the field could be excluded. Prior to the neutron diffraction measurements we performed temperature dependence of the magnetization measurements along with X-ray diffraction analysis at room temperature. The X-ray diffraction spectrum is shown in fig. 4.29(a). The pattern consists of the reflection peaks belonging to the austenite Heusler $L2_1$ cubic phase (Bragg peaks are marked with higher row of and indexed with horizontal labels) and reflections belonging to the ZrO_2 tetragonal lattice. The residuals from milling balls are the source of trace ZrO_2 in the sample. These additional peaks from ZrO_2 are present on all diffraction patterns shown in this section. We estimate the amount of residual ZrO_2 to be less than 1%.

In fig. 4.29(b), we show the temperature dependence of the magnetization for the sample used in this experiment. The dotted lines represent behavior of the magnetization under ZFC, FC and FW measurements in $5\ mT$ and $5\ T$ fields, while bright colors represent actual path of the magnetization during the experiment. The labels mark the state of the sample where we performed the diffraction measurement. According to the magnetization measurements this sample undergoes magnetic order-disorder transition in the austenitic state at $T_C^A = 293\ K$. On cooling in $5\ mT$ magnetic field it starts transforming from the austenitic to the martensitic phase at $M_s = 210\ K$, while in $5\ T$ field transformation temperature is $190\ K$. Thus with the application of the magnetic field M_s decreases by $4\ K$ per Tesla.

Initially, the as-sintered sample resided at $280\ K$ in zero field. We show the neutron diffraction spectrum of this sample in this state in fig. 4.30(a). The spectrum consists of two patterns: one belongs to the tetragonal ZrO_2 lattice and indexed by the lower row of reflections and the other one belonging to the cubic austenite lattice and indexed by the higher row of reflections (corresponding peaks are labeled by horizontal labels). At this temperature the austenite phase is $L2_1$ type with lattice parameter $a = 6.0111\ \AA^{-1}$.

Afterwards, the sample was cooled in zero field (thus following ZFC path of the magnetization in fig. 4.29(a)), below the structural transformation M_s temperature to $100\ K$, so the sample resides in the fully-transformed martensitic state. The low temperature martensite phase is the product of tetragonal distortion of parent cubic phase. Therefore, the reflections from the cubic lattice split into the several new reflections in the product phase, and the resulting low-temperature diffraction pattern consists of more diffraction peaks than the high-temperature one. In fig. 4.30(b) we show the neutron diffraction pattern corresponding to this state. The pattern is indexed using two phases: residiual ZrO_2 (the lower row of reflections) and 3-fold monoclinic martensite phase with space group $P2/m$ and lattice parameters $a = 4.4137\ \AA$, $b = 5.6548\ \AA$, $c = 13.0351\ \AA$ and $\beta = 86.73^{\circ}$.

In fig. 4.31(a) we show the diffraction pattern of the powder sample after the application of $5\,T$ field at $100\ K$. Application of the field to zero-field cooled sample at this temperature does not affect lattice symmetry, but leads to the changes in lattice parameters: $a = 4.4150\ \AA$, $b = 5.6540\ \AA$, $c = 13.0331\ \AA$ and $\beta = 86.73^{\circ}$. Additionally, in fig. 4.31(b) and (c) we show comparison of the spectra measured at $5\ T$ and $0\ T$ along with the subtraction of observed intensities spectra $\Delta Y(q) = Y^{5\ T}_{100\ K}(q) - Y^{0\ T}_{100\ K}(q)$ in range between $1\ \AA^{-1} < q < 4\ \AA^{-1}$ and $4\ \AA^{-1} < q < 7\ \AA^{-1}$, respectively. According to this comparison, no new Bragg reflections emerge on the diffraction spectrum after applying the magnetic field. However, intensity of the certain reflections, belonging to the martensite phase changes after the applying of the magnetic field. These reflections are marked by black arrows in fig. 4.31(b) and (c). The intensities of the Bragg reflections at 1.8, 2.2, 2.8, 2,9, 3.0 and 4.4 $\mathring{A}^{-1}$ increase in $5\ T$ field. While the intensities of the Bragg reflections at 3.6 and 5.3 $\mathring{A}^{-1}$ do not change, and the kinks on ΔY_{obs} graph occur due to slight difference in the peak positions (and thus, differences in lattice parameters) in each of the states.

We then warm up the sample above A_f temperature from $100\ K$ to $280\ K$ in $5\ T$ field. In fig. 4.32(a) we show the diffraction pattern measured in this state. The diffraction pattern consists of two phases: tetragonal ZrO_2 and cubic $L2_1$ austenite with lattice parameter $a = 6.0110\ \mathring{A}$. In fig. 4.32(b) and (c) we show the comparison of diffractions patterns measured at $280\ K$ in two different states: FW in $5\ T$ and as-sintered in zero-field along with the differential spectrum. Horizontal labels index Bragg reflections from cubic lattice. No new Bragg reflections are found on the spectrum measured in-field, and intensities of all reflections from cubic phase are higher in $5\ T$ field, than in zero-field.

After this measurement, the sample was cooled again below M_s temperature down to $100\ K$ in $5\ T$ field. In fig. 4.33(a) we show the diffraction pattern measured in this state. The diffraction pattern consists of the two phases: tetragonal ZrO_2 and cubic $L2_1$ austenite with lattice parameters $a = 4.4155\ \mathring{A}$, $b = 5.6508\ \mathring{A}$, $c = 13.0282\ \mathring{A}$ and $\beta = 86.73^{\circ}$. In fig. 4.33(b) and (c) we show the comparison of diffractions patterns measured at $100\ K$ in two different states: FC in $5\ T$ and zero-field cooled in zero field along with the differential spectrum. While both spectra bear the same reflections, the intensities of some of these reflections differ (marked by black arrows on the graph). The intensities of the Bragg reflections at 2.09 ,4.5 and 4.93 $\mathring{A}^{-1}$ are higher in FC state, while at 1.97, 2.22 and 4.45 $\mathring{A}^{-1}$ intensities are higher in ZFC state.

As the last step, we performed the diffraction measurement in FC state after removing the field. In fig. 4.34(a) we show the diffraction pattern measured at this state. The removal of the field does not alter phase symmetry, however, the lattice parameters do change: $a = 4.4163\ \mathring{A}$, $b = 5.6482\ \mathring{A}$, $c = 13.0368\ \mathring{A}$ and $\beta = 86.73^{\circ}$. Additionally, in fig. 4.34(b) and (c) we show comparison of the spectra measured at $5\ T$ nad $0\ T$ along with the subtraction of observed intensities spectra $\Delta Y(q) = Y^{5\ T}_{100\ K}(q) - Y^{0\ T}_{100\ K}(q)$ in range between $1\ \mathring{A}^{-1} < q < 4\ \mathring{A}^{-1}$ and $4\ \mathring{A}^{-1} < q < 7\ \mathring{A}^{-1}$, respectively. According to this comparison, no new Bragg reflections are present on the diffraction spectrum after heating and cooling in the magnetic field. However, there is a difference in the intensities of the Bragg reflections between these two spectra. The intensities of the Bragg reflections at 2.9 and 4.88 $\mathring{A}^{-1}$ are higher in FC state, while the intensities of the Bragg reflection at 3.05 $\mathring{A}^{-1}$ are lower in this state. The kinks on $\Delta Y_{obs}(q)$ dependence in range of 1.8 - 2.3 $\mathring{A}^{-1}$ and 2.8 - 3.2 $\mathring{A}^{-1}$ are related to differences in the Bragg reflection positions.

Additionally, we performed reference neutron diffraction measurements on the sintered powder sample in the sample environment without the superconducting magnet. In fig. 4.35(a) we show the diffraction pattern of the as-sintered sample measured above Curie temperature of the austenite phase T_C^A at $320\ K$ in $0\ T$. The diffraction pattern consists of the reflections from the residual tetragonal ZrO_2 phase, and the cubic austenite with lattice parameter $a = 6.0133\ \mathring{A}$.

In fig. 4.35(b) we show the diffraction pattern of zero-field cooled sample measured below M_s at $100\ K$ in $0\ T$. The diffraction pattern consists of the reflections from the residual tetragonal ZrO_2 phase, and the cubic austenite with lattice parameter $a = 4.4223\ \mathring{A}$, $b = 5.6553\ \mathring{A}$, $c = 13.028\ \mathring{A}$ and $\beta = 86.80^{\circ}$.

physical state			lattice parameters				cell volume	
T(K)	Field (T)	pre-history	a (Å)	b(Å)	c(Å)	β ()	(Å^3)	χ^2
$\star$ 320	0	as-sintered	6.0133	6.0133	6.0133	90.00	217.44	4.92
$\star$ 100	0	ZFC	4.4223	5.6553	13.028	86.80	325.32	13.2
$\times$ 294	0	as-sintered	6.0059	6.0059	6.0059	90.00	216.64	1.92
280	0	as-sintered	6.0111	6.0111	6.0111	90.00	217.20	0.64
100	0	ZFC	4.4137	5.6548	13.0351	86.73	324.82	3.08
100	5	ZFC	4.4150	5.6540	13.0331	86.73	324.80	0.34
280	5	FW	6.0110	6.0110	6.0110	90.00	217.19	0.65
100	5	FC	4.4155	5.6508	13.0282	86.73	324.54	0.34
100	0	FC	4.4163	5.6482	13.0368	86.73	324.67	2.95

Table 4.2: Lattice parameters of the $Ni_{50.42}Mn_{32.96}In_{16.63}$ sample measured under differend conditions (fields and temperatures) after certain state (3rd column). Star sign marks the data obtained from the neutron diffraction measurements in the environment without superconducting magnet. X sign marks the data obtained from the X-ray diffraction measurement. The rest data is obtained from the neutron diffraction measurements performed in the environment with the superconducting magnet.
χ^2 is a quality of the fit parameter (less is better).

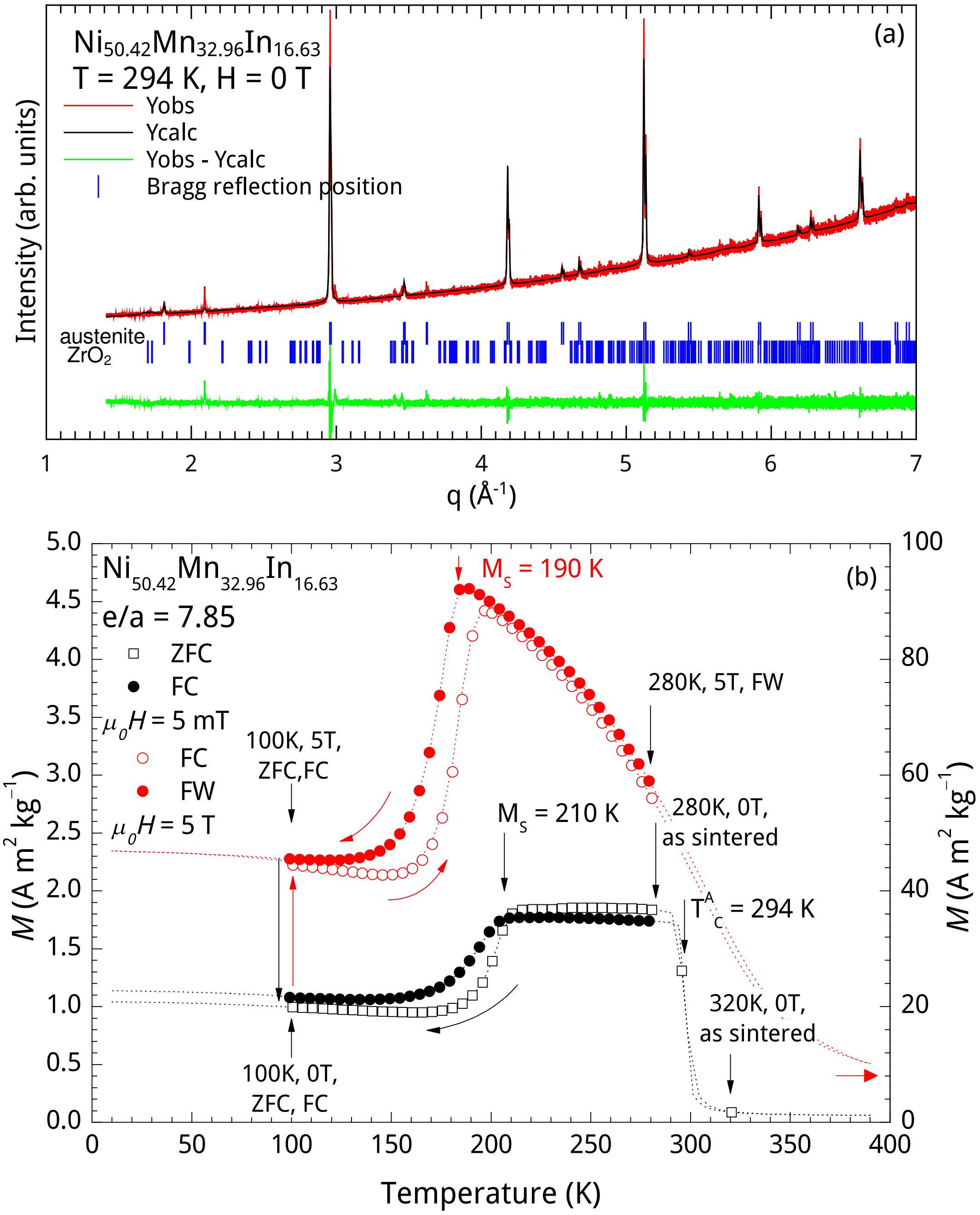

Figure 4.29: (a) X-ray diffraction pattern for the as-sintered powder $Ni_{50.42}Mn_{32.96}In_{16.63}$ sample at $294\ K$ in zero field with calculated and substracted diffraction profiles. Higher Bragg reflections belong to Heusler lattice, lower Bragg reflections to ZrO_2. (b) Temperature dependence of magnetization measured in $5\ mT$ (black color) and $5\ T$ (red color) under ZFC (open squares), FC (filled circles) and FW (open circles) protocols of $Ni_{50.42}Mn_{32.96}In_{16.63}$ sample. Labels relate certain states on magnetization curves with corresponding diffraction patterns.

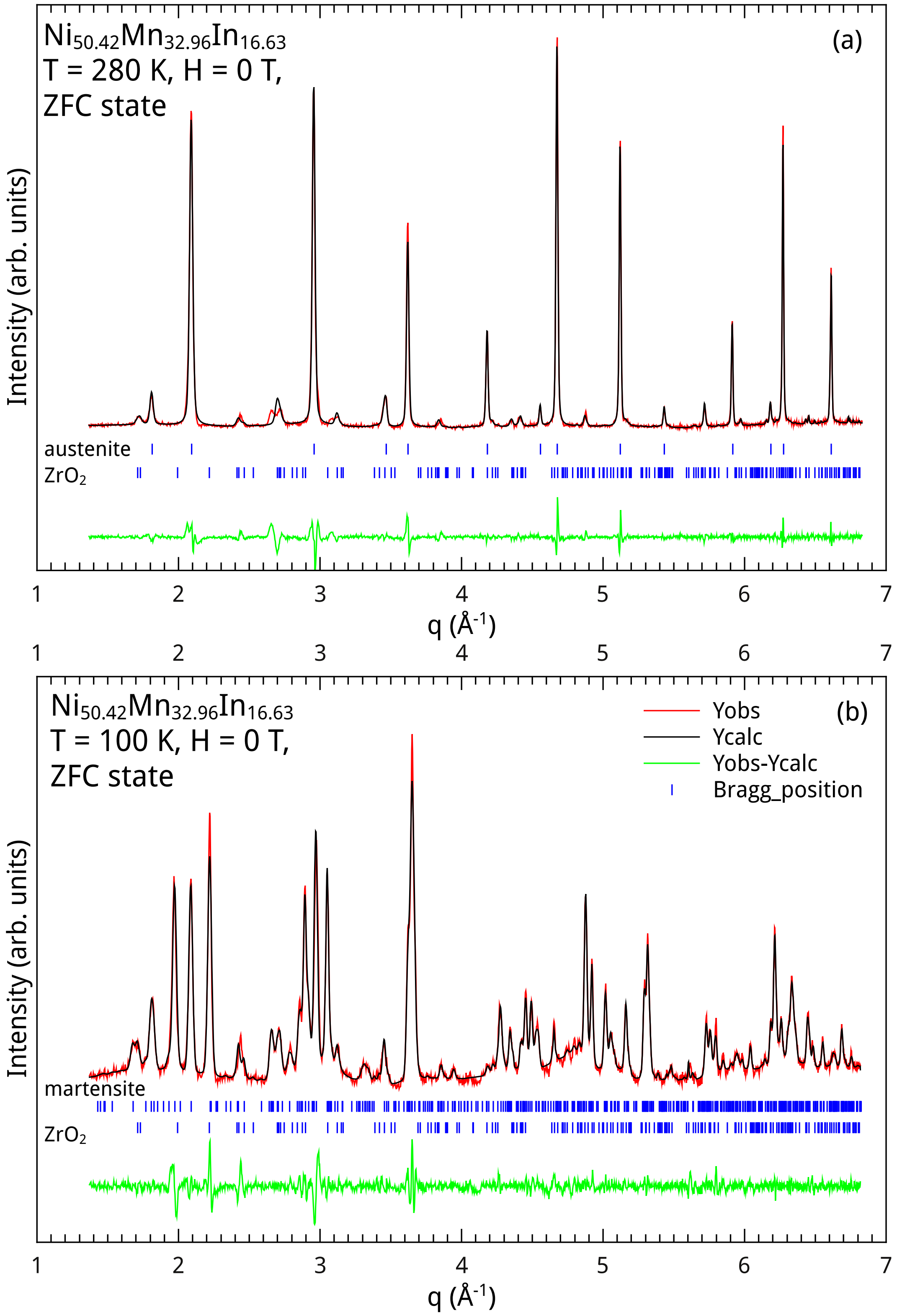

Figure 4.30: Neutron diffraction pattern for the $Ni_{50.42}Mn_{32.96}In_{16.63}$ sample with calculated and substracted profiles measured in the as-sintered austenite state at $280\ K$ (a) and in the martensite state at $100\ K$ after ZFC protocol (b) at zero field. Higher Bragg reflections belong to Heusler lattice, lower Bragg reflections to ZrO_2.

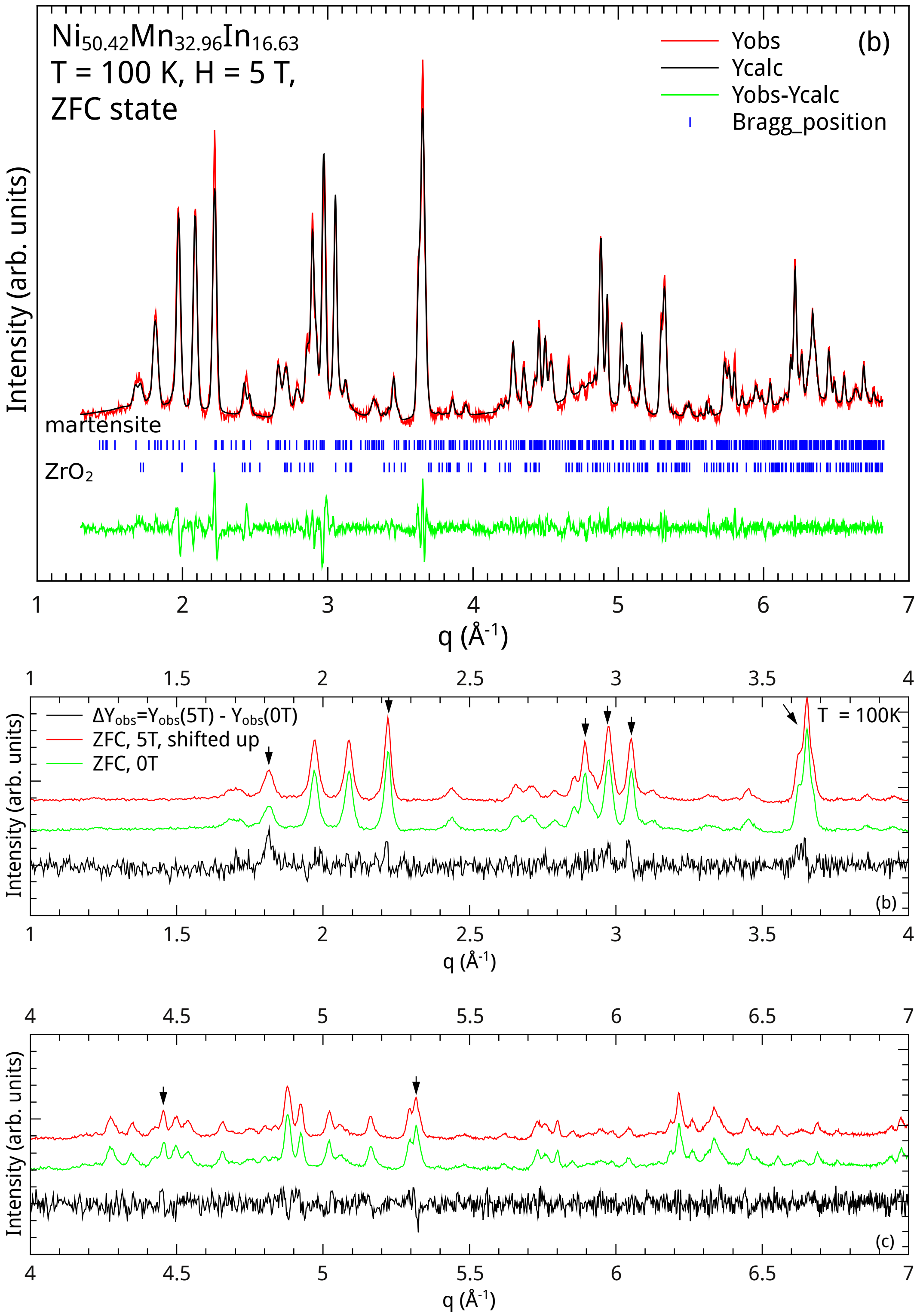

Figure 4.31: (a) Neutron diffraction pattern for the $Ni_{50.42}Mn_{32.96}In_{16.63}$ sample with calculated and substracted profiles measured in the martensite state at $100\ K$ in $5\ T$ after cooling in zero field. Higher Bragg reflections belong to Heusler lattice, lower Bragg reflections to ZrO_2.
Comparison of the neutron diffraction patterns in range between $1\ \AA^{-1} < q < 4\ \AA^{-1}$ (b) and $4\ \AA^{-1} < q < 7\ \AA^{-1}$ (c) for the same sample measured in $5\ T$ (shifted up for clarity) and $0\ T$ fields at $100\ K$ after cooling in zero field, along with difference between spectral intensities $\Delta Y(q) = Y^{5\ T}_{100\ K}(q) - Y^{0\ T}_{100\ K}(q)$.

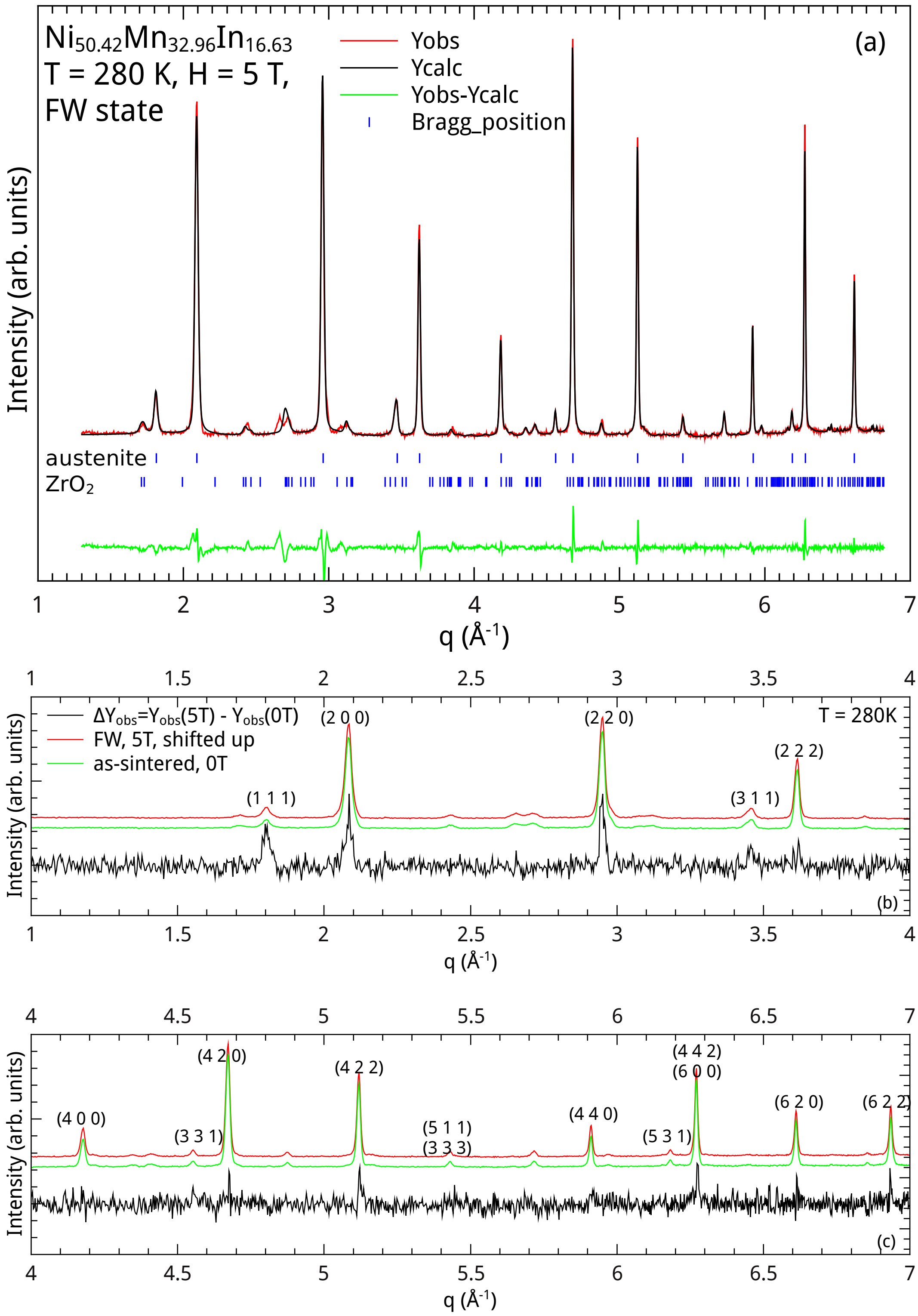

Figure 4.32: (a) Neutron diffraction pattern for the $Ni_{50.42}Mn_{32.96}In_{16.63}$ sample with calculated and substracted profiles measured in the martensite state at $280\ K$ in $5\ T$ after heating in $5\ T$ field. Higher Bragg reflections belong to Heusler lattice, lower Bragg reflections to ZrO_2.
Comparison of the neutron diffraction patterns in range between $1\ \AA^{-1} < q < 4\ \AA^{-1}$ (b) and $4\ \AA^{-1} < q < 7\ \AA^{-1}$ (c) for the same sample measured in $5\ T$ (FW protocol, shifted up for clarity) and $0\ T$ (as-sintered) fields at $280\ K$, along with difference between spectral intensities $\Delta Y(q) = Y^{5\ T}_{280\ K}(q) - Y^{0\ T}_{280\ K}(q)$.

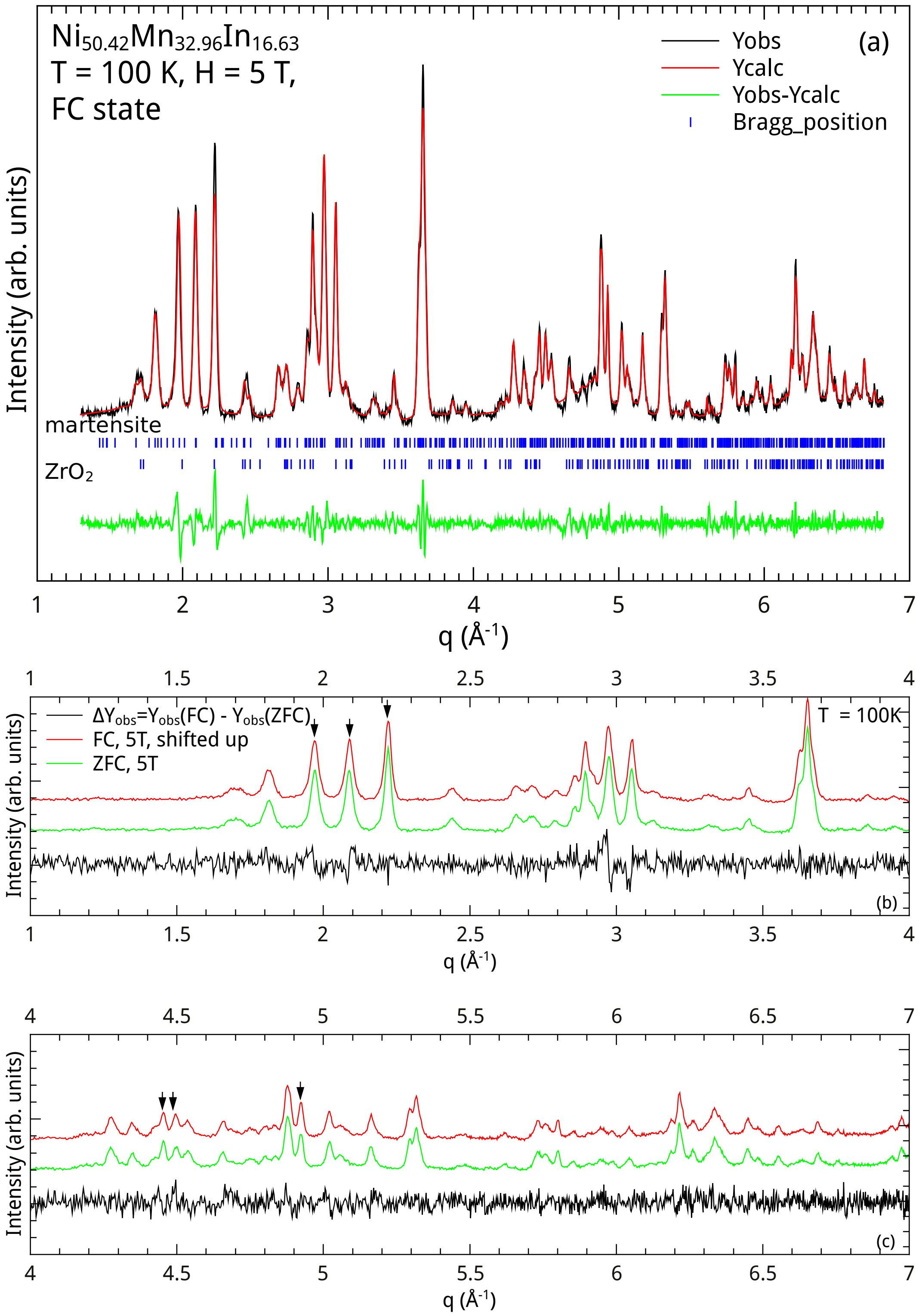

Figure 4.33: (a) Neutron diffraction pattern for the $Ni_{50.42}Mn_{32.96}In_{16.63}$ sample with calculated and substracted profiles measured in the martensite state at $100\ K$ in $5\ T$ after cooling in $5\ T$ field. Higher Bragg reflections belong to Heusler lattice, lower Bragg reflections to ZrO_2.
Comparison of the neutron diffraction patterns in range between $1\ \mathring{A}^{-1} < q < 4\ \mathring{A}^{-1}$ (b) and $4\ \mathring{A}^{-1} < q < 7\ \mathring{A}^{-1}$ (c) for the same sample measured in $5\ T$ after FC protocol (shifted up for clarity) and ZFC protocol at $100\ K$, along with difference between spectral intensities $\Delta Y(q) = Y^{FC}_{100\ K}(q) - Y^{ZFC}_{100\ K}(q)$.

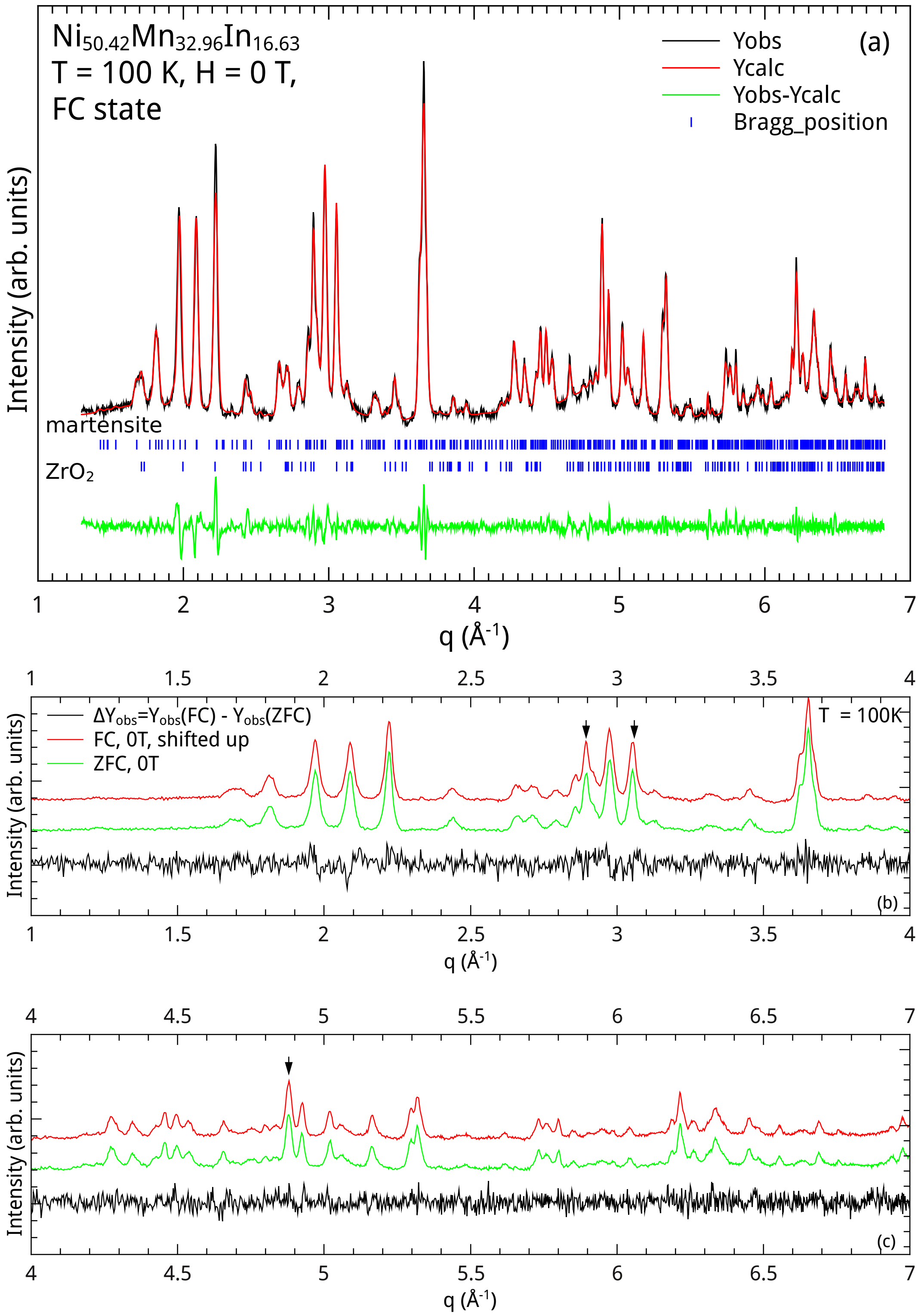

Figure 4.34: (a) Neutron diffraction pattern for the $Ni_{50.42}Mn_{32.96}In_{16.63}$ sample with calculated and substracted profiles measured in the martensite state at $100\ K$ in $0\ T$ after cooling in $5\ T$ field. Higher Bragg reflections belong to Heusler lattice, lower Bragg reflections to ZrO_2.
Comparison of the neutron diffraction patterns in range between $1\ \mathring{A}^{-1} < q < 4\ \mathring{A}^{-1}$ (b) and $4\ \mathring{A}^{-1} < q < 7\ \mathring{A}^{-1}$ (c) for the same sample measured in zero field after FC protocol, (shifted up for clarity) and ZFC protocol at $100\ K$, along with difference between spectral intensities $\Delta Y(q) = Y^{FC}_{100\ K}(q) - Y^{ZFC}_{100\ K}(q)$.

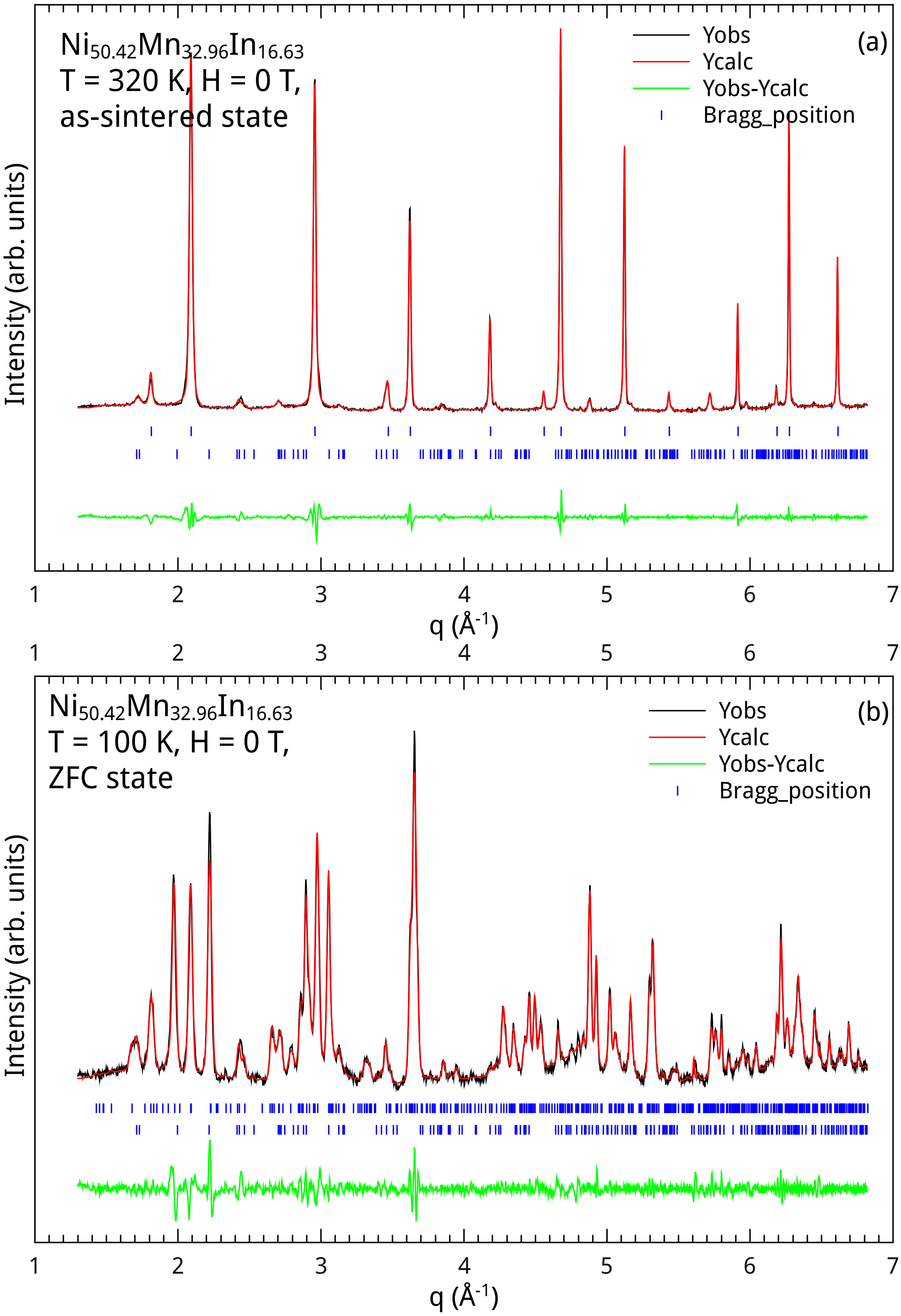

Figure 4.35: Neutron diffraction pattern for the $Ni_{50.42}Mn_{32.96}In_{16.63}$ sample with calculated and substracted profiles measured in the as-sintered austenite state at $320\ K$ (a) and in the martensite state at $100\ K$ in zero field after ZFC protocol (b). Higher Bragg reflections belong to Heusler lattice, lower Bragg reflections to ZrO_2. Both measurements were performed in the cryostat environment without the superconducting magnet.

5 Discussion

> There are always enough facts to build a complete theory, only fantasy is lacking.
> D. Blokhintsev, theoretical physicist

5.1 Effect of stoichiometry on magnetic interactions in Ni-Mn-Ga and Ni-Mn-Sn alloys

As we have shown above, the phenomena exhibited by Heusler alloys in the martensite state such as exchange bias effects and magnetic glass properties, such as the splitting between ZFC and FC magnetization curves, can be explained with the hypothesis that `Mn` atoms, bearing the major magnetic moment in the cell, couple together antiferromagnetically at short range in addition to their ferromagnetic coupling (see section 2.3.3). For example, AF interactions are observed in stoichiometric Ni_2MnAl, which features a cone spiral AF magnetic ordering of Mn moments, while NiMn is a collinear antiferromagnet. There are a series of experiments giving evidence for this hypothesis. We list below the used methods for observing various magnetic interactions:

Mössbauer spectra no AF correlations are found below M_s and above T_C^A in ^{57}Fe-doped martensitic Heuslers $Ni_{50}Mn_{36.5}{}^{57}Fe_{0.5}Sn_{13}$ and $Ni_{50}Mn_{34.3}{}^{57}Fe_{0.5}In_{15.2}$.

magnetization measurements: indirect signs of non-FM coupling;

neutron diffraction: indirect signs of short range or incommensurate AF in $Ni_{50}Mn_{36}Sn_{14}$, $Ni_{50}Mn_{37}Sb_{13}$ and $Ni_{46}Mn_{41}In_{13}$

neutron polarization analysis: presence of AF correlations and both AF and FM correlations in magnetically disordered martensite and austenite phases, respectively, in $Ni_{50}Mn_{37}Sn_{13}$ and $Ni_{50}Mn_{40}Sb_{10}$.

FMR: presence both AF and FM resonance lines in magnetically ordered martensite phase in $Ni_{1-x-y}Mn_xGa_y$, $Ni_{49.1}Mn_{35.4}In_{15.5}$, $Ni_{49.9}Mn_{37.0}Sn_{13.1}$

As seen from the list, the only method that does not show the presence of AF correlations in the martensite phase of Ni-Mn-based Heusler alloys is Mössbauer spectroscopy, while the experimental results obtained by other methods lead to the conclusion that AF correlations are present in the martensite phase as well as in the austenite phase.

Mössbauer cannot distinguish PM from AF when AF is in the form of a short range correlation as in this case the resoloution is not high enough to distinguish the very narrowly spaced 6-lines from a single peak.

It is worth noting that any one of these methods is not sufficient alone to provide information on all aspects of the occurring magnetic interactions; e.g., ferromagnetic resonance gives information on magnetically ordered states, while neutron polarization can provide information on the nature of magnetic short range correlations. This means that FMR experiments can be used to determine the nature of long-range magnetic coupling in martensitic Heuslers in magnetically ordered states, while neutron polarization analysis can be applied for martensitic Heuslers only in temperature-ranges where no long range ordering may occur, i.e. in the range $T_C^M < T < M_s$ and above T_C^A. Alternatively, it can be used just above T_M^C in the case when the martensitic transition occurs between paramagnetic austen-

composition	martensite phase $< T_C^M$	$> T_C^M$	austenite phase $< T_C^A$	$> T_C^A$	e/a	refs.
$Ni_{50}Mn_{40}Sb_{10}$		AF		AF+FM	8.3	[28]
$Ni_{50}Mn_{37}Sn_{13}$	AF+FM	AF, AF+FM	FM	AF+FM, PM	8.11	[28, 78]
$Ni_{50}Mn_{37}In_{13}$	AF+FM	AF	FM	PM	7.98	[78]
$Ni_{50}Mn_{36}Sn_{14}$	AF+FM	▨	FM		8.08	[68]
$Ni_{50}Mn_{37}Sb_{13}$	AF+FM	▨	FM		8.24	[66]
$Ni_{46}Mn_{41}In_{13}$	AF+FM	AF+FM	FM		7.86	[67]
$Ni_{50}Mn_{36.5}{}^{57}Fe_{0.5}Sn_{13}$		PM		PM	8.12	[26]
$Ni_{50}Mn_{34.3}{}^{57}Fe_{0.5}In_{15.2}$		PM		PM	7.9	[27]
$Ni_{45}Co_{5}Mn_{35}In_{15}$	AF+FM	AF+FM		AF+FM	7.85	⋆
$Ni_{50.42}Mn_{32.96}In_{16.63}$	AF+FM	▨	FM		7.85	⋆
$Ni_{49.37}Mn_{40.31}Sn_{9.92}$	AF+FM	FM	▨	▨	8.16	⋆
$Ni_{49.38}Mn_{34.80}Sn_{15.82}$	AF+FM	▨	FM	AF+FM, PM	8.01	⋆
$Ni_{54.65}Mn_{19.29}Sn_{26.06}$	▨	▨	FM	FM, PM	7.86	⋆
$Ni_{49.71}Mn_{23.98}Sn_{26.31}$	▨	▨	FM	FM, PM	7.70	⋆
$Ni_{49.97}Mn_{30.35}Ga_{19.68}$	AF+FM	AF+FM, PM	▨	AF+FM	7.71	⋆
$Ni_{49.95}Mn_{24.67}Ga_{25.38}$	AF+FM	▨	FM	AF+FM, PM	7.48	⋆
$Ni_{45.32}Mn_{30.33}Ga_{24.35}$	AF+FM	▨	FM	AF+FM, PM	7.38	⋆
$Ni_{49.06}Mn_{20.28}Ga_{30.66}$	▨	▨	FM	PM	7.25	⋆

Table 5.1: List of the samples with determined magnetic states in martensite and austenite phase below and above temperatures of magnetic ordering in each of the phases (T_C^M,T_C^A,respectively). Colored labels denote experimental data obtained by Mössbauer spectroscopy, ferromagnetic resonance, neutron diffraction and neutron polarization experiments. Filled cell means that this phase was not observed in the sample. References relate to the published data, star sign ⋆ marks the original research, made in this thesis.

ite state and martensitic state with low magnetization (see fig. 2.10(c) or [28]). Although, FMR can be employed in the PM phase, neutron polarization analysis gives more detailed information on, e.g., FM correlations in Fe above the Curie temperature fig. 3.7. Therefore, these methods provide complementary information.

In table 5.1 we give a list of materials for which the magnetic couplings in the austenite and martensite phases were determined by either method. Colored labels denote experimental data obtained by Mössbauer spectroscopy, ferromagnetic resonance, neutron diffraction and neutron polarization experiments. Filled cell means that this phase was not observed in the sample. The data obtained from published results is located in the upper part of the table, while the data shown in this thesis is located in the lower part below the double line.

We first discuss the data given in the references in the table. Except for $Ni_{50}Mn_{37}Sn_{13}$, which was studied with the two techniques, the other samples were studied using either of the methods. This is insufficient for studying the development of magnetic ordering with temperature. Additionally, the evolution of magnetic structure with the compositional change is of fundamental interest. Because all of these measurements were performed on martensitic samples, there is no direct evidence of the absence of AF correlations in non-martensitic Heuslers obtained by these methods.

Therefore, to go further in these studies, we prepared two series of the Ni-Mn-Sn and Ni-Mn-Ga samples with over stoichiometric and under stoichiometric Mn composition with respect to the $Ni_{50}Mn_{25}Z_{25}$ compositions. These are termed as Mn-rich and Mn-poor in the discussion below. In the Ga-containing series, the Mn-poor alloy $Ni_{49.06}Mn_{20.28}Ga_{30.66}$ does not transform martensitically, while at a composition close to the composition of the stoichiometric compound $Ni_{49.95}Mn_{24.67}Ga_{25.38}$, off-stoichiometric Mn-rich $Ni_{49.97}Mn_{30.35}Ga_{19.68}$, and Mn-rich and Ni-poor $Ni_{45.32}Mn_{30.33}Ga_{24.35}$ undergo martensitic transitions. In the Sn-containing series, Mn-rich $Ni_{49.38}Mn_{34.80}Sn_{15.82}$ and $Ni_{49.37}Mn_{40.31}Sn_{9.92}$ exhibit martensitic transitions, while the alloy with composition close to the 50-25-25 stoichiometry, $Ni_{49.71}Mn_{23.98}Sn_{26.31}$, and Ni-rich Mn-poor $Ni_{54.65}Mn_{19.29}Sn_{26.06}$ do not.

Most of the investigated martensitic samples do not exhibit a magnetic transition in the martensite state except for $Ni_{49.37}Mn_{40.31}Sn_{9.92}$ and $Ni_{49.97}Mn_{30.35}Ga_{19.68}$, which have a region with low magnetization in the martensitic state. These samples undergo structural transformation from a magnetically short-range correlated martensite to paramagnetic austenite.

According to ferromagnetic resonance experiments, these samples in the austenite phase are ferromagnetic below T_C^A, and paramagnetic above it. However, neutron polarization analysis shows that in non-transforming Ni-Mn-based Heuslers only FM correlations are present above T_C^A. In the martensitic alloys, both FM and AF correlations are observed.

The ferromagnetic resonance experiments show the presence of both AF and FM lines in the resonance spectra below T_C^M in the martensite state of the alloys. The two samples exhibiting magnetic transitions in the martensite state, $Ni_{49.37}Mn_{40.31}Sn_{9.92}$ and $Ni_{49.97}Mn_{30.35}Ga_{19.68}$ show different magnetic ordering above T_C^M, in the sense that while only FM lines are present in the resonance spectra of $Ni_{49.37}Mn_{40.31}Sn_{9.92}$ sample above T_C^M, $Ni_{49.97}Mn_{30.35}Ga_{19.68}$ is in the magnetically disordered state, according to FMR results. Additionally, neutron polarization experiments show AF and FM correlations in this state, just as in the austenite phase of this sample.

These results give evidence for the presence of AF interactions in martensitic Ni-Mn-based Heusler alloys with Ga and Sn. Supported by other experiments (see table 5.1), we conclude that the AF interactions are also present in alloys with In and Sb. Studying the compositional lines we show that AF interactions are inherent to transforming alloys, and they vanish if the alloy does not transform martensitically.

As shown in section 4.3.2 the q-dependence of the magnetic cross section exhibits diffuse scattering above $q(\AA^{-1}) > 1$ in paramagnetic austenite state of martensitic Heuslers (e.g. see fig. 4.20) indicating the presence of AF correlations. The diffuse nature of the scattering suggests that there is no ordering of the magnetic structure above T_C^A and there are AF interactions existing on a certain range of distances (about $\approx 1.2 - 2.0\ \AA^{-1}$ in q-range).

In the FMR experiments, martensitic samples exhibit AF resonance line in martensite phase, lying close to the isotropic value ω/γ. On increasing temperature towards A_s this line approaches ω/γ, looses intensity and dies out. This, again, means that the AF interactions are not strong enough to lead to long-range AF ordering. The AF correlations observed are due to the Mn-Mn interactions in the lattice. AF interactions occur just between pairs of Mn-Mn atoms close enough to couple antiferromagnetically with each other, if the distance is larger, they couple ferromagnetically, so the *long-range* AF ordering is not formed.

The cubic phase η of AF $NiMn$ has cubic *B2* structure with lattice parameter $a_{NiMn} = 2.98\ \AA$. Therefore, in $NiMn$ the are pairs Mn atoms with distances of 2.98 Å, 4.21 Å and 5.16 Åcorresponding to a_{NiMn}, $\sqrt{2}a_{NiMn}$ and $\sqrt{3}a_{NiMn}$, respectively. The closest Mn atoms couple antiferromagnetically. On doping $NiMn$ with a Z element (Z = Ga, In, Sn, Sb), while keeping Ni concentration constant at 50 at.%, the Z element will occupy some Mn positions, thus reducing the number of closest pairs of Mn atoms; e.g., in the cubic $L2_1$ (austenite) phase of $Ni_{50}Mn_{50-x}Z_x$ alloy, where $x < 25$ at.%, the Mn atoms form pairs with distances $\frac{a}{2}$, $\frac{\sqrt{2}a}{2}$ and $\frac{\sqrt{3}a}{2}$. Among these distances $\frac{\sqrt{2}a}{2}$ corresponds to the distance between Mn atoms occupying *4b* positions, and the other ones are the closest and the furthest distances between atoms in *4b* position and *4a* position. However, as the concentration of the doping element x rises, Mn pairs with distances $\frac{\sqrt{a}}{2}$ and $\frac{\sqrt{3a}}{2}$ become less, and in the stoichiometric case ($x = 25$ at.%), they do not exist. Finally, at $x \gtrsim 25\, at.\%$, the number of Mn pairs with distance $\frac{\sqrt{2}a}{2}$ start decreasing.

$NiMn$ undergoes a martensitic transition from the cubic η to the tetragonal η' phase. Similarly, some $Ni_{50}Mn_{50-x}Z_x$ alloys with $x \leq 25$ at.% undergo structural transition from cubic $L2_1$ to tetragonal martensitic phase. The transition is *martensitic* so the atoms maintain their local neighborhood. The martensite phase is either *fct* consisting of two $L1_0$ cells stacked on each other in *[001]* direction (so, called **2M**), or more complex structure, consisting of several **2M** (e.g. **10M**).

We consider the simpler case of tetragonal **2M** lattice with lattice parameters $a_{fct} = c_{fct} = \frac{\sqrt{2}a}{2}$, $b_{fct}/a_{L2_1} < 1$. In martensitic $Ni_{50}Mn_{50-x}Z_x$ alloy, where $x < 25$ at.%, Mn-pairs with the following distances exist: $\frac{\sqrt{2}a_{fct}}{2}$, $\frac{b_{fct}}{2}$, a_{fct}, $\sqrt{\frac{a_{fct}^2}{2} + \frac{b_{fct}^2}{4}}$ and $\sqrt{a_{fct}^2 + \frac{b_{fct}^2}{4}}$. However, in the stoichiometric case only two distances are left: a_{fct} and $\sqrt{\frac{a_{fct}^2}{2} + \frac{b_{fct}^2}{4}}$. Considering that $a_{fct} = \frac{\sqrt{2}a}{2}$ and $b_{fct}/a_{L2_1} \simeq 0.95$, the Mn-Mn distances can be written in terms of the lattice parameter of cubic phase *a*: $\frac{a}{2}$ and $\lesssim \frac{a}{2}$, $\frac{\sqrt{2}a}{2}$ and $\lesssim \frac{\sqrt{2}a}{2}$, $\lesssim \frac{\sqrt{3}a}{2}$, where $\frac{\sqrt{2}a}{2}$ and $\lesssim \frac{\sqrt{2}a}{2}$ are the distances present in stoichiometric case. On further doping, when $x \gtrsim 25\, at.\%$ number of Mn pairs with these distances decreases.

Therefore, there are 3 possible distances between Mn pairs, existing in austenite non-stoichiometric Heusler alloy, and only a single distance remains in stoichiometric alloy. On structural transformation into martensite, some Mn pairs become closer.

The lattice parameter of austenite phase of $Ni_{50}Mn_{36}Sn_{14}$ alloy is $a = 5.973\ \mathring{A}$ [68]. The possible Mn-Mn distances are: $\frac{a}{2} = 2.98(7)\ \mathring{A}$, $\frac{\sqrt{2}a}{2} = 4.22\ \mathring{A}$ and $\frac{\sqrt{3}a}{2} = 5.17\ \mathring{A}$. The distance $\frac{a}{2}$ is approximately the distance of Mn atoms coupling AF in NiMn lattice, $\frac{a}{2} \approx a_{NiMn}$. It is present either in austenite, or martensite states, however, on decreasing the Mn concentration, these pairs will become less in number and then vanish, i.e. AF correlations will decrease and die out. This argument is proved experimentally in this thesis. Therefore, we can conclude from this qualitative consideration that in the lattice of martensitic Ni-Mn-based Heusler alloys, nearest neighboring Mn atoms couple antiferromagnetically at $\frac{a}{2}$, while next nearest neighbors couple ferromagnetically at $\frac{\sqrt{2}a}{2}$.

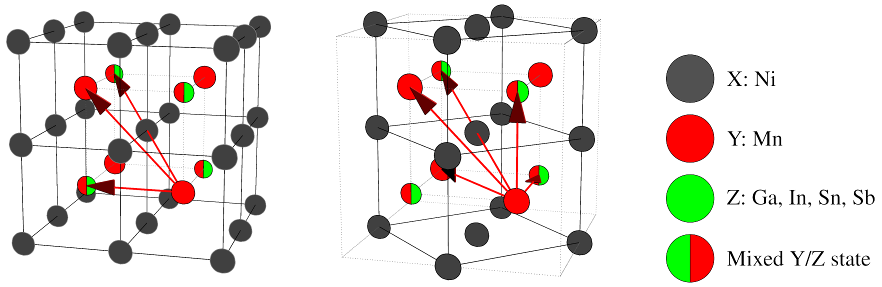

Figure 5.1: Possible distances between Mn atoms in $L2_1$ (a) and $L1_0$ (b) lattice.

This consideration is also supported by DFT calculations on the dependence of exchange parameters J of atoms in Heusler alloy lattice on interatomic distances. According to the results of these calculations, there is strong FM coupling between Ni and Mn atoms, while Mn atoms occupying *4a* and *4b* positions couple antiferromagnetically. The exchange parameter monotonically decreases with increasing distance between atoms, approaching 0 at distance $\lesssim a$. Therefore, the dominant ordering depends on number of Ni-Mn and Mn-Mn pairs and the lattice parameter. This means that it is possible to induce AF correlations in austenitic non-transforming Heusler alloy by applying hydrostatic pressure and reducing lattice parameter. The latter was experimentally proven [15].

As a result; there are three main factors influencing the magnetic interactions in Ni-Mn-based Heusler alloys with Ga, In, Sn, Sb:

stoichiometry: occurrence of AF coupled Mn-Mn pairs, linearly depends on Mn concentration;

doping element: affects the electronic structure and exchange parameters in the lattice and lattice parameter;

lattice parameter: affects the possible distances between Mn atoms, should be $\approx 5.8 - 6.1\ \mathring{A}$, so the distance between the nearest neighbouring Mn atoms is small enough for them to couple AF.

In particular, this correlates with M_s to the specific electron concentration $\frac{e}{a}$ as a general parameter in phase diagrams of Ni-Mn based Heuslers (introduced in section 2.3.1).

5.2 Evolution of magnetic interactions in martensitic Heusler alloys with temperature

As it was shown in previous subsection, AF correlations are present in martensitic Heusler alloys in the whole range of magnetic and structural phases. Here we discuss the development of these interactions with temperature. In section 4.3.1 we showed the temperature dependence of the measured FMR signal ($\frac{d\chi''}{dH}$) for the several NiMn-based martensitic Heusler alloys undergoing structural transformation: $Ni_{49.95}Mn_{24.67}Ga_{25.38}$, $Ni_{45.32}Mn_{30.33}Ga_{24.35}$, $Ni_{49.97}Mn_{30.35}Ga_{19.68}$, $Ni_{49.38}Mn_{34.80}Sn_{15.82}$ and $Ni_{49.37}Mn_{40.31}Sn_{9.92}$. Among them $Ni_{49.97}Mn_{30.35}Ga_{19.68}$ and $Ni_{49.37}Mn_{40.31}Sn_{9.92}$ exhibit a low magnetization region in the martensite phase in addition to the structural transformation.

As mentioned in the previous section, FMR spectra measured on all these samples show both FM and AF lines in the martensite phase below the magnetic order-disorder temperature T_C^M. The measured FMR spectra on powder samples consist of the superposition of resonance lines of differently oriented and shaped particles. Thus it is not possible to determine the behavior of separate lines. However, assuming that the particles are homogeneous and have the same composition, the resonance line position will differ from particle to particle due to crystalline anisotropy. Then, it is possible to speak about the behavior of lines with lowest and highest anisotropy values (in other words, trailing and leading edges of the signal $\frac{d\chi''}{dH}(H)$, respectively) in superposition, lying below the isotropic value $\frac{\omega}{\gamma}$, and similarly, about the behavior of lines with the highest anisotropy (in other words, trailing edge of the signal $\frac{d\chi''}{dH}(H)$) in the superposition lying above the isotropic value.

In case of the austenitic samples the measured spectrum consists of a superposition of FM lines. The width of the signal and position of the line do not change with temperature until $100\ K$ below Curie temperature of the austenite phase T_C^A. Then signal becomes narrower and moves towards the isotropic value. Above T_C^A there is a single line at $\frac{\omega}{\gamma}$present. The intensity of the FM lines is not constant with temperature: the magnitude of low anisotropy lines rises with heating, while higher anisotropy lines die out with temperature (e.g. compare FMR signals measured at $100\ K$ and $230\ K$ fig. 4.13(d)). This behavior is general for all austenitic samples and resemble the behavior of a conventional ferromagnet.

The case of the martensitic Heuslers is somewhat more complex. Although all martensitic Heusler alloys exhibit both FM and AF lines in martensitic state and only FM in austenitic state, the exact temperature dependent behavior of the measured signal differs from sample to sample.

In the case of the close-to-stoichiometry $Ni_{49.95}Mn_{24.67}Ga_{25.38}$ sample and Ni-poor $Ni_{45.32}Mn_{30.33}Ga_{24.35}$ sample, the FMR signal consist of two "humps" below and above the isotropic value $\frac{\omega}{\gamma}$, below the start of the martensitic transition temperature A_s, while above the transition only FM lines are present (e.g. see fig. 4.12(c)).

In both cases, the AF lines, lying above $\frac{\omega}{\gamma}$, behave as follows: the anisotropy is almost constant at lower temperatures, while in the vicinity of A_s, it decreases, and AF lines shift towards $\frac{\omega}{\gamma}$. No AF lines are detected above the end of the martensitic transition.

The behavior of FM lines in these samples is similar to non-martensitic samples. Anisotropy does not change in the martensite phase, so the position of FM lines is constant. It changes above A_s, and then the lines shift towards $\frac{\omega}{\gamma}$, reaching it as the sample undergoes magnetic order-disorder transition at the Curie temperature of the austenite T_C^A.

The intensity of both AF and FM lines in martensite state is about 100 times lower than the intensity of FM lines in FM austenite state. The intensity of the AF lines decreases as the temperature rises towards the martensite start temperature, while the intensity of FM lines in martensitic state is constant.

We observed the similar behavior of the resonance lines in Mn-rich $Ni_{49.38}Mn_{34.80}Sn_{15.82}$ sample (fig. 4.18(c)). Similar to the previous case, the FMR signal consist of two "humps" below and above isotropic value $\frac{\omega}{\gamma}$ below A_s and FM lines above the transition. However, in this case the martensitic transition occurs in the temperature range about $100\ K$, so the evolution of both AF and FM lines is more clear. Thus, one can see that the anisotropy related to the position of the AF resonance lines is constant below $30\ K$. It then weakens in the vicinity of the martensitic transition and continues to gradually decrease during the transition. It totally vanishes at the end of the transition around $200\ K$.

The cases of Mn-rich $Ni_{49.97}Mn_{30.35}Ga_{19.68}$ and $Ni_{49.37}Mn_{40.31}Sn_{9.92}$ (see fig. 4.14 and fig. 4.19, respectively) differ from the previously discussed cases. While in previous samples we observed the transition from magnetically ordered martensite to magnetically ordered austenite, in these samples the transition occurs from the magnetically ordered martensite to the austenite phase with low magnetization. In these samples we observed lower anisotropy of the AF lines than in previous samples and more complex behavior of the FM lines in martensite state. However, the general observation that AF lines are present only in the martensite phase is still valid for these samples.

The FMR experiments discussed above do not show presence of AF lines in FM austenite. However, in light of the conclusions in the previous section, we suggest that AF coupling is still present in this phase. At a fixed composition the lattice parameter is the only parameter ruling Mn-Mn pair distances and thus their exchange parameter. The dimensions of the cubic austenite cell slowly increases with increasing temperature which should gradually weaken the AF exchange. Neutron polarization experiments performed above Curie temperature of austenite phase

T_C^A confirm presence of AF correlations in this state. Thus, AF correlations should be also present in FM austenite.

We consider the case of $Ni_{50.42}Mn_{32.96}In_{16.63}$. At $T = 280\ K$ its lattice parameter is $a = 6.0111\ \mathring{A}$. According to table 4.2, the temperature coefficient equals $5.510^{-5}\ \mathring{A}/K$. Thus the lattice parameter at $T = 500\ K$ is $a \approx 6.0232\ \mathring{A}$. Polarized neutron scattering experiments performed on an alloy with a similar composition confirmed the presence AF correlations in the PM austenite phase so that Mn pairs still couple AF at distance $\frac{a}{2} = 3.0116\ \mathring{A}$. Therefore, Mn pairs should also couple AF at lower temperatures, when the interatomic distance is smaller.

Another example is the case of Mn-rich $Ni_{49.97}Mn_{30.35}Ga_{19.68}$. According to the neutron polarization data (see fig. 4.21(c) and (d)), the sample is in a low-magnetization martensite state at $400\ K$ and is in a low-magnetization austenite phase at $500\ K$. The spectra of magnetic cross sections measured at these temperatures are almost identical, meaning that the magnetic ordering is very similar in these phases. The intensity of the forward scattering is higher in the austenite phase, which is consistent with the fact that FM coupling is stronger in the austenite. While the spectra of the diffuse scattering between $1.2 < q(\mathring{A}) < 2.3$ is similar, meaning that the strength of AF correlations are the same both in the martensitic and austenitic phases.

These results are also consistent with temperature dependent Hall effect measurements performed on NiMn-based Heusler alloys, yielding no difference in Hall constants below and above the martensitic transition and implying that the magnetic subsystem is very similar in martensite and austenite phases.

The fact that the FMR method does not resolve the AF lines in the austenite phase can be explained by the either the low intensity of AF lines compared to the FM lines in austenite or by the hypothesis that the AF interactions are weak enough to be easily suppressed by applying the external field. In other words, a magnetic field greater than isotropic value $H_0 = 337\ mT$, which is required for observation of AF resonance also flips the magnetic moments in Mn pairs. Additionally, similar considerations can also be applied to the PM phase of austenite, where a single line at the isotropic value is observed.

5.2.1 Evolution of the magnetic entities around the martensitic transition

We conclude from our FMR measurements that on heating, both the anisotropy and the intensity of the AF lines decrease starting from temperatures below the transition, and they are finally extinct as the transition finishes. The case for the sample with concentration close to stoichiometry, $Ni_{49.95}Mn_{24.67}Ga_{25.38}$, sets an example (cf. fig. 4.15(b) measurements taken with smaller step in temperature); as well as the Mn-rich $Ni_{49.38}Mn_{34.80}Sn_{15.82}$ sample (cf. fig. 4.18(c) transition occurring over about $100\ K$).

It worth noting that the FMR experiments themselves, being field dependent, can break weak AF or ferrimagnetic order and induce austenite during the measurement at constant temperature close to the transition, so that the FMR data should be analyzed with certain care. However, it is possible to apply the polarized neutron scattering technique to probe the lattice structure and the magnetic subsystem non-disruptively. Although this method is applicable only in the low magnetization state, it is possible to measure the development of the magnetic entities in both directions of the transition.

We consider the data obtained from neutron depolarization measurements on $Ni_{49.97}Mn_{30.35}Ga_{19.68}$ (see fig. 4.21(b)). Initially, the flipping ratio $R_F = 1$ because the polarized beam is depolarized by the sample. On heating, as the sample undergoes magnetic order-disorder transition in martensitic state and its net magnetization decreases, R_F increases and reaches its maximum at $T = 395\ K$. At this temperature ($\approx 400\ K$), the sample resides in the martensite state. However, the flipping ratio starts decreasing on further heating, and the sample finally resides in austenite state. Therefore, the decrease of R_F can be explained by development of FM entities as the sample undergoes the structural transition. This can also be seen by comparing magnetic cross section spectra measured in both phases (see fig. 4.21(c)), discussed in present section: FM coupling is stronger in the austenite than in martensite.

We performed neutron depolarization measurements on heating and cooling in a broad temperature range on Co-doped Mn-rich $Ni_{45}Mn_{35}In_{15}Co_5$ exhibiting low magnetization in the martensitic state. In fig. 5.2(a) we show the temperature dependence of the magnetization measured in $5\ mT$ magnetic field. This data has similar behavior to the magnetization in neutron polarization experiments. The characteristic temperatures of the structural and magnetic transitions were determined from DSC measurements (see section 4.4 and fig. 4.26(a)). As mentioned earlier, neutron depolarization occurs due to an interaction between the incident neutron beam and the FM domain walls. The beam becomes depolarized ($R_F = 1$) if FM domains are present. The smaller the number of domain walls the less is the beam depolarized; e.g. in low magnetization martensite phase $R_F = 4$ instead of 23 in PM austenite (see fig. 4.26(c)). Thus, the reversed flipping ratio R_F^{-1} can be used to estimate the evolution of the magnetization of the sample with temperature.

We show the temperature dependence of $R_F^{-1}(T)$ in the vicinity of the transition in fig. 5.2(b). On heating from $5\ K$ (FW protocol), R_F^{-1} starts increasing from $A_s = 255\ K$ as FM entities develop during the martensitic transition. The beam becomes depolarized at $280\ K$ as the net magnetization increases. Consequently, the austenite finish temperature $A_f = 306\ K$ cannot be resolved with this method. The following plateau $280\ K < T < T_C^A$ ($R_F^{-1} \approx 1$) corresponds to the end of the martensitic transition and the FM austenite phase. Above $T_C^A = 393\ K$, the beam is polarized and R_F^{-1} is low. The abrupt drop corresponds to the Curie temperature of the austenite. On cooling from $500\ K$ (FC protocol), the plateau lies between $280\ K < T < T_C^A$ and R_F^{-1} decreases starting from $M_s = 289\ K$. However, the decrease continues below $M_f = 242\ K$ down to $150\ K$. Below this temperature the flipping ratio is constant on both heating and cooling: $R_F^{-1} \approx 0.25$

The data discussed above yields the result that FM entities still exist down to $100\ K$ below the finish temperature of the martensitic transition, while according to magnetization and calorimetric data, the transition should have already finished at this temperature. It is difficult to state with this method, whether the similar process occurs on the reverse transformation branch, as the net magnetization depolarizes the beam. However, this effect could be suppressed by the FM phase itself.

As a conclusion, AF interactions are present in all martensitic NiMn-based Heusler alloys in both martensite and austenite phases. These interactions are random, occurring at certain distances (see section 5.1). In FM austenite, these correlations were not observed by the FMR method as they can be easily suppressed by a relatively small magnetic field ($\approx 500\ mT$). However, AF correlations are still present in austenite, and neutron polarization experiments discussed above demonstrate that these correlations have lead to the same σ_{mag} cross sections in low magnetization martensite and austenite phases. Additionally, we have shown that FM still evolves after the M_f temperature.

5.3 Influence of magnetic field on lattice properties in Ni-Mn-In alloy

In section 2.1.1 we mentioned the phenomenon of austenite arrest, occurring in martensitic Heusler alloys in high fields above $5\,T$. This phenomenon was initially observed in $Ni_{45}Co_5Mn_{36.7}In_{13.3}$ alloy by means of resistivity measurements and X-ray diffraction analysis (see fig. 2.4(a-c)) [39]. In our work we carried out similar X-ray diffraction experiment on sintered $Ni_{50.42}Mn_{32.96}In_{16.63}$ powder sample. Applying the magnetic field in this alloy results in decreasing the cell volume of both martensite and austenite phases. The application of the field at a given temperature results in a smaller volume-change compared to field-cooling to this temperature (see table 4.2). However, According to our diffraction data, there is no austenite phase below M_f, neither in ZFC nor in FC cases. Therefore, the structural trans-

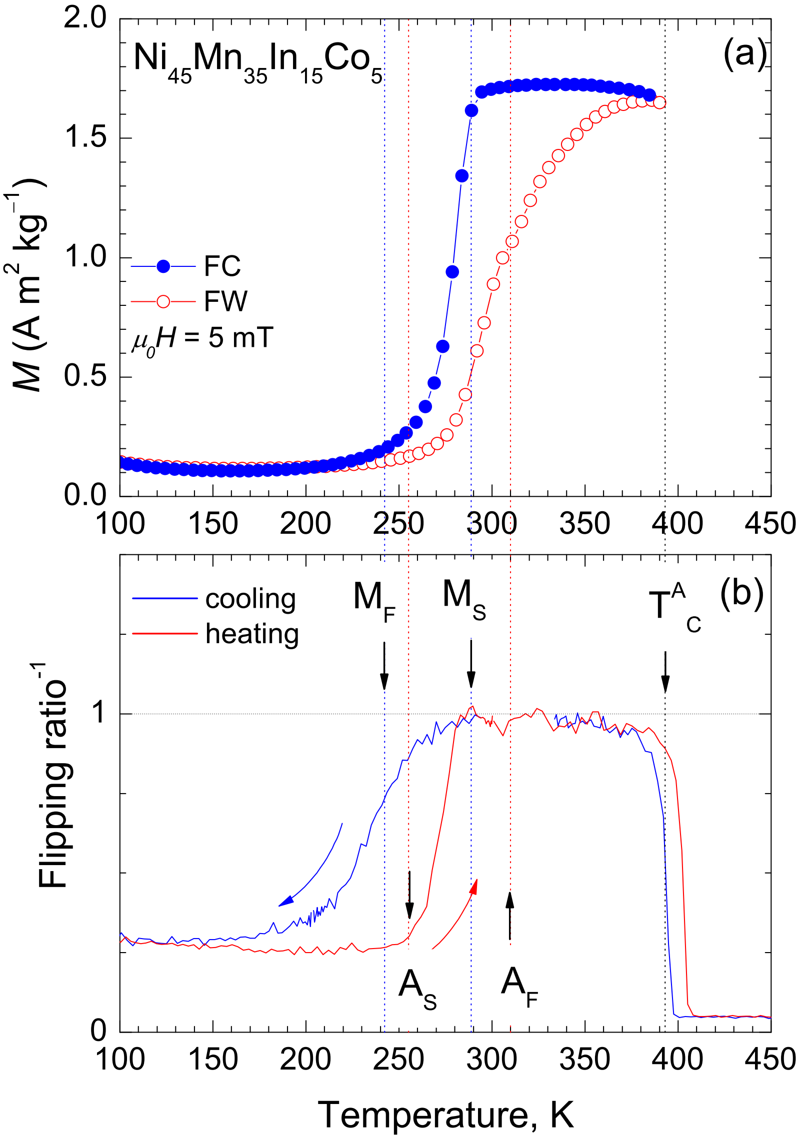

Figure 5.2: Temperature dependence of the magnetization $M(T)$ measured in $5\,mT$ field (a) and reversed flipping ratio $R_F^{-1}(T)$ (b) in the vicinity of the structural transition in $Ni_{45}Mn_{35}In_{15}Co_5$ sample. The labeled temperatures of the structural and magnetic transitions were obtained from the DSC measurements (see fig. 4.26(a))

formation fully occurs in $Ni_{50.42}Mn_{32.96}In_{16.63}$ alloy in fields up to 5 T. This result was also observed by X-ray diffraction measurements on $Ni_{46}Mn_{41}In_{13}$ alloy [67].

We suggest the following explanation for the observed phenomena. The external magnetic field stabilizes the phase with higher magnetization at a given temperature resulting in a linear shift of M_s with field (see section 2.3.3). In most of the Ni-Mn based Heuslers, where the martensite phase exhibits lower magnetization than the austenite phase, M_s shifts to lower temperatures with field, and it takes very large fields ($\approx 20\ T$) to stabilize austenite at temperatures close to 0 K. However, in Ni-Mn-In-Co the full austenite arrest was observed at 8 T field and partial arrest at 5 T [39]. This can be explained with decreasing mobility of the habit planes between austenite and martensite phases, so the austenite phase undercools in a cooling in field, and recovers on zero-field warming (e.g. see fig. 2.4(c)). In Ni-Mn-In alloys, the mobility of the habit plane is high enough, so that kinetic arrest is not observed in fields up to 5 T.

5.4 Influence of the transitional hysteresis on magnetocaloric effect in Ni-Mn-based Heusler alloys

As mentioned in section 2.2.1, the maximum of the MCE is expected to be around the 1^{st} and 2^{nd} order transitions, where the total entropy change is largest. Martensitic NiMn-based Heusler alloys undergo 1^{st} order magnetostructural transition, which can be induced by temperature, external field and pressure. These transitions exhibit temperature hysteresis of at least several degrees. The hysteresis shape and width is influenced by both microscale parameters like magnetic interactions in the lattice and lattice types, and macroscale parameters like habit plane mobility and the metallurgical state of alloy (purity, strain, etc). Additionally, since these alloys exhibit MSME, *training* should also change the parameters of the structural hysteresis. As the presence of hysteresis brings energy losses and irreversibility on field cycling, one can consider the methods concerning reducing the hysteresis width. However, possible technical applications of martensitic Heuslers such as the MCE does not necessarily require the cycling around the whole transition (i.e from above A_f to below M_f and back), but cycling around arbitrary *working* temperature in the transitional hysteresis region (i.e. $M_s < T < A_s$) can be sufficient. Thus, in our work, we have focused on the investigation of the influence of the structural hysteresis on the adiabatic temperature change and the behavior of the austenite-to-martensite ratio in the minor loops of the hysteresis. Summing up the results shown in section 4.2, we came up to a model for ΔT_{ad} estimation based on the consideration of $S_{total}(T, H)$, described in the following section.

5.4.1 Reversibility of the adiabatic temperature change around the magnetostructural transition

Following the schematic representation of the temperature dependence of the entropy around the transition, we consider field-cycling: fig. 5.3. In section 2.2.1 we have discussed the case of reversible MCE in the vicinity of a non-hysteretic transition, i.e. the absolute values of the adiabatic temperature change are equal on application and removal of the field.

First, we consider the case of a large field, when the forward branch of the martensitic transition in zero field lies lower than the in-field reverse transformation branch on S-T plane. Schematic graph of such a case is shown in fig. 5.3(a). Initially, the system resides on the reverse transformation branch at temperature $T = T_1$ and at zero-field with austenite-to-martensite ratio $\left(\frac{a}{m}\right)_1$. This state results in a total entropy $S_{total} = S_0$. On the adiabatic application of the field, the system follows the $S_{total} = S_0$ line in the state on the in-field reverse transformation branch with austenite-to-martensite ratio $\left(\frac{a}{m}\right)_2 > \left(\frac{a}{m}\right)_1$. This results in a negative adiabatic temperature change $\Delta T_{ad}^{1\to2} = T_2 - T_1 < 0$ due to the inverse MCE. On the adiabatic removal of the field, the system should return on the zero-field reverse transformation branch. However, due to hysteresis, the austenite-to-martensite ratio is not fully recovered. Therefore after the field removal, it resides on forward transformation branch and its austenite-to-martensite ratio is $\left(\frac{a}{m}\right)_2 > \left(\frac{a}{m}\right)_3 > \left(\frac{a}{m}\right)_1$. The adiabatic temperature change is positive $\Delta T_{ad}^{2\to3} = T_3 - T_2 > 0$. However, if the field is adiabatically applied again, the system should return back to the state on the in-field reverse transformation branch with austenite-to-martensite ratio $\left(\frac{a}{m}\right)_2 > \left(\frac{a}{m}\right)_3$, resulting in a negative adiabatic temperature change $\Delta T_{ad}^{3\to2} = T_2 - T_3 < 0$ due to the inverse MCE. Further adiabatic removal of the field will drive the system to a state with austenite-to-martensite ratio $\left(\frac{a}{m}\right)_3$ at temperature T_3 again. This results in a positive adiabatic temperature change $\Delta T_{ad}^{2\to3} = T_3 - T_3 > 0$. Further cycles of applying and removing the field will result in the system running between states at T_2 and T_3.

Therefore, the first application of the field leads to a negative temperature change of $\Delta T_{ad}^{1\to2} = T_2 - T_1 < 0$, while the following removal of the field and further field cycles result in a lower constant absolute value of the adiabatic temperature change: $|\Delta T_{ad}^{3\to2}| = |\Delta T_{ad}^{2\to3}|$, while during all cycles the MCE is inverse. This adiabatic temperature change will be the "real" working value obtainable on field cycling in technical applications. Both Ni-Mn-In samples we measured exhibited field cycling properties as in the case discussed above (see fig. 4.7).

The next case we consider is the case of lower field when the forward branch of the martensitic transition in zero field lies higher than the in-field reverse transformation branch on S-T plane. A schematic representation of such a case is shown in fig. 5.3(b). Initially, the system resides on the reverse transformation branch at temperature $T = T_1$ and zero field with austenite-to-martensite ratio $\left(\frac{a}{m}\right)_1$. This state has total entropy $S_{total} = S_0$. On the adiabatic application of the field, the system follows the $S_{total} = S_0$ line in the state on the in-field reverse transformation branch with austenite-to-martensite ratio $\left(\frac{a}{m}\right)_2 > \left(\frac{a}{m}\right)_1$. This results in a negative adiabatic temperature change $\Delta T_{ad}^{1\to2} = T_2 - T_1 < 0$ due to the inverse MCE. On the adiabatic removal of the field, the system should return on the zero-field reverse transformation branch. However, since the hysteresis in the austenite-to-martensite ratio is not fully recovered, it resides on the forward transformation branch after the field removal. Its austenite-to-martensite ratio is $\left(\frac{a}{m}\right)_2 > \left(\frac{a}{m}\right)_3 > \left(\frac{a}{m}\right)_1$. In contrast to the prior case, the zero-field forward transformation branch lies higher than in-field reverse one, so the expected adiabatic temperature change is again negative $\Delta T_{ad}^{2\to3} = T_3 - T_2 < 0$ and the MCE is conventional. However, if the field is adiabatically applied again, the system should turn back to the state on the in-field reverse transformation branch with austenite-to-martensite ratio $\left(\frac{a}{m}\right)_2 > \left(\frac{a}{m}\right)_3$ resulting in a positive adiabatic temperature change $\Delta T_{ad}^{3\to2} = T_2 - T_3 > 0$ due to the conventional MCE. Further adiabatic removal of the field will drive the system to the state with austenite-to-martensite ratio $\left(\frac{a}{m}\right)_3$ at temperature T_3 again resulting in the negative adiabatic temperature change $\Delta T_{ad}^{2\to3} = T_3 - T_3 > 0$. Further cycles of applying and removing the field will result in system running between states at T_2 and T_3.

In this case, the first application of the field leads to the negative temperature change of $\Delta T_{ad}^{1\to2} = T_2 - T_1 < 0$, while the following removal of the field and further field cycles result in a lower constant absolute value of adiabatic temperature change: $|\Delta T_{ad}^{3\to 2}| = |\Delta T_{ad}^{2\to 3}|$. During all cycles the MCE is conventional, on contrast to the prior case. This adiabatic temperature change will be *real* the working value on field cycling in technical applications. The $Ni_{48.56}Mn_{34.94}Sn_{16.50}$ sample also exhibits the field cycling properties as in the case discussed above (see fig. 4.5).

As a result of these consideration the following can be concluded:

- The value of adiabatic temperature change on the first application of the field $\Delta T_{ad}^{1\to 2} = T_2 - T_1$ characterizes maximum ΔT_{ad}, while $\Delta T_{ad}^{2\leftrightarrow 3}$ characterizes the system's cycling properties, as following temperature changes are constant.
- Also this simple consideration of influence of the transitional hysteresis leads to the result, that width of the hysteresis should be considered together with the hysteresis field shift, as interplay of these parameters results in the different cycling behaviors of temperature change.
- The other interesting result from this model is that if the system initially resides in the state at temperature T_2 on forward transformation branch, absolute value of the adiabatic temperature change will be constant during all the cycles.

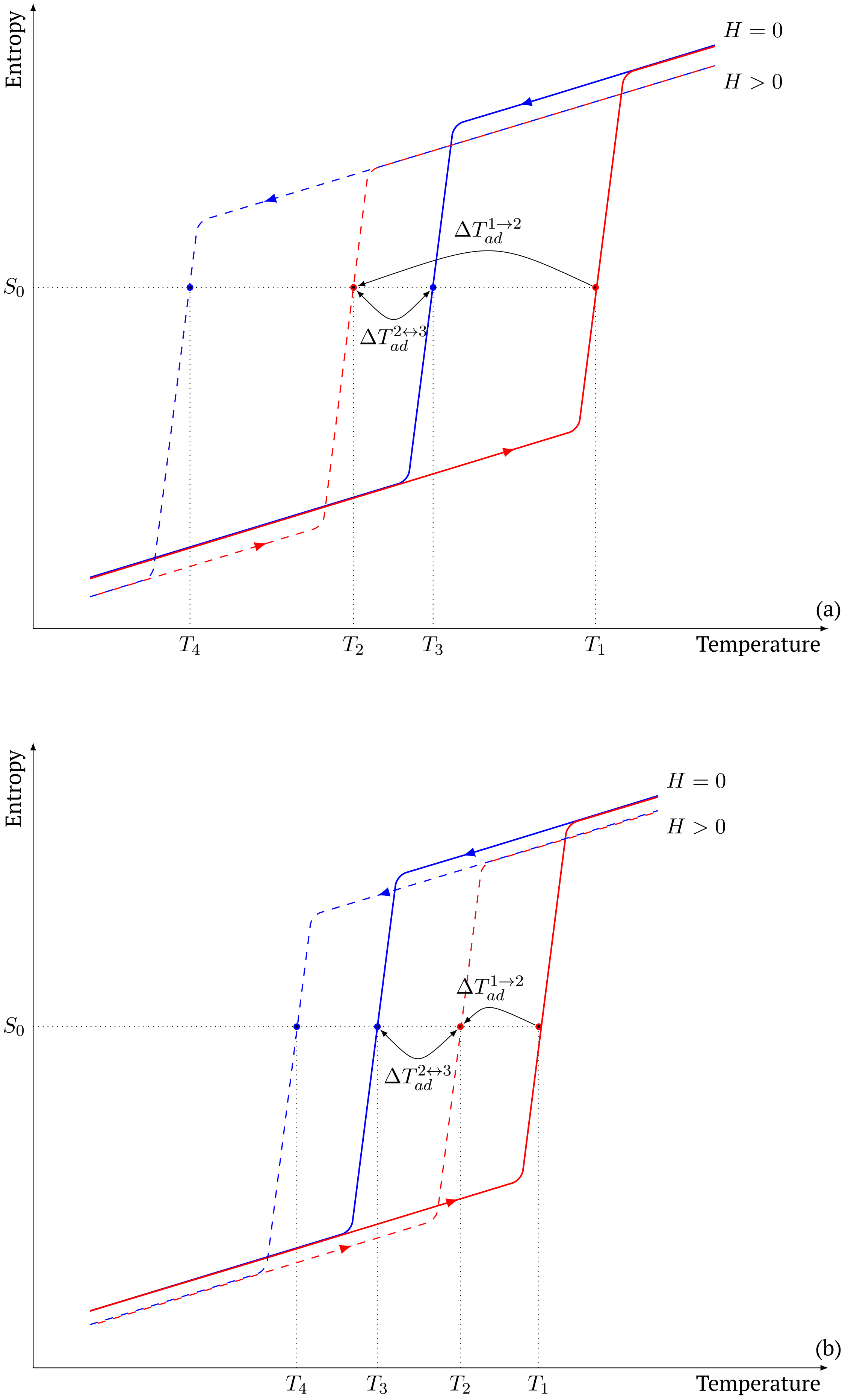

Figure 5.3: Schematic representation of the inverse MCE in the case of overlapping (a) and non-overlapping (b) transitional hysteresis.

6 Conclusion

This thesis is devoted to the understanding of the nature of magnetic interactions in martensitic Ni-Mn based Heusler alloys and the influence of the structural transition hysteresis on the exhibited magnetocaloric effects in these alloys.

Th martensitic Heusler alloys are *smart* materials, with properties and possible application that depend on the martensitic transition they exhibit. There are hypotheses that AF interactions play the key role in magnetostructural transitions in Ni-Mn based Heuslers.

In the present work we studied magnetic properties of the Heusler alloys using various techniques like polarized neutron scattering and FMR to understand the types of the magnetic interactions in the alloy. We carried out these studies on the Ni-Mn-Z (Z = Ga, Sn) alloy series varying the concentration of the doping element, thus changing number of Mn pairs in the unit cell. Samples with stoichiometric Ni_2MnZ composition as well as Mn-rich and Mn-poor compositions were studied. Using the neutron polarization analysis we observed AF correlations in martensitic Mn-rich samples and much weaker AF correlations in non-transforming samples. Using the FMR we observed evolution of the AF interactions with temperature in the martensite phase of Heusler alloys, while only FM interactions were observed in the austenite phase. As a result of the present work, we find that in Ni-Mn based Heusler alloys, AF interactions occur between nearest neighbor Mn atoms and that the presence of these interactions on the microscale leads to the occurrence of structural transformations at the macroscale. The parameters which influence these interactions are: the Mn concentration in the alloy, the doping elements (Ga, In, Sn, Sb and, possibly, 4^{th} element like Co) with the respect to initial NiMn alloy, and the lattice parameter depending on the composition of the alloy, as well as external magnetic field and pressure.

The transitional hysteresis in martensitic Heuslers yields on the one hand significant changes in the physical parameters bound to the lattice. The strong coupling between magnetic subsystem and lattice in NiMn-based Heusler alloys also makes its possible to induce structural transition with external magnetic field or pressure, rendering possible many technical applications of these alloys. On the other hand the transitional hysteresis brings irreversibilities and energy losses, making the above mentioned applications more difficult. In the present work we considered the influence of the transitional hysteresis on the MCE effect in Ni-Mn-In and Ni-Mn-Sn alloys under different measurement conditions and previous states of the sample. These alloys exhibit narrow (Ni-Mn-In) and wide (Ni-Mn-Sn) transitional hysteresises due to different strength of AF pinning in the lattice. We performed adiabatic field-cycling measurements on these alloys to study the reversibility of the MCE depending on the previous states of the sample. We conclude from our results, that the minor loops of the transitional hysteresis provide reversible states in the transition and their usage can be technically feasible.

List of abbreviations and symbols

A_f	finish temperature of the austenite growth
A_s	start temperature of the martensite growth
C	heat capacity
G	Gibb's free energy
H	magnetic field strength (intensity)
K	magnetic anisotropy
M_f	finish temperature of the martensite growth
M_s	start temperature of the martensite growth
M	magnetization
P	polarization vector
R_F	flipping ratio
T_C^A	magnetic order-disorder temperature of the austenite phase
T_C^M	magnetic order-disorder temperature of the martensite phase
T_B	blocking temperature
ΔS_{iso}	isothermal entropy change
ΔT_{ad}	adiabatic temperature change
$\Delta l/l$	relative length change
χ''	imaginary part of the ac susceptibility
$\frac{a}{m}$	austenite-to-martensite ratio
γ	gyromagnetic ratio
μ_0	vacuum permeability, $4\pi \cdot 10^{-7}\ H/m$
μ_B	Bohr magneton, $9.274 \cdot 10^{-27}\ J/T$
μ	magnetic moment, $\mu_B/atom$
ω/γ	isotropic value of the resonance field
ω	angular frequency
σ^{bgr}	cross section background intensity
σ^{inc}	spin-incoherent cross section
σ^{mag}	nuclear spin-coherent cross section
σ^{nuc}	magnetic cross section
a	lattice constant
$d\sigma/d\Omega$	differential scattering cross section
e/a	valence electron concentration per atom
q	scattering vector
10M	modulated monoclivic structure, with the period of 10 atomic layers
14M	modulated monoclinic structure, with the period of 14 atomic layers
2M	monoclinic structure, with the period of 2 atomic layers
4O	modulated orthorohmbic structure, with the period of 4 atomic layers
AF	antiferromagntetic

bcc	body-centered cubic
bct	body-centered tetragonal
D2B	D2B
DNS	diffuse neutron spectrometer
DSC	differential scanning calorymetry
EDX	energy dispersive X-ray analysis
FC	field cooled
fcc	face-centered cubic
fct	face-centered tetragonal
FI	ferrimagnetic
FM	ferromagnetic
FW	field warmed
MCE	magnetocaloric effect
MSME	magnetic shape memory effect
NSF	non-spin-flip
PM	paramagnetic
SF	spin-flip
SMA	shape memory alloys
SME	shape memory effect
SQUID	superconducting quantum interference device
XRD	X-Ray diffraction
ZFC	zero field cooled

List of Figures

List of Tables

7 Bibliography

[1] F. Heusler. Über die magnetische manganlegierungen. *Verhandlungen der Deutschen physikalischen Gesellschaft*, 5:219, 1903.

[2] F. Heusler, W. Starck, and E. Haupt. Über die synthese ferromagnetischer manganlegierungen. *Verhandlungen der Deutschen physikalischen Gesellschaft*, 5:220, 1903.

[3] Otto Heusler. Kristallstruktur und Ferromagnetismus der Mangan-Aluminium-Kupferlegierungen. *Annalen der Physik*, 411(2):155–201, 1934.

[4] R. A. de Groot, F. M. Mueller, P. G. van Engen, and K. H. J. Buschow. New class of materials: Half-metallic ferromagnets. *Phys. Rev. Lett.*, 50:2024–2027, Jun 1983.

[5] Thorsten Krenke. *Untersuchung der martensitischen Umwandlung und der magnetischen Eigenschaften Mangan-reicher Ni-Mn-In- und Ni-Mn-Sn-Heusler-Legierungen,*. PhD thesis, Department of Physics, Universität Duisburg Essen, 2007.

[6] K. Ullakko, J. K. Huang, C. Kantner, R. C. O'Handley, and V. V. Kokorin. Large magnetic-field-induced strains in Ni_2MnGa single crystals. *Applied Physics Letters*, 69(13):1966–1968, 1996.

[7] K. Ullakko, J.K. Huang, V.V. Kokorin, and R.C. O'Handley. Magnetically controlled shape memory effect in Ni_2MnGa intermetallics. *Scripta Materialia*, 36(10):1133 – 1138, 1997.

[8] R. C. O'Handley. Model for strain and magnetization in magnetic shape-memory alloys. *Journal of Applied Physics*, 83(6):3263–3270, 1998.

[9] A. Sozinov, A. A. Likhachev, N. Lanska, and K. Ullakko. Giant magnetic-field-induced strain in NiMnGa seven-layered martensitic phase. *Applied Physics Letters*, 80(10):1746–1748, 2002.

[10] V. K. Pecharsky and K. A. Gschneidner, Jr. Giant magnetocaloric effect in $Gd_5Si_2Ge_2$. *Phys. Rev. Lett.*, 78:4494–4497, Jun 1997.

[11] E. Brück. *Magnetocaloric refrigeration at ambient temperature*, volume 17. Amsterdam: Elsevier Science, 2008.

[12] Feng-Xia Hu, Bao-Gen Shen, and Ji-Rong Sun. Magnetic entropy change in $Ni_{51.5}Mn_{22.7}Ga_{25.8}$ alloy. *Applied Physics Letters*, 76(23):3460–3462, 2000.

[13] Feng-Xia Hu, Bao-Gen Shen, Ji-Rong Sun, and Guang-Heng Wu. Large magnetic entropy change in a Heusler alloy $Ni_{52.6}Mn_{23.1}Ga_{24.3}$ single crystal. *Phys. Rev. B*, 64:132412, Sep 2001.

[14] Thorsten Krenke, Eyup Duman, Mehmet Acet, Eberhard F. Wassermann, Xavier Moya, Lluis Manosa, and Antoni Planes. Inverse magnetocaloric effect in ferromagnetic Ni-Mn-Sn alloys. *Nat Mater*, 4:450–454, Jul 2005.

[15] Seda Aksoy. *Magnetic interactions in martensitic Ni-Mn based Heusler systems*. PhD thesis, Department of Physics, Universität Duisburg Essen, 2010.

[16] Igor Dubenko, Mahmud Khan, Arjun Kumar Pathak, Bhoj Raj Gautam, Shane Stadler, and Naushad Ali. Magnetocaloric effects in Ni-Mn-X based Heusler alloys with X=Ga, Sb, In. *Journal of Magnetism and Magnetic Materials*, 321(7):754 – 757, 2009. Proceedings of the Forth Moscow International Symposium on Magnetism.

[17] A.K. Pathak, I. Dubenko, C. Pueblo, P. Basnyat, S. Stadler, and N. Ali. The effect of partial substitution of Ni by Co on the magnetic and electrical properties of $Ni_{50}Mn_{35}In_{15}$ Heusler alloy. *Magnetics, IEEE Transactions on*, 46(6):1444 –1446, june 2010.

[18] Z. H. Liu, H. Liu, X. X. Zhang, X. K. Zhang, John Q. Xiao, Z. Y. Zhu, X. F. Dai, G. D. Liu, J. L. Chen, and G. H. Wu. Large negative magnetoresistance in quaternary Heusler alloy $Ni_{50}Mn_{8}Fe_{17}Ga_{25}$ melt-spun ribbons. *Applied Physics Letters*, 86(18):182507, 2005.

[19] V.N. Prudnikov, A.P. Kazakov, I.S. Titov, N.S. Perov, A.B. Granovskii, I.S. Dubenko, A.K. Pathak, N. Ali, A.P. Zhukov, and J. Gonzalez. Hall effect in a martensitic transformation in Ni-Co-Mn-In Heusler alloys. *JETP Letters*, 92:666–670, 2010.

[20] Igor Dubenko, Tapas Samanta, Arjun Kumar Pathak, Alexandr Kazakov, Valerii Prudnikov, Shane Stadler, Alexander Granovsky, Arcady Zhukov, and Naushad Ali. Magnetocaloric effect and multifunctional properties of Ni-Mn-based Heusler alloys. *Journal of Magnetism and Magnetic Materials*, 324(21):3530 – 3534, 2012. Fifth Moscow international symposium on magnetism.

[21] K. Koyama, T. Igarashi, H. Okada, K. Watanabe, T. Kanomata, R. Kainuma, W. Ito, K. Oikawa, and K. Ishida. Magnetic and thermoelectric properties of $Ni_{50}Mn_{36}Sn_{14}$ in high-magnetic fields. *Journal of Magnetism and Magnetic Materials*, 310(2, Part 3):e994 – e995, 2007. Proceedings of the 17th International Conference on Magnetism The International Conference on Magnetism.

[22] S. Y. Yu, Z. H. Liu, G. D. Liu, J. L. Chen, Z. X. Cao, G. H. Wu, B. Zhang, and X. X. Zhang. Large magnetoresistance in single-crystalline $Ni_{50}Mn_{50-x}In_{x}$ alloys (x = 14–16) upon martensitic transformation. *Applied Physics Letters*, 89(16):162503, 2006.

[23] Keiichi Koyama, Hironari Okada, Kazuo Watanabe, Takeshi Kanomata, Ryosuke Kainuma, Wataru Ito, Katsunari Oikawa, and Kiyohito Ishida. Observation of large magnetoresistance of magnetic Heusler alloy $Ni_{50}Mn_{36}Sn_{14}$ in high magnetic fields. *Applied Physics Letters*, 89(18):182510, 2006.

[24] Thorsten Krenke, Mehmet Acet, Eberhard F. Wassermann, Xavier Moya, Lluís Mañosa, and Antoni Planes. Martensitic transitions and the nature of ferromagnetism in the austenitic and martensitic states of $Ni-Mn-Sn$ alloys. *Phys. Rev. B*, 72:014412, Jul 2005.

[25] Thorsten Krenke, Mehmet Acet, Eberhard F. Wassermann, Xavier Moya, Lluís Mañosa, and Antoni Planes. Ferromagnetism in the austenitic and martensitic states of $Ni-Mn-In$ alloys. *Phys. Rev. B*, 73:174413, May 2006.

[26] R. Y. Umetsu, R. Kainuma, Y. Amako, Y. Taniguchi, T. Kanomata, K. Fukushima, A. Fujita, K. Oikawa, and K. Ishida. Mössbauer study on martensite phase in $Ni_{50}Mn_{36.5}{}^{57}Fe_{0.5}Sn_{13}$ metamagnetic shape memory alloy. *Applied Physics Letters*, 93(4):042509, 2008.

[27] V. V. Khovaylo, T. Kanomata, T. Tanaka, M. Nakashima, Y. Amako, R. Kainuma, R. Y. Umetsu, H. Morito, and H. Miki. Magnetic properties of $Ni_{50}Mn_{34.8}In_{15.2}$ probed by Mössbauer spectroscopy. *Phys. Rev. B*, 80:144409, Oct 2009.

[28] S. Aksoy, M. Acet, P. P. Deen, L. Mañosa, and A. Planes. Magnetic correlations in martensitic Ni-Mn-based Heusler shape-memory alloys: Neutron polarization analysis. *Phys. Rev. B*, 79:212401, Jun 2009.

[29] K. Ōtsuka and C.M. Wayman, editors. *Shape Memory Materials*. Cambridge University Press, 1998.

[30] Floris Osmond. *Microscopic analysis of metals*. Charles Griffin and Company, 1904.

[31] F.X. Kayser and J.W. Patterson. Sir William Chandler Roberts-Austen — His role in the development of binary diagrams and modern physical metallurgy. *Journal of Phase Equilibria*, 19(1):11–18, 1998.

[32] C.M. Wayman and H.K.D.H. Bhadeshia. Phase transformations, nondiffusive. In *Physical Metallurgy*, volume 2, chapter 16, pages 1507–1554. North-Holland, 4 edition, 1996.

[33] Aleksandr N Vasil'ev, Vasilii D Buchel'nikov, T Takagi, Vladimir V Khovailo, and Emmanuil I Estrin. Shape memory ferromagnets. *Physics-Uspekhi*, 46(6):559, 2003.

[34] Antoni Planes, Lluìs Mañosa, and Mehmet Acet. Magnetocaloric effect and its relation to shape-memory properties in ferromagnetic Heusler alloys. *Journal of Physics: Condensed Matter*, 21(23):233201, 2009.

[35] C.M. Wayman T.A. Schroeder. The formation of martensite and the mechanism of the shape memory effect in single crystals of Cu-Zn alloys. *Acta Metallurgica*, 25(12):1375–1391, December 1977.

[36] R. Wasilewsky. *Phase transformations, nondiffusive*, page 245. J. Perkin (Ed.),Plenum, New York, 1975.

[37] C.M. Wayman T.A. Schroeder. The two-way shape memory effect and other "training" phenomena in Cu-Zn single crystals. *Scripta Metallurgica*, 11(3):225–230, March 1977.

[38] Thorsten Krenke, Eyüp Duman, Mehmet Acet, Eberhard F. Wassermann, Xavier Moya, Lluís Mañosa, Antoni Planes, Emmanuelle Suard, and Bachir Ouladdiaf. Magnetic superelasticity and inverse magnetocaloric effect in Ni-Mn-In. *Phys. Rev. B*, 75:104414, Mar 2007.

[39] Wataru Ito, Kouhei Ito, Rie Y. Umetsu, Ryosuke Kainuma, Keiichi Koyama, Kazuo Watanabe, Asaya Fujita, Katsunari Oikawa, Kiyohito Ishida, and Takeshi Kanomata. Kinetic arrest of martensitic transformation in the NiCoMnIn metamagnetic shape memory alloy. *Applied Physics Letters*, 92(2):021908, 2008.

[40] W. Ito, Y. Imano, R. Kainuma, Y. Sutou, K. Oikawa, and K. Ishida. Martensitic and magnetic transformation behaviors in Heusler-type NiMnIn and NiCoMnIn metamagnetic shape memory alloys. *Metallurgical and Materials Transactions A*, 38:759–766, 2007.

[41] K A GschneidnerJr, V K Pecharsky, and A O Tsokol. Recent developments in magnetocaloric materials. *Reports on Progress in Physics*, 68(6):1479, 2005.

[42] A.M. Tishin. Magnetocaloric effect in strong magnetic fields. *Cryogenics*, 30(2):127 – 136, 1990.

[43] V. K. Pecharsky and Jr. K. A. Gschneidner. Some common misconceptions concerning magnetic refrigerant materials. *Journal of Applied Physics*, 90(9):4614–4622, 2001.

[44] A. M. Tishin, K. A. Gschneidner, and V. K. Pecharsky. Magnetocaloric effect and heat capacity in the phase-transition region. *Phys. Rev. B*, 59:503–511, Jan 1999.

[45] E. Warburg. Magnetische Untersuchungen. *Annalen der Physik*, 249(5):141–164, 1881.

[46] P. Langevin. Magnétisme et théorie des électrons. *Ann. Chim. Phys. Chem.*, 5(70), 1905.

[47] P. Debye. Einige Bemerkungen zur Magnetisierung bei tiefer Temperatur. *Annalen der Physik*, 386(25):1154–1160, 1926.

[48] W. F. Giauque. A thermodynamic treatment of certain magnetic effects. a proposed method of producing temperatures considerably below 1° absolute. *Journal of the American Chemical Society*, 49(8):1864–1870, 1927.

[49] W. F. Giauque and D. P. MacDougall. Attainment of temperatures below 1° absolute by demagnetization of $Gd_2(SO_4)_3 \cdot 8H_2O$. *Phys. Rev.*, 43:768–768, May 1933.

[50] W.J De Haas, E.C Wiersma, and H.A Kramers. Experiments on adiabatic cooling of paramagnetic salts in magnetic fields. *Physica*, 1(1–6):1 – 13, 1934.

[51] Zimm C, Jastrab A, Sternberg A, Pecharsky V K, Gschneidner K Jr, Osborne M, and Anderson. volume I, page 1759. 1998.

[52] Vitalij K. Pecharsky and Karl A. Gschneidner Jr. Magnetocaloric effect and magnetic refrigeration. *Journal of Magnetism and Magnetic Materials*, 200(1–3):44 – 56, 1999.

[53] Thorsten Krenke, Eyüp Duman, Mehmet Acet, Xavier Moya, Lluís Ma nosa, and Antoni Planes. Effect of Co and Fe on the inverse magnetocaloric properties of Ni-Mn-Sn. *Journal of Applied Physics*, 102(3):033903, 2007.

[54] I. Titov, M. Acet, M. Farle, D. González-Alonso, L. Mañosa, A. Planes, and T. Krenke. Hysteresis effects in the inverse magnetocaloric effect in martensitic Ni-Mn-In and Ni-Mn-Sn. *Journal of Applied Physics*, 112(7):073914, 2012.

[55] V. I. Zverev, A. M. Tishin, and M. D. Kuz'min. The maximum possible magnetocaloric Delta T effect. *Journal of Applied Physics*, 107(4):043907, 2010.

[56] M. Acet, Ll. Mañosa, and A. Planes. *Chapter Four - Magnetic-Field-Induced Effects in Martensitic Heusler-Based Magnetic Shape Memory Alloys"*, volume 19 of *Handbook of Magnetic Materials*, pages 231 – 289. Elsevier, 2011.

[57] N. Lanska, O. Söderberg, A. Sozinov, Y. Ge, K. Ullakko, and V. K. Lindroos. Composition and temperature dependence of the crystal structure of Ni-Mn-Ga alloys. *Journal of Applied Physics*, 95(12):8074–8078, 2004.

[58] Y. Sutou, Y. Imano, N. Koeda, T. Omori, R. Kainuma, K. Ishida, and K. Oikawa. Magnetic and martensitic transformations of NiMnX(X = In,Sn,Sb) ferromagnetic shape memory alloys. *Applied Physics Letters*, 85(19):4358–4360, 2004.

[59] E. Wachtel, F. Henninger, and B. Predel. Constitution and magnetic properties of Ni-Mn-Sn alloys - solid and liquid state. *Journal of Magnetism and Magnetic Materials*, 38(3):305 – 315, 1983.

[60] E. Krén, E. Nagy, I. Nagy, L. Pál, and P. Szabó. Structures and phase transformations in the MnNi system near equiatomic concentration. *Journal of Physics and Chemistry of Solids*, 29(1):101 – 108, 1968.

[61] Seda Aksoy, Mehmet Acet, Eberhard F. Wassermann, Thorsten Krenke, Xavier Moya, Lluís Mañosa, Antoni Planes, and Pascal P. Deen. Structural properties and magnetic interactions in martensitic Ni-Mn-Sb alloys. *Philosophical Magazine*, 89(22-24):2093–2109, 2009.

[62] Mahmud Khan, Naushad Ali, and Shane Stadler. Inverse magnetocaloric effect in ferromagnetic $Ni_{50}Mn_{37+x}Sb_{13-x}$ Heusler alloys. *Journal of Applied Physics*, 101(5):053919, 2007.

[63] Mahmud Khan, Igor Dubenko, Shane Stadler, and Naushad Ali. Magnetostructural phase transitions in $Ni_{50}Mn_{25+x}Sb_{25-x}$ Heusler alloys. *Journal of Physics: Condensed Matter*, 20(23):235204, 2008.

[64] L. Pál, E. Krén, G. Kádár, P. Szabó, and T. Tarnóczi. Magnetic structures and phase transformations in Mn-based CuAu-I type alloys. *Journal of Applied Physics*, 39(2):538–544, 1968.

[65] V. Krasevec, P. Delavignette, and S. Amelinckx. Superstructure due to periodic twinning in quenched NiMn-alloy. *Materials Research Bulletin*, 2(11):1029 – 1034, 1967.

[66] P J Brown, A P Gandy, K Ishida, W Ito, R Kainuma, T Kanomata, K U Neumann, K Oikawa, B Ouladdiaf, A Sheikh, and K R A Ziebeck. Magnetic and structural properties of the magnetic shape memory compound $Ni_2Mn_{1.48}Sb_{0.52}$. *Journal of Physics: Condensed Matter*, 22(9):096002, 2010.

[67] P J Brown, A P Gandy, R Kainuma, T Kanomata, K U Neumann, K Oikawa, B Ouladdiaf, A Sheikh, and K R A Ziebeck. The field and temperature dependence of the magnetic and structural properties of the shape memory compound $Ni_{1.84}Mn_{1.64}In_{0.52}$. *Journal of Physics: Condensed Matter*, 23(45):456004, 2011.

[68] P J Brown, A P Gandy, K Ishida, R Kainuma, T Kanomata, K-U Neumann, K Oikawa, B Ouladdiaf, and K R A Ziebeck. The magnetic and structural properties of the magnetic shape memory compound $Ni_2Mn_{1.44}Sn_{0.56}$. *Journal of Physics: Condensed Matter*, 18(7):2249, 2006.

[69] J. Soltys. X-ray diffraction research of the order-disorder transitions in the ternary heusler alloys B_2MnAl (B = Cu, Ni, Co, Pd, Pt). *Physica Status Solidi (a)*, 66(2):485–491, 1981.

[70] R Kainuma, M Ise, K Ishikawa, I Ohnuma, and K Ishida. Phase equilibria and stability of the B2 phase in the Ni–Mn–Al and Co–Mn–Al systems. *Journal of Alloys and Compounds*, 269(1–2):173 – 180, 1998.

[71] R.W. Overholser, Manfred Wuttig, and D.A. Neumann. Chemical ordering in Ni-Mn-Ga heusler alloys. *Scripta Materialia*, 40(10):1095 – 1102, 1999.

[72] T. Miyamoto, W. Ito, R.Y. Umetsu, R. Kainuma, T. Kanomata, and K. Ishida. Phase stability and magnetic properties of $Ni_{50}Mn_{50-x}In_x$ Heusler-type alloys. *Scripta Materialia*, 62(3):151 – 154, 2010.

[73] K. Otsuka, T. Ohba, M. Tokonami, and C.M. Wayman. New description of long period stacking order structures of martensites in β-phase alloys. *Scripta Metallurgica et Materialia*, 29(10):1359 – 1364, 1993.

[74] S. Kaufmann, U. K. Rößler, O. Heczko, M. Wuttig, J. Buschbeck, L. Schultz, and S. Fähler. Adaptive modulations of martensites. *Phys. Rev. Lett.*, 104:145702, Apr 2010.

[75] J.S. Kasper and J.S. Kouvel. The antiferromagnetic structure of NiMn. *Journal of Physics and Chemistry of Solids*, 11(3–4):231 – 238, 1959.

[76] K R A Ziebeck and P J Webster. Helical magnetic order in Ni_2MnAl. *Journal of Physics F: Metal Physics*, 5(9):1756, 1975.

[77] B.D. Shanina, A.A. Konchits, S.P. Kolesnik, V.G. Gavriljuk, I.N. Glavatskij, N.I. Glavatska, O. Söderberg, V.K. Lindroos, and J. Foct. Ferromagnetic resonance in non-stoichiometric $Ni_{1-x-y}Mn_xGa_y$. *Journal of Magnetism and Magnetic Materials*, 237(3):309 – 326, 2001.

[78] Aksoy S, Posth O, Acet M, Meckenstock R, Lindner J, Farle M, and Wassermann E F. Ferromagnetic resonance in Ni-Mn based ferromagnetic heusler alloys. *Journal of Physics: Conference Series*, 200(9):092001, 2010.

[79] V Buchelnikov, V Sokolovskiy, S Taskaev, V Khovaylo, and P Entel. Monte carlo study of magnetocaloric properties of Ni-Mn-Ga Heusler alloys. *Journal of Physics: Conference Series*, 200(3):032008, 2010.

[80] V. D. Buchelnikov, P. Entel, S. V. Taskaev, V. V. Sokolovskiy, A. Hucht, M. Ogura, H. Akai, M. E. Gruner, and S. K. Nayak. Monte carlo study of the influence of antiferromagnetic exchange interactions on the phase transitions of ferromagnetic Ni-Mn-x alloys $(x = \mathrm{In}, \mathrm{Sn}, \mathrm{Sb})$. *Phys. Rev. B*, 78:184427, Nov 2008.

[81] V. V. Khovailo, K. Oikawa, T. Abe, and T. Takagi. Entropy change at the martensitic transformation in ferromagnetic shape memory alloys ni2+xmn1-xga. *Journal of Applied Physics*, 93(10):8483–8485, 2003.

[82] V. V. Khovailo, V. Novosad, T. Takagi, D. A. Filippov, R. Z. Levitin, and A. N. Vasil'ev. Magnetic properties and magnetostructural phase transitions in $\mathrm{Ni}_{2+x}\mathrm{Mn}_{1-x}\mathrm{Ga}$ shape memory alloys. *Phys. Rev. B*, 70:174413, Nov 2004.

[83] K. Oikawa, T. Ota, T. Ohmori, Y. Tanaka, H. Morito, A. Fujita, R. Kainuma, K. Fukamichi, and K. Ishida. Magnetic and martensitic phase transitions in ferromagnetic Ni–Ga–Fe shape memory alloys. *Applied Physics Letters*, 81(27):5201–5203, 2002.

[84] FullProf Suite, comprehensive set of crystallographic tools for Rietveld, profile matching & integrated intensity refinement of x-ray and/or neutron data. http://www.ill.eu/sites/fullprof.

[85] L.H. Schwartz and J.B. Cohen. *Diffraction from materials*. Materials science and technology. Academic Press, 1977.

[86] High-resolution two-axis diffractometer D2B. http://www.ill.eu/instruments-support/instruments-groups/instruments/d2b/description/instrument-layout/.

[87] Diffuse scattering neutron time of flight spectrometer DNS. http://www.frm2.tum.de/en/science/spectrometry/dns/index.html.

[88] R. M. Moon, T. Riste, and W. C. Koehler. Polarization analysis of thermal-neutron scattering. *Phys. Rev.*, 181:920, May 1969.

[89] O. Schärpf, T. Chattopadhyay, H. W. Weber, O. B. Hyun, and D. K. Finnemore. Polarized neutron experiments on $REBa_2Cu_3O_7\text{-}\delta$ with polarization and time of flight energy analysis. *physica status solidi (b)*, 175(1):175–196, 1993.

[90] P.J. Brown, H. Capellmann, J. Déportes, D. Givord, and K.R.A. Ziebeck. Ferromagnetic correlations in both the α and γ-phases of paramagnetic iron. *Journal of Magnetism and Magnetic Materials*, 30(3):335 – 339, 1983.

[91] K.R.A. Ziebeck, J.G. Boom, P.J. Brown, H. Capellmann, and J.A.C. Bland. Observation of spatial magnetic correlations in the paramagnetic phase of chromium using polarised neutrons and polarisation analysis. *Zeitschrift für Physik B Condensed Matter*, 48:233–239, 1982.

[92] Masayuki Shiga, Hiroyuki Nakamura, Masakazu Nishi, and Kazuhisa Kakurai. Polarized neutron scattering study of β-Mn and β-$\mathrm{Mn}_{0.9}\mathrm{Al}_{0.1}$. *Journal of the Physical Society of Japan*, 63(5):1656–1660, 1994.

[93] V.K. Arkad'yev. Ferromagnetic properties of metals as function of wavelength. *Journal of Russian physical and chemical society*, 45:103, 1913.

[94] V.K. Arkad'yev. Electromagnetic field theory in ferromagnetic metal. *Journal of Russian physical and chemical society*, 45:312, 1913.

[95] J. H. E. Griffiths. Anomalous high-frequency resistance of ferromagnetic metals. *Nature*, 158:670, 11 1946.

[96] E. K. Zavoiskii. Magnetic spin resonance in ferromagnets on centimeter waves. *Journal of Experimental and Theoretical Physics*, 17:883, 1947.

[97] Aleksandr V Kessenikh. Magnetic resonance: discovery, investigations, and applications. *Physics-Uspekhi*, 52(7):695, 2009.

[98] G. G. Scott. Review of gyromagnetic ratio experiments. *Rev. Mod. Phys.*, 34:102–109, Jan 1962.

[99] Charles Kittel. On the gyromagnetic ratio and spectroscopic splitting factor of ferromagnetic substances. *Phys. Rev.*, 76:743–748, Sep 1949.

[100] J Pelzl, R Meckenstock, D Spoddig, F Schreiber, J Pflaum, and Z Frait. Spin–orbit-coupling effects on g-value and damping factor of the ferromagnetic resonance in Co and Fe films. *Journal of Physics: Condensed Matter*, 15(5):S451, 2003.

[101] S. P. Heims and E. T. Jaynes. Theory of gyromagnetic effects and some related magnetic phenomena. *Rev. Mod. Phys.*, 34:143–165, Apr 1962.

[102] S.V. Vonsovskii. *Magnetism*. Number v.1 in Magnetism. J. Wiley, 1974.

[103] Jian Liu, Nils Scheerbaum, Sandra Weiß, and Oliver Gutfleisch. Ni–Mn–In–Co single-crystalline particles for magnetic shape memory composites. *Applied Physics Letters*, 95(15):152503, 2009.

8 Acknowledgments

First I would like to thank all, who helped, assisted me during my scientific studies, and all the people, who helped and supported me during the "darker" days. Without their compassion and understanding, this work would have never been done.

First of all, I would like to express my gratitude to Prof. Dr. M. Farle for giving me the opportunity to work in his group, develop my scientific qualities and many more.

I would like to thank Prof. i. R. Dr. M. Acet, *hocam*, for supervision and support, teaching and helping, compassion and understanding, providing ideas and topics for the research, making the PhD research truly interesting and challenging.

I would like to acknowledge Dr. S. Aksoy for the introduction to the *"workflow"*, showing me around the labs in the very beginning of my work.

I would like to express my deepest gratitude to Dr. A. Elsukova for the midnight scientific discussions, fruitful co-working and her endless support, sincere friendship and understanding.

I would like to thank:

Dr. S. Ener for the help with DSC measurements, crash-in course in RSA and FullProf, and good times in Münich;

Dr. R. Meckenstock and Dipl. Phys. C. Schöppner for the introduction to FMR and beneficial discussions of the FMR measurements afterwards;

M. Sc. Y. Aleksandrov for assisting me with SEM and EDX as well for teaching me Turkish and sharing a beer;

Prof. Dr. L. Mañosa, Prof. Dr. A. Planes, and Dr. T. Krenke for discussions of the MCE experiments and giving useful hints on them;

Dr. Y. Su at the Forschungsreaktor München II for his help in temperature dependent polarized neutron scattering measurements on DNS instrument;

Dr. E. Suard at the Institute Lauve-Langevine in France for her help in temperature dependent neutron diffraction measurements on D2B instrument;

M. Sc. F. Scheibel for helping in "Übersetzung von Kurzzusammenfassung";

Dipl. Ing. H. Zähres and D. Schädel for the *"applied technical magic"*, making small and large things work, helping out with suggestions and ideas about technical problems;

Team assistance S. Grubba and H. Mundt for their friendly help in various issues with papers, arrangements, etc...

Prof. Dr. V.N. Prudnikov and Prof. Dr. A.B. Granovskii from Lomonosov Moscow State University for the detailed criticism and discussion of the scientific methods and experimental approach;

The whole working group of Prof. Dr. M. Farle (students, postdocs, co-workers) for the very scientific and friendly atmosphere, discussions on science and life;

The members of *"the Turkish village"* lab for the days and nights spent on ΔT setup, while doing the measurements and exchanging Turkish and Russian cultures.

Financial support from the Deutsche Forschungsgemeinschaft through the Priority Programme SPP1239 is gratefully acknowledged.

I would like to express my gratitude to my family: my wife, parents and grandparents, their support and love leads me through my life and research.

9 List of Publications

1. **I. Titov**, M. Acet, M. Farle, D. González-Alonso, L. Mañosa, A. Planes, and T. Krenke, *Hysteresis effects in the inverse magnetocaloric effect in martensitic Ni-Mn-In and Ni-Mn-Sn*, Journal of Applied Physics, **112** (2012) 073914

List of publications not included in this thesis:

1. S. Ener, J. Neuhaus, W. Petry, R. Mole, K. Hradil, M. Siewert, M. Gruner, Markus, P. Entel, **I. Titov**, and M. Acet, *Effect of temperature and compositional changes on the phonon properties of Ni-Mn-Ga shape memory alloys*, Physical Review B, **86** (2012), 144305
2. V.N. Prudnikov, A.B. Granovskii, A.P. Kazakov, M.V. Prudnikova, D.E. Mettus, **I.S. Titov**, *Galvanomagnetic phenomena in ferromagnetic metals and alloys. Advanced lab course*, Typography of the Moscow State University, 2012, ISBN 976-5-8279-0111-2
3. L. Mañosa, D. González-Alonso, A. Planes, M. Barrio, J.L. Tamarit, **I.S. Titov**, M. Acet, A. Bhattacharyya, and S. Majumdar, *Inverse barocaloric effect in the giant magnetocaloric La-Fe-Si-Co compound*, Nature communications, **2** (2011), 595
4. V.N. Prudnikov, A.P. Kazakov, **I.S. Titov**, Ya. N. Kovarskii, N.S. Perov, A.B. Granovsky, I. Dubenko, A.K. Pathak, N. Ali, and J. Gonzalez, *Quasi-diamagnetism and exchange anisotropy in Ni-Mn-In-Co Heusler alloys*, Physics of the Solid State, **53** (2011), 490
5. V.N. Prudnikov, A.P. Kazakov, **I.S. Titov**, N.S. Perov, A.B. Granovskii, I.S. Dubenko, A.K. Pathak, N. Ali, A.P. Zhukov, and J. Gonzalez, *Hall effect in a martensitic transformation in Ni-Co-Mn-In Heusler alloys*, JETP Letters, **92** (2010), 666

Curriculum vitae

Name : Ivan S. Titov
Date/Place of Birth : 10.11.1987 in Moscow
Nationality : Russian
Marital Status : married

Education :

10.2013 — …	PhD student, Faculty of Physics, Lomonosov Moscow State University, Moscow, Russia
05.2010 — 12.2012	research assistant, Faculty of Physics, University of Duisburg-Essen, Duisburg, Germany
01.2010	Master's degree in physics, thesis title: *"Study of the transport properties of the single nanoparticles and nanoparticle ensembles."*
09.2004 — 01.2010	student, Faculty of Physics, Lomonosov Moscow State University, Moscow, Russia
09.1994 — 06.2004	School №843, Moscow